DOCTORAL SCHOOL
UNIVERSITA' *MEDITERRANEA* DI REGGIO CALABRIA

DIPARTIMENTO DI INGEGNERIA DELL'INFORMAZIONE, DELLE INFRASTRUTTURE E
DELL'ENERGIA SOSTENIBILE (DIIES)

Ph.D IN
INFORMATION ENGINEERING

S.S.D. ING-IND/22
S.S.D. ING-INF/01
XXXV CICLO

DESIGN AND DEVELOPMENT OF A SENSING DEVICE FOR ENVIRONMENT MONITORING

CANDIDATE
Antonio FOTIA

ADVISOR
Prof.ssa Patrizia FRONTERA

Prof. Francesco DELLA CORTE

CO-ADVISOR
Ing. Angela MALARA

Ing. Massimo MERENDA

COORDINATOR
Prof. Antonio IERA

ANTONIO FOTIA

DESIGN AND DEVELOPMENT OF A SENSING DEVICE FOR ENVIRONMENT MONITORING

The Teaching Staff of the PhD course in
INFORMATION ENGINEERING
consists of:

Antonio IERA (coordinator)
Pier Luigi ANTONUCCI
Giuseppe ARANITI
Francesco BUCCAFURRI
Claudia CAMPOLO
Giuseppe COPPOLA
Mariantonia COTRONEI
Lorenzo CROCCO
Dominique DALLET
Claudio DE CAPUA
Francesco DELLA CORTE
Giuliana FAGGIO
Gioia FAILLA
Fabio FILIANOTI
Patrizia FRONTERA
Sofia GIUFFRÈ
Giorgio GRADITI
Voicu GROZA
Tommaso ISERNIA
Gianluca LAX
Aime Lay EKUAKILLE
Gaetano LICITRA
Antonella MOLINARO
Andrea MORABITO
Carlo Francesco MORABITO
Giacomo MORABITO
Rosario MORELLO
Fortunato PEZZIMENTI
Filippo PRATICÒ
Domenico ROSACI
Giuseppe RUGGERI
Mariateresa RUSSO
Antonino VITETTA

Nulla si ottiene senza sacrificio e senza coraggio. Se si fa una cosa apertamente, si può anche soffrire di più, ma alla fine l'azione sarà più efficace. Chi ha ragione ed è capace di soffrire alla fine vince.

(Mahatma Gandhi)

Il senso del sacrificio è l'assoluta umiltà necessaria per agire pur sapendo che non vedremo i risultati.

(Alejandro Jodorowsky)

Abstract

Analyses of the presence of heavy metals are particularly important in assessing water quality. The detection of heavy metal ions (HMI) in water is commonly performed using a variety of traditional methods. The monitoring of environmental parameters leads to the collection and analysis of a large set of data that may be used to reduce polluting actions, suggesting that IoT technology may provide an efficient contribution to the mitigation of environmental issues. Under this context, this thesis, which has a multidisciplinary approach and a "cradle to gate" research perspective, culminates in the creation of sensing devices for environmental monitoring. This thesis presents a novel active layer for the detection of heavy metals in aqueous solutions. The electrospinning method was utilized to produce the polymeric microfibers that constitute the active layer, and different investigation techniques were employed for its characterization. Electrochemical impedance spectroscopy (EIS) was used to perform the sensing tests with lead and thallium as pollutants. Indeed, both metals, that can be found in industrial wastewater, are known to be harmful to the environment and human health, even at low concentrations. This work also aims at training a machine learning model that can be implemented on a portable device using a low-power microcontroller.

II

Contents

VI

List of Figures

X

X

List of Tables

Introduction

With the increase in urbanization, environmental issues are important concerns that research must address. Air quality and water pollution are major factors that pose genuine challenges for the environment. Indeed, a suitable monitoring is necessary so that the world can achieve sustainable growth, maintaining at the same time a healthy society. Potentially, the IoT technology can give an efficient contribution to mitigate environment-related problems, since the monitoring of environmental parameters lead to the collection and analysis of a whole set of data that can be used to mitigate/reduce actions of polluting.

Under this scenario, this thesis, characterized by a multidisciplinary approach and with a perspective "cradle to gate" developed research, is finalized to the development of sensing devices for the environmental monitoring.

The thesis introduces an innovative active layer for the detection of heavy metals in aqueous solutions. The active layer, made up of polymeric microfibers, was produced using the electrospinning technique, a very simple, inexpensive, and scalable technique, and was directly collected on interdigitated electrodes. Different types of microfibers were produced and characterized using complementary characterization techniques.

The sensing tests were performed using the electrochemical impedance spectroscopy (EIS) technique with lead and thallium as contaminants, both known to cause risks to the ecosystem and human health even at low concentrations, being present in industrial wastewater.

In addition, using the obtained sensing data, this work also aimed at training a machine learning model, that can be implemented on a portable device using a low-power microcontroller. The approach adopted for the machine learning is divided into two parts: i) training and selection of the best-performing model

to be carried out on a desktop using the dataset obtained by sensing tests; ii) performing runtime inference on a dedicated board. The focus is centred on the training of different types of algorithms, both qualitatively (classification) and quantitatively (regression), with the prospect to realize in the future a low-power device capable of performing the measurement and predicting the response.

The thesis is organized in six chapters. The first two are related to the analysis of the state of art dealing with sensors for environmental monitoring, particularly focused on the detection of heavy metals in water (*Chapter 1*) and about the electrical impedance spectroscopy (EIS), a digital analysis method of measurement that could be integrated with IoT technologies (*Chapter 2*).

The experimental part is divided into four chapters. The activities related to the design and the characterization of performant active layers of sensing devices are described in the *Chapter 3* and *Chapter 4*. Following, the sensing performance of prototype-devices have been measured and the results are reported in the *Chapter 5* and finally the training of classification and regression models with the experimental data have been proposed in the *Chapter 6*.

The experimental activity here presented was carried out in the laboratory of *Materials for Environmental and Energy Sustainability* and the laboratory of *Electronics and Microelectronics* of the University Mediterranea of Reggio Calabria. The study, design, construction and characterization of single fiber sensors were carried out at the Department of Nanomaterials of the Interdisciplinary Centre of Nanoscience of Marseille (CINaM), in collaboration with Dr. Beniamino Sciacca.

1

Sensors for environmental monitoring

Analyses of the presence of heavy metals are of particular importance for the evaluation of water quality. Nowadays, there are several conventional techniques that are generally used to evaluate the presence of heavy metals ions (HMI) in water. The aim of this chapter is to introduce the problems related to the presence of HMI in the environment, and to discuss about the activity of metal chelating agents. Furthermore, the main electrochemical techniques for the detection of heavy metals and the state of the art of electrochemical sensors and materials used for the electrode are described.

1.1 Heavy metals ions (HMI) in the environment

The word "heavy metals" indicates any metallic element that has a relatively high density and is toxic or poisonous even at low concentration. This term is applied to the group of metals and metalloid with atomic density at least 5 times greater than that of water. Heavy metals include copper (Cu), zinc (Zn), lead (Pb), mercury (Hg), silver (Ag), cadmium (Cd), chromium (Cr), iron (Fe), arsenic (As), and the elements of the platinum group [1]. Human exposure to heavy metals pollution can occur through different pathways: food, air, soil and water. The latter is one of the main vectors of these ions, because it can reach humans directly (ingestion or dermal adsorption), and indirectly through food (animals, fishes and plants).

When heavy metals are introduced into our bodies through ingestion or inhalation, they are not metabolized by the body, but they tend to bioaccumulate. Bioaccumulation has biological and physiological consequences in the human body since causes serious damage to the respiratory and reproductive systems, as well as the digestive tract and neurodegenerative disorders and diseases, such as Alzheimer and Parkinson diseases [2].

Heavy metals have been classified into two categories based on their toxicity: essential and non-essential. Essential heavy metals are necessary for life and, at low concentrations, they are nontoxic, instead, non-essential heavy metals have no known biological role in living organisms and, even at low concentrations, are very hazardous. Essential heavy metals play important physiological and biochemical roles in biological systems. Since they may be components of biomolecules, they are required for the proper function of various enzymes and proteins and either their deficiency or excess can have an impact on the human body. Mn, Fe, Cu, and Zn are examples of necessary heavy metals. For example, zinc is a constituent for many enzymes, iron is important for haemoglobin, selenium is essential for the glutathione peroxidase enzyme; cobalt is essential for the synthesis of vitamin B_{12} [2]. Cd, Pb, and Hg, whereas are toxic and considered physiologically nonessential. Ni, Cr, and Cd are recognised for the carcinogenic properties.

Heavy metals and metalloid poisoning have a negative impact on an organism's reproductive system. Nickel interferes with protamine causing the histone to be replaced in spermiogenesis. Cadmium causes erectile dysfunction in adult males, interferes with fertilization, and harms developing fetuses and neonates. Lead can alter sex hormones and destabilize chromatin, resulting in congenital disabilities. It also causes seminiferous tubule atrophy and miscarriage or low birth weight [3].

Specifically, heavy metals induce oxidative stress by generating, directly, free radicals, such as the reactive oxygen and nitrogen species (RNS; ROS) which damages DNA, alters sulfhydryl homeostasis, and promotes the peroxidation of lipids in the plasma membrane [2], or indirectly through the depletion of cellular antioxidants. For example, arsenic has been shown to produce superoxide ($O_2^{\cdot-}$), oxygen ($O_2^{\cdot}$), nitric oxide ($NO^{\cdot}$), hydrogen peroxide (H_2O_2), and peroxyl ($ROO^{\cdot}$) radicals. Pb exposure significantly reduces antioxidant parameters, such as GPx, CAT, SOD, GST, and GSH while it increases oxidative parameters MDA and H_2O_2 [4]. Because of their highly soluble, stable, non-biodegradable nature and ability to migrate throughout aqueous medium, heavy metals have a negative impact on human health and also on

plants, causing photosynthesis inhibition, reduced seed germination, decreased enzyme activity, and chlorophyll synthesis [5]. For this reason, HMI have been included as significant elements to be monitored, especially in water, by several international organization like the World Health Organization (WHO), European Union (EU), Centre for Disease Control (CDC) and the US Environmental Protection Agency (EPA) [6]–[8]. The primary sources and related permissible limits are reported in **Table 1**.

Table 1 - Source of heavy metals and related toxicity of human health.

Heavy Metals	Sources	Toxic Impact on Human Health	Permissible Limits [6], [8]
Arsenic (As)	drinking-water and food; industrial processes; tobacco	pigmentation changes, skin lesions, hyperkeratosis	10 μg/L
Cadmium (Cd)	corrosion of galvanized pipes, erosion of natural deposits, discharge from metal refineries, runoff from waste batteries and paints	renal tubular dysfunction, osteoporosis, acute pneumonitis, cancer	3 μg/L
Chromium (Cr)	coal and oil combustion; electroplating; leather tanning; industrial processes, tobacco	contact dermatitis, hemolysis, renal diseases, allergic reaction, cancer	50 μg/L
Lead (Pb)	drinking-water and food; lead-containing pipes; children's toys; cosmetics	microcytic anemia; nephropathy; immune system diseases; reproductive system diseases; developmental system disease	10 μg/L
Mercury (Hg)	accidents, environmental pollution, dental care,	calcium homeostasis; neurological diseases, corrosive to skin,	6 μg/L

	preventive medical practices, industrial and agricultural operations, fish consumption	corrosive to eyes, cancer, corrosive to the gastrointestinal tract	
Thallium (Tl)	drinking-water and food; air-borne contamination (fly ash)	gaseous emission of cement factories, coal-burning power plants, metal sewers	0.5 μg/L
Selenium (Se)	natural deposits releases from copper smelting	endocrine function, hepatotoxicity, and gastrointestinal disturbances	40 μg/L
Copper (Cu)	industrial discharges, copper salts, plumbing material	brain and kidney damage, chronic anemia, stomach and intestine irritation	2 mg/L
Zinc (Zn)	discharges of smelter slags and wastes, mine tailings, coal and bottom fly ash, fertilizers	dizziness, fatigue	5 mg/L

Heavy metals have contaminated around 40% of the world's lakes and rivers. High quantities of Cd^{2+}, Cu^{2+}, and Zn^{2+} ions have been found in 9 coastal rivers in the Laizhou Bay basin in China. Significant mercury pollution has been found in Venezuela's Coyuni river basin, which has been linked to amalgam methods used in grassroots gold mining. Several heavy metals were also discovered in two major rivers in Antalya, Turkey[9].

The pollution of heavy metals in the atmosphere, soils and waters is mainly due to and anthropogenic activities like mining, several industries that are metal-based, fossil fuel combustion and the use of pesticide and fertilisers in the agricultural field. Additionally, natural factors including volcanic activity, metal corrosion, metal evaporation from soil and water and sediment re-

suspension, soil erosion, and geological weathering can contribute to the accumulation of HMs [10]. For example, lead is a heavy metal that is widely produced by the mining, electroplating, and battery manufacturing industries; the US Environmental Protection Agency lists it as a priority pollutant due to its biological toxicity and non-degradability in the environment [11].

Metal toxicity can be either acute or chronic. The dose/quantity of a metal, its nature, its biological function, the exposed organism, and the time during which the organism is exposed are only a few of the many variables that affect how toxic a metal is. Numerous approaches have been employed for the detection of heavy metal ions, which may be categorized into three major groups: spectroscopic detection techniques, electrochemical detection techniques, and optical detection techniques [12]. The most widely used techniques for removing metals from wastewater include those based on precipitating metal hydroxides or sulphides, ion exchange on chelating ion exchangers, evaporation in vacuum evaporators, reverse osmosis, membrane filtration, electrochemical processing techniques, adsorption on various materials, co-precipitation with ferrite, or the use of starch or borohydride xanthates to convert metal ions [13]. It is possible for heavy metals to be present in either their gaseous or particulate forms; this is determined by the manner in which they are transported from one location to another, which can include wind, catchment areas, drainage water, and improper dumping of untreated water into other water bodies [14].

1.2 Activity of metal chelating agents

The detection of heavy metals as well as their removal from pollutant sites is very important. Many different methods have been explored in literature and the use of chelating agents has been extensively treated [15].

Chelating agents, because of their ability to complex metals, are widely used in a variety of industrial, domestic, and agricultural fields. They have been used in several applications over the last few decades, including scale and corrosion inhibitors, pulp, paper, and textile production, cleaning and laundry operations,

microorganism prevention/inhibition, soil remediation, waste and effluent treatment, agriculture, metal electroplating and other surface treatments, tanning processes, cement admixtures, photography, food products, pharmaceuticals, and cosmetics [16].

Sir Gilbert T. Morgan and H. D. K. Drew coined the term chelate in 1920. Chelation derives from the Greek word *chele*, which means lobster claw, and thus represents the concept of clinging or holding with a firm grip [17]. It is the process by which ions/molecules of a ligand form a coordination bond with the central metal atom/ions leading to a cyclic or ring like structure called 'chelate' [2]. A ligand is an ion or molecule having two or more atoms capable of contributing two electrons in order to create a covalent connection with a metal atom/ion. Generally, atoms such as S, N, and O act as ligand atoms in the form of chemical groups such as -SH, -S-S, -NH₂, =NH, -OH, -OPO₃H, or >C=O [17]. Ligands are categorized into three categories based on the number of donor atoms: unidentate (one donor atom), bidentate (two donor atoms), and polydentate (more than two donor atoms). Chelate complexes are more stable than the analogous complexes with monodentate ligands. The stability of these complexes varies depending on the interactions between the ligand and the metal ion.

Good chelating agents have high solubility in water, a higher affinity for harmful metals and produce chemically inert and non-toxic complexes. The stability constants K_s of the chelant-metal complexes is commonly used to assess a chelant's efficiency in metal extraction. The order of magnitude of the K_s can be used to rank different chelants based on their overall efficacy, but not to rank the efficacy of a specific chelant toward different metals, because the latter is also dependent by metal speciation in a given matrix [18]. Additionally, pH has a significant impact on the stability and development of complexes. At low pH, the majority of chelating agents are unstable, but at high pH, metals frequently form insoluble hydroxides that are less receptive to chelating agents.

The most commonly used chelating agent is based on ethylenediaminetetraacetic acid (EDTA), a synthetic polyamino-polycarboxylic

acid that has been used to treat childhood lead poisoning since the 1950s [17], and its salts, such as ethylenediaminetetraacetic acid disodium salt Na$_2$-EDTA. It does not react directly with lead metal but reacts with lead ions by coordinating two molecules around the ion through the electron pairs associated to the nitrogen atoms on the molecule. The result is called an organometallic complex, Pb-EDTA, characterized by a high stability constant [19]. Different hypotheses have been made on the reaction mechanism and, due to the complexities between the modified adsorbents and metals, both the chelation and ion-exchange for EDTA modified adsorbents have been reported in the literature. Indeed, in the latter case, when ion-exchange model is considered, EDTA can take up (or absorb) positively or negatively charged ions from aqueous electrolyte solutions and at the same time release other ions of equivalent amount into the aqueous solution.

Less expensive than other chelators, EDTA is a mass-produced metal sequestrant and applied in many industrial processes because of its excellent chelating ability with heavy metal ions, such as in industrial detergents and fertilizers [20]. It is also frequently used as a soil washing eluent for the remediation of Pb(II) and Cd(II)-contaminated soil [11]. In a large number of cases, EDTA has been used in processes which are solely targeted at the removal of heavy metals from different industrial effluents. Cadmium, lead, copper, and manganese have been extracted from industrial solid wastes using EDTA aqueous extraction solutions [21]. Indeed, EDTA shows a high selectivity to numerous heavy metal ions since it is possible to control interference quite well by regulating the pH of the solution [22].

Therefore, since EDTA has favourable chelating and ion-exchange properties for many different metal ions, its immobilization on the different supporting materials for the metal adsorption purposes has received wide attention. Many examples of the use of EDTA to modify supports have been reported in the literature and in all these cases, EDTA was observed to form stable chelates with metals, suppressing their activities [23].

Due to the interesting chelating properties, an upgraded use of EDTA was focused on the development of electrochemical sensor, able to exploit the

formation of metal-complexes for the detection and quantification of heavy metals in aqueous solutions. Even in those cases, the dispersion of EDTA over a suitable support was considered of pivotal importance. For example, Dong et al. developed an ultra-sensitive electrochemical sensor able to detect lead, based on an EDTA intercalated layered double hydroxides modified carbon paste electrode [24]. A low-cost, rapid and sensitive electrochemical sensor based on an organic layer of EDTA-NQS (1,2-napthaquinone-4 sulphonic acid sodium salt) formed on the surface of a glassy carbon electrode was developed by Toghan et al., confirming the complexation of EDTA-NQS electrode surface with HMIs and showing a good activity, sensitivity, selectivity, stability, and reproducibility, with a very low detection limit for the simultaneous detection of different heavy metal ions, such as Cu^{2+}, Cd^{2+}, Hg^{2+}, Pb^{2+} and Fe^{3+}. Other authors investigated the electrochemical recognition of Hg(II) ions utilizing EDTA modified polyaniline (PANI)/Graphene Oxide (GO) composite material. The activity of the sensor toward Hg(II) ions was tested by differential pulse stripping voltammetry (DPSV) from 30 to 1 ppb. The modification by the EDTA chelating ligand showed a successful increase of the affinity of PANI/GO composite toward Hg(II) ions [25]. In the study of Chen et al., EDTA was intercalated into layered double hydroxides (LDH) by the coprecipitation method, and then encapsulated in a polymeric matrix of polyacrylonitrile (PAN) using the electrospinning technique. The performance of MgAl-EDTA-LDH@PAN electrospun nanofiber membrane was finally evaluated and proved for copper removal [26]. Deshmukh et al. proposed instead a nanocomposite material made by polypyrrole (Ppy) and single walled carbon nanotubes (SWNTs), that was successfully synthesized by an electrochemical method on a stainless-steel electrode (SSE). The functionalization with EDTA was performed using the dip coating technique at room temperature. The EDTA-Ppy/SWNTs modified stainless steel electrode exhibited good sensitivity and selectivity toward the detection of Pb(II) ions in aqueous media, showing a detection limit of 0.07μM [27].

In this study, the evaluation of the dispersion of the EDTA-based chelating agent over a suitable support has been considered and discussed. In particular,

on account of the featuring properties and characteristics of the chelating agent, the encapsulation in a polymeric matrix through the electrospinning technique was pursued as a good compromise between a rapid and low-cost method and the production of high-quality materials for the development of sensitive layers.

1.3 Electrochemical Techniques for the detection of heavy metals

There are various techniques used to determine the presence of heavy metals in solution, including atomic adsorption spectroscopy (AAS) [28], inductively coupled plasma optical emission spectrometry (ICP-OES) [29], flameless atomic absorption spectrophotometry (FAAS) [30], inductively coupled plasma mass spectrometry (ICP-MS) [31]. However, although they are very selective and sensitive techniques, they require very expensive devices, which can only be used by qualified personnel, given the complex operating procedures, and they also require quite long periods to carry out the measurements.

The electrochemical methods, unlike those previously mentioned, are affordable, user-friendly, involve simple procedures for the monitoring of contaminated samples and have a very short analytical time in comparison to other spectroscopic techniques [32]. Electrochemical techniques can be subdivided as shown in **Figure 1**. For static techniques, no net reaction occurs and the currents in the system are ideally zero. In the dynamic methods the system is dynamic in the sense that a net reaction proceeds and there are significant currents flows [33]. The latter can be classified in controlled current and controlled potential. Instruments called galvanostats are used in controlled current techniques to manage the current and measure the potential of the working electrode. Otherwise, when the potential is controlled, the devices, called potentiostats, are used, allowing to control the potential. The current is then evaluated as the answer of the electrochemical system to the induced potential.

Voltammetry is one of the few electrochemical methods that has a high sensitivity and gives the possibility to carry out heavy metal detection tests, directly in situ. The typical voltammetry techniques for heavy metals detection

are cyclic voltammetry (CV) [34], [35] , differential pulse voltammetry (DVP) [36], [37], square wave voltammetry (SWV) [38], [39] and stripping voltammetry (SV) [40], [41]. However, in recent years, many attempts have been made to use electrochemical impedance spectroscopy (EIS) [42], [43] in order to assess the presence of these pollutants.

The above-mentioned techniques will be described in detail in the following subparagraphs and schematically summarized in **Figure 2**.
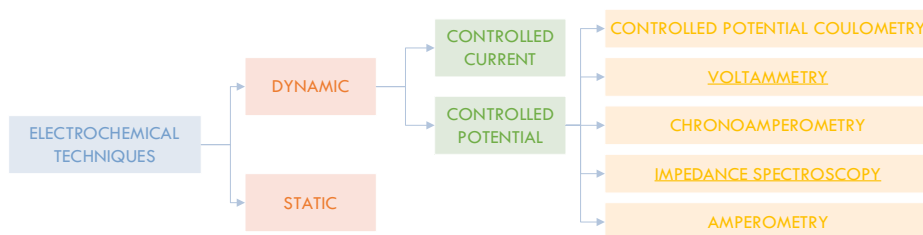
Figure 1- Electrochemical techniques.

1.3.1 Cyclic Voltammetry

Cyclic voltammetry consists in applying an increasing or decreasing potential, first in one direction and then in the reverse one, using the same scan rate. It is occasionally employed for the quantitative determination of the analytes, but it is commonly used to study redox reactions and to obtain information about the chemical reaction occurred. The current is recorded and plotted against the applied potential, in order to achieve cyclic voltammogram. From CV, some significant parameters, like anodic and cathodic peak potentials and corresponding currents, can be obtained.

1.3.2 Differential Pulse Voltammetry

Pulse voltammetry, a subtype of voltammetry, results from the use of pulses of voltage signals with varying shapes and amplitudes in voltammetric measurements. The subcategories of pulse voltammetry include normal pulse voltammetry, reverse pulse voltammetry, differential pulse voltammetry, etc. Due to its high sensitivity towards the detection of heavy metal ions, DVP is the most prevalent pulse voltammetric technique. Comparing normal pulse

voltammetry and differential pulse voltammetry reveals that the potential pulse, in DVP, is fixed and superimposed on a slowly varying base potential. Current is measured at two points: before the application of the pulse and at its conclusion. The difference between the first and the second current is plotted against the applied potential. The peak current produced is proportional to the concentration of the analyte.

1.3.3 Square Wave Voltammetry

Square wave voltammetry is among the most rapid and sensitive pulse voltammetry methods. In SWV, the form of the potential current curve is determined by the application of potentials of height (pulse amplitude) that fluctuate based on a potential step (in mV) and duration (τ). On the potential–time curve, the pulse width is represented by $t = \tau/2$, and the frequency of pulse application is represented by $f = 1/t$. The electric currents are measured at the end of the direct (I_1) and reverse (I_2) pulses, and the signal is acquired as the intensity of the resultant differential current (I). This method provides great sensitivity and strong capacitive current rejection. SWV's primary benefit is its speed. Compared with square wave and differential pulse voltammetry for reversible and irreversible situations, it was revealed that square-wave currents are 4 and 3.3 times greater, respectively, than the corresponding differential-pulse response.

1.3.4 Stripping Voltammetry

For the study of trace amounts of electroactive species in solution, stripping voltammetry is an extremely sensitive technique. There have been reports of detection limits for metal ions at sub-ppb quantities. Stripping voltammetry consists of two primary steps: electrodeposition, where an analyte solution is placed on the electrode from a well-stirred solution, and the voltammetric step, when the analyte is stripped off and may be analysed by any of the VM techniques. By using an anodic potential scan or a cathodic potential scan, the stripping voltammetry is further classified as anodic stripping voltammetry

(ASV) or cathodic stripping voltammetry (CSV), respectively. In addition to a very low detection limit, stripping voltammetry needs equipment that are easy to use, affordable, and highly suitable for downsizing.

Stripping methods can be combined with various pulse voltammetric techniques to create new detection techniques, such as linear sweep anodic stripping voltammetry, differential pulse anodic stripping voltammetry, square wave anodic stripping voltammetry, etc., which are quite effective for trace level detection of heavy metal ions with extremely low detection limits.
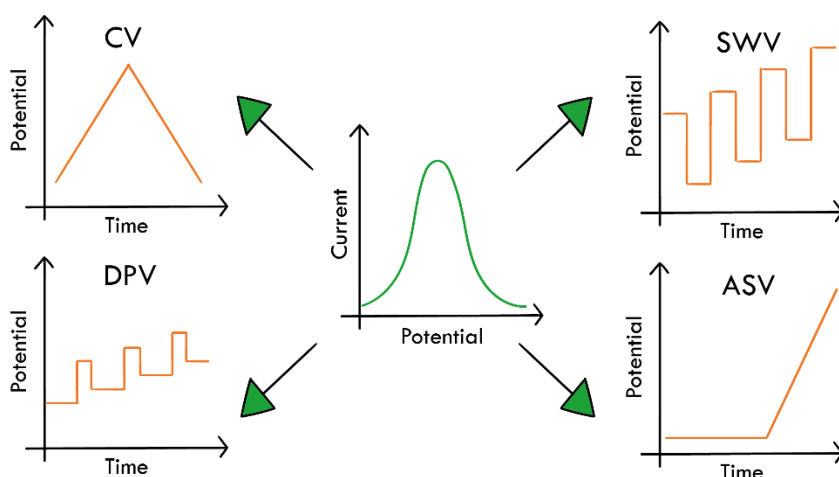
Figure 2 - Potential versus time graphs for some voltammetry techniques used to produce a signal. Adapted from [22].

1.3.5 Electrochemical Impedance Spectroscopy

Impedance spectroscopy is a highly sensitive electrochemical technique used to measure the impedance of a system in dependence of the AC potentials frequency. Using an electrode setup consisting of a working, reference, and counter electrodes a known voltage is passed from the working electrode through an electrolytic solution and into the counter electrode. Quantitative measurements can be performed by the EIS, determining a wide range of dielectric and electrical properties in research fields studying batteries, corrosion, coatings, biomedical devices, semiconductors, solid-state devices, as well as sensors. This technique will be described in more detail in *Chapter 2*.

1.4 Electrochemical sensors

1.4.1 Electrochemical cell and configurations

An electrochemical cell is required to investigate the electrochemical process. A potentiostat/galvanostat is the necessary electrical hardware for controlling the electrochemical cell and performing electrochemical measurements. Currently, two different kinds of electrochemical cells are used to detect HMI in water solutions. **Figure 3** depicts either a three-electrode or two-electrode configurations.
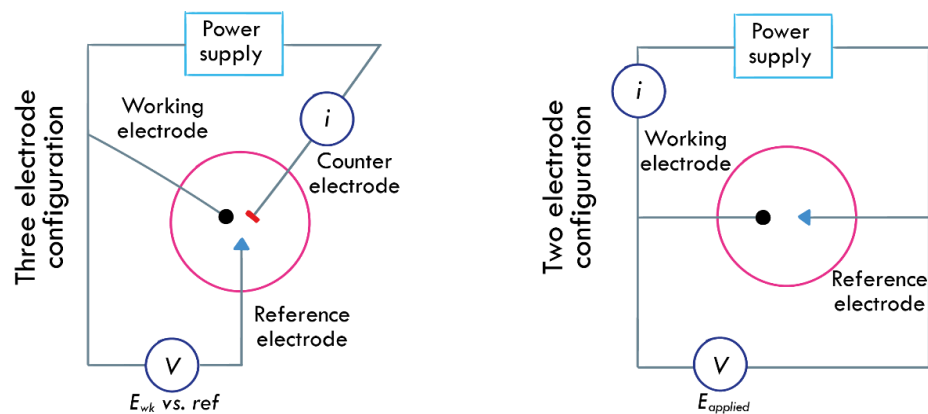
Figure 3 - Different configurations of electrochemical cell. Adapted from [44].

Usually, the electrode under investigation is called the working electrode (WE), and the electrode necessary to close the electrical circuit is called the counter electrode (CE). A two-electrode configuration is used to investigate electrolyte proprieties. A three-electrode configuration is most common for classic electrochemical applications. A reference electrode (REF) is a third electrode, and it is used to determine, with high precision, the potential across the electrochemical interface.

The current is measured after applying a voltage to the working electrode. This is coupled with a reference electrode whose known fixed voltage is as near as feasible to a non-polarized voltage. As the following equation [44] shows, the voltage that is applied is not always the same as the voltage that is measured in the electrochemical cell.

$$E_{applied} = E_{cell} - iR_s \ (1)$$

Where $E_{applied}$ represents the applied voltage to the potentiostat, which is divided into two fractions. E_{cell} is the voltage given to the working electrode to drive the redox reaction, while the remainder of the voltage represents the ohmic drop (iR_s) induced by the current passing through a resistive solution. This ohmic drop is typical of the bulk solution, so it will change with the concentration of the electrolyte. In analyses where extremely small electrodes (nano or microelectrodes) are employed, the current is frequently on the order of nanoamperes, and the electrolyte concentration is high, the contribution of the ohmic drop is minimal, and thus a cell can be used for a two-electrode configuration. However, when the electrolyte concentration in the solution being measured is low and a big electrode (more than a hundred microns in diameter) is used, the ohmic drop will be significant, and a three-electrode system is therefore chosen. The third electrode is a counter electrode (or auxiliary electrode). Its main function is to stop the current from flowing between the working electrode and the reference electrode, and to allow instead the current flow between the counter electrode and the working electrode.

For most electrochemical measurements, one of the electrodes in an electrochemical cell must be maintained at a constant potential. This so-called reference electrode permits the control of a working electrode's potential. In electrochemical devices, the standard hydrogen electrode (SHE) serves as a reference element. However, it is hard to handle. In most experiments, secondary reference electrodes are therefore preferred. A secondary reference electrode must satisfy the following criteria:

- The thermal coefficient of potential must be small;
- It must be chemically and electrochemically reversible, i.e., its potential is governed by the Nernst equation and does not change over time;
- The potential must remain almost constant when a small current flows through the electrode and reverse to its original value after such small current flow (i.e., a non-polarisable electrode).

Several electrodes come quite close to exhibit this perfect behaviour, but there is not a reference electrode that possesses all these characteristics. In general, secondary reference electrodes are electrodes of the second type, i.e., metal electrodes associated with a solubility equilibrium of a salt of this metal and an electrolyte solution with a defined concentration of the anion of the sparingly soluble metal salt. The silver/silver chloride electrode (Ag/AgCl) is the most popular because it is simple, affordable, stable, and durable. Calomel (Hg/Hg_2Cl_2), silver/silver sulphate (Ag/Ag_2SO_4), mercury/mercury oxide (Hg/HgO), mercury-mercurous sulphate (Hg/Hg_2SO_4), and copper/copper sulphate ($Cu/CuSO_4$) are also examples of secondary electrodes. In addition to these types, there are various reference systems for certain scenarios. It would be optimal if the reference electrode could be immersed in the same electrolyte solution as the electrochemical system. In the two-electrode configuration used for potentiometric measurements and the three-electrode configurations used in voltammetric and recent polarographic investigations, the reference electrode might be a second-type electrode or a metal wire (e.g., platinum). In the latter case, the potential of the metal wire may be constant during an experiment.

1.4.2 Working electrode

A working electrode is an electronic conductor in contact with an ionic conductor. The electronic conductor may be a metal, a semiconducting material, or a combination of electronic and ionic conductors. Typically, the ionic conductor is an electrolyte solution. Voltammetry electrodes are often composed of solid or liquid metals or carbon. Also utilised are metal oxides and polymers. The primary metallic conductor can be coated with a thin film of a secondary conductor (such as oxides or polymers) or a monolayer of covalently bound foreign atoms or molecules. This is what is known as chemically modified electrodes. The surface of the electrode might be chemically modified before the measurement, in a separate operation, or in situ, as an essential component of the analytical methodology. With rare exceptions, the substance employed as an electrode should not react with the solvent and

the supporting electrolyte. This condition is best addressed by noble metals, carbon glass, and graphite. Platinum and gold are the most common components of solid metal electrodes. Mercury partially fits the abovementioned condition, although it is commonly used because of its liquid state and high overvoltage for hydrogen evolution. The potential range within which the electrode may be polarised is referred to as the working window of the electrode, as only this range can be utilised for measurements. The electrode is polarised if a change in voltage does not produce any other current flow than that required for double-layer charging. This implies that there are no faradaic processes.

1.4.3 Electrochemical sensing mechanism

In instances when analysis is not feasible with a bare conductive electrode or in order to amplify the sensitivity, the electrode is modified. The kinetics of electron transport may be accelerated by modifying the conductive substrate. Surface variations have a catalytic function, and the sensitivity of measurement in electroanalytical applications is determined by an extremely small change in surface properties. Generally, modified surfaces result in:

- Physical and chemical characteristics of the modifier are transferred to the electrode;
- Due to immobilised functional groups and dopants, analyte selectivity is enhanced;
- Rapid diffusion kinetics in the case of certain materials and the capture and accumulation of an analyte at the surface of the electrode;
- Increased electrocatalytic activity as a result of the use of materials with a high surface area, allowing for increased sensitivity.

Several methods exist for modifying electrode [45], such as adding additional materials to the surface of the electrode. According to the different reactions that occur within or on the surface of a working electrode, the preparation methods required to realize a modified electrode can be divided into four categories: adsorption, covalent bond formation, electrochemical

polymerization, and electrochemical deposition, whereas screen-printing and integration are regarded as working electrodes preparation processes, not modification techniques.

Adsorption is a non-covalent interaction that holds the modified suspension to the surface of the WE. Chemical adsorption, self-assembled monolayers, and coating are all possibilities. Chemical adsorption is a simple and irreversible process for altering the electrode directly. Through natural mutual adsorption between the solid material and solution interface, the electrodes are changed. On the surface of the electrode, self-assembled monolayers are formed by physical and chemical interactions between functional groups and film-forming molecules or by the spontaneous adsorption of these groups to gold [46], silver [47], or platinum electrodes [38]. This process can improve the structural, thermal, and electronic characteristics of functional groups in order to increase binding interactions. Coating is the most frequent adsorption technique since it is simpler than the techniques described above. This procedure is carried out by combining the modified solution with the material and then applying this mixture to the surface of the bare electrode. After the solvent has fully evaporated, only a stable layer composed of the modified compounds will remain on the surface. Coating can be performed using any of the following operating techniques:

- spin coating, where the electrode is immersed in a solution, rotated using spin coating equipment, and then extracted to allow the solution to dry and create a film on its surface [48];
- dip coating, in which the surface of the bare electrode is fully immersed in the mixture and then exposed to air to remove the mixture and produce a layer [49];
- dispensing, in which a micro syringe is used to deposit a known quantity of modified droplets on the electrode surface [50].

In the process of covalent bond formation, some oxygen- containing groups bind to the surface of the electrode by oxidation and reduction reactions, and then bond to the modified substances to form carriers. Electrochemical deposition and polymerization are two similar techniques for modifying the

electrodes of an electrochemical device. Electro-polymerization is based on the deposition of polymer onto the surface of the electrode. A voltage is generally supplied to a working electrode immersed in an electrochemical cell with a monomer, the electrolyte solution and in case a doping agent. Thus, the monomer can be electrochemically oxidised to generate free radicals that induce polymerization and the deposition of the conducting polymer layer on the working electrode surface. The electrochemical polymerization process may be classified into two main categories: anodic and cathodic [51]. The anodic electrochemical polymerization is the optimal approach for creating conducting compounds by oxidising monomer species. Rarely is cathodic electrochemical polymerization used to produce conducting polymers. In fact, this form of polymerization requires electro-synthetic reductive processes that result in a relatively low yield of conducting polymers. Electrochemical deposition is an efficacious approach for creating metal nanoparticles, but it is often employed less frequently than wet-chemical techniques. This method can occasionally exhibit restrictions in terms of nanomaterial dimensions and permitted morphologies, but it has several advantages, including a short synthesis time, the absence of chemical reductants or oxidants, and the absence of unwanted by-products. In addition, when the modifier film is put directly on the electrode, higher adhesion can be achieved [52].

1.5. Electrode materials

In electrochemistry, graphene and its derivatives, such as graphene oxide (GO), reduced graphene oxide (rGO), and three-dimensional (3D) graphene, are frequently employed. Typically, carbon-based materials combine a low price, a high surface area, good electrical conductivity, and strong electrocatalytic activity and therefore they have demonstrated good performance [53] in heavy metals detection. In addition, being this type of materials modified (or doped) with different types of additives such as metals, metal oxides, etc., they are often used as a base for electrochemical sensors.

Since noble metal nanoparticles (M-NPs) have high catalytic activity via the size effect, graphene modified with these M-NPs has been exploited for the

detection of heavy metal ions. Additionally, the catalytic process may be sped up by graphene's ability to transmit electrons obtained from the M-NPs' catalytic activity to electrodes. When combined with graphene, gold nanoparticles (Au-NPs) are the most common NPs used to detect metal ions. This is because Au-NPs are chemically stable and easy to make. For example, Lee et al.[54] synthesized via electrodeposition G/Au-NPs on a glassy carbon electrode(GSE), to determine trace of Pb^{2+} in acetate buffer solution using square wave anodic stripping voltammetry. Instead, Sang et al.[55] synthesized rGO/Ag-NPs and realized by a coating, starting with a magnetic glassy carbon electrode, a highly sensitive electrode for simultaneous detection of HMI. But expensive materials like Au and Ag aren't very useful when making macroelectrodes, which require a large amount of material. Alternatives like tin NPs or bismuth NPs have also been employed to heavy metal ion identification. Lee et al. show in their study [56] how to make a new graphene/bismuth nanocomposite film-modified glassy carbon electrode by electrochemically depositing exfoliated graphene oxide and plating bismuth film in place. This makes it possible to find trace amounts of zinc, cadmium, and lead ions.

Due to their large surface areas and high electrocatalytic activity, metal oxides are often used instead of M-NPs and metal films to detect heavy metal ions. Strong adsorption capacity, electrocatalytic activity, or both simultaneously are the sensing mechanisms of metal oxide for heavy metal ions. The majority of metal oxides, however, have poor conductivities and stabilities, which are unfavourable to electron transport during the detection process and reduce the electrode's long-term stability. But, when metal oxide and graphene are mixed, a new electrochemical platform for heavy metal ion detection is expected. Graphene nanocomposites based on Fe_3O_4, ZnO, MnO_2, Cu_2O, Fe_2O_3, SnO_2, TiO_2, and Co_3O_4 have so far been effectively used to detect heavy metal ions in aqueous solution [57]. The performance of the modified electrode can be significantly impacted by the morphology and average size of the metal oxide. By using a simple one-pot synthesis method, Xiong et al. [58] produced reduced graphene oxide-Fe_3O4 nanocomposites with small-sized Fe_3O_4. They

deposited the material obtained on a previously treated GSE using a dispensing technique, and the analysis of Cd^{2+}, Pb^{2+} and Hg^{2+} was performed by square wave anodic stripping voltammetry (SWASV). Another example of the use of metal oxides combined with graphene derivatives is illustrated by Wei et al. [59]. In their work, the authors give a thorough analysis of the SnO_2/rGO nanocomposite modified glass carbon electrode, which could be used for the simultaneous and selective electrochemical detection of ultra-trace Cd (II), Pb (II), Cu (II), and Hg (II) in drinking water.

1.5.1 Electrospun nanofibers

Numerous electrospun materials for the detection of heavy metal ions have been developed and evaluated using a wide variety of techniques [41]. Electrospun nanofibers have numerous advantageous characteristics, including a high surface-to-volume ratio, porosity, tunability of nanofiber properties (chemical composition, morphology, and dimensions), and the ability to be easily functionalized to enhance material performance [60]. The functional sites on which fibers can be endowed, through the different functionalization or doping methods, promote the activation of anchor points for HMI. Moreover, the high surface area to volume ratio of fibers conveys a broader dispersion of active sites, which, along with the porous structure of fibrous membranes, assesses the heavy metal removal capability of the electrospun[61]. Therefore, it has been demonstrated that the integration of nanomaterials as electrodes can improve the sensitivity and reproducibility of electrochemical methods in the detection of HMI [62]. When polymeric nanofibers are considered, polyaniline conductive polymer was found to be among the most used sources. Indeed, it played a dual role in both increasing the surface area, due to the mono-dimensional structure, and assuring at the same time a high conductivity due to the well-known electronic properties. Promphet et al. [63] reported electrospun nano-porous fibers fabricated by mixing graphene, polyaniline, and polystyrene and deposited onto carbon electrodes. The system was tested under SWASV for the simultaneous determination of Pb^{2+} and Cd^{2+} ions in the presence of Bi^{3+} ions. The observed increase in the electrochemical sensitivity

of modified electrodes (observed in comparison to unmodified ones) was ascribed to an increase in the specific electrode surface area because of the presence of nanofibers. The electrode system showed high reproducibility and was successfully applied in real river water samples, demonstrating that it is a useful tool for the environmental monitoring of these ions with a detection limit for Pb^{2+} and Cd^{2+} down to 3.3 and 4.43 μg/L, respectively.

Huang et al. [64] used one-dimensional phytic acid-doped polyaniline nanofibers as a modifier for GCE for simultaneous detection of Cd^{2+} and Pb^{2+} using DPASV. The reported detection limits were 0.02 and 0.05 μg/L for Cd^{2+} and Pb^{2+}, respectively. The fabrication and evaluation of a glassy carbon electrode modified with self-doped polyaniline nanofibers/mesoporous carbon nitride and bismuth for the simultaneous determination of trace Cd^{2+} and Pb^{2+} by SWASV were reported by Zhang et al. [65]. Under the optimum conditions, the fabricated electrode exhibited a limit of detection (LOD) of 0.7 nM for Cd^{2+} and 0.2 nM for Pb^{2+}. Both individual and simultaneous detection of Pb^{2+} and Cd^{2+} were afterward investigated on polyaniline nanotubes/electrospun polystyrene surface [66]. The morphological and electrochemical properties of the polyaniline nanotubes were demonstrated to depend on the size of the polystyrene fibers.

Good sensitivity and reproducibility were demonstrated by SWASV. The LOD was found to be 9.65×10^{-11} mol/L and 2.67×10^{-10} mol/L for the individual detection of Pb^{2+} and Cd^{2+} ions, respectively. Simultaneous detection of Zn^{2+}, Cd^{2+}, and Pb^{2+} using a graphene–polyaniline nanocomposite electrode was investigated by SWASV in the presence of Bi^{3+}. Metal ion concentration with detection limits of 1.0 μg/L for Zn^{2+} and 0.1 μg/L for both Cd^{2+} and Pb^{2+}. The modified electrode allowed selective determination of the target metals in the presence of common metal interferences including Mn^{2+}, Cu^{2+}, Fe^{3+}, Fe^{2+}, Co^{3+}, and Ni^{2+}[67]. Field monitoring of HMI pollution for the detection of Hg^{2+} was demonstrated by Naourei et al. [68]. Mercury ions were quantified by ASV using a novel conductive nanofibrillar structure made of a copolymer, poly(aniline-co-o-aminophenol) decorated with gold nanoparticles, with a very low LOD of 0.23 nM. The sensor resulted efficient in Hg^{2+} detection in river

water and in fish samples. Along with electrospun polyaniline, another commonly reported system is based on carbon nanofibers, which is considered a system with a remarkable surface area. Li et al. [69] constructed a bismuth-film modified graphite nanofibers–Nafion GCE for the simultaneous determination of trace Pb^{2+} and Cd^{2+}. The electrochemical properties of the modified electrode, studied under optimal conditions, showed the LOD equal to 0.09 µg/L for Cd^{2+} and 0.02 µg/L for Pb^{2+} with a 10 minutes preconcentration by DPASV.

High reproducibility and selectivity in both real, such as river water, and human blood samples were demonstrated. The same metals, generally reported as representative metals, were also used by Zhao et al. [70] to test through the same electrochemical technique the performance of a carbon-based fibers/Nafion modified electrode, resulting in a LOD equal to 0.9×10^{-9} M and 1.5×10^{-9} M, for Pb^{2+} and Cd^{2+}, respectively. A Nafion-modified glassy carbon electrode was constructed for anodic stripping analysis of Hg^{2+}, combining bis(indolyl) methane with the unique properties of mesoporous carbon nanofiber, with a satisfactory result in HMI coexistence (Hg^{2+}, Cd^{2+}, Pb^{2+}, and Cu^{2+}). This electrochemical sensor significantly improved selectivity and sensitivity towards Hg^{2+} determination with a detection limit of 0.3 nM [71]. Glutathione peptide was successfully immobilised onto a nanomaterial substrate electrode based on carbon nanofiber. The repeatability, reproducibility, and analytical performance were compared to a classical screen-printed carbon electrode modified with glutathione. It was demonstrated that the enhanced surface area attributed to the carbon nanofiber substrate gave higher results for Pb^{2+} and Cd^{2+} determinations [72]. A facile, green, highly sensitive, and simultaneous method for the detection of trace HMI was demonstrated by Zhang et al.[73]. Well dispersed gold nanoparticles were grown on carbon nanofibers synthesised via the electrospinning technique and exhibited a high surface-specific area and high porosity. When used as the working electrode for the simultaneous determination of HMI such as Cd^{2+}, Pb^{2+}, and Cu^{2+} through the SWASV method, those properties resulted in being beneficial for the penetration of heavy metal ion solutions and increasing the

surface contact area of the electrode. Simultaneous detection of Cd^{2+}, Pb^{2+}, and Cu^{2+} with a low concentration of 0.1 mM was attributed to the exposed well-dispersed gold nanoparticles and the high electron transport capability of carbon nanofibers. Vertically aligned carbon nanofibers were evaluated for the detection of Pb^{2+} by ASV by Robinson et al. [74].

The achieved detection limit reported was 1.73 nM. A nanocomposite of polypyrrole and carbon nanofibers modified carbon paste electrode was reported for the determination of traces of lead ions in real samples of water. The SWASV was used to investigate the analytical performance of the designed electrode. Under the optimum experimental conditions, good linearity between the stripping peak currents and the concentration of Pb^{2+} was obtained with a detection limit estimated at around 0.05 μg/L [75].

Another study describes a simple and efficient method for creating new sensors for simultaneous tracing detection of HMIs. Bimetallic platinum-gold alloy nanoparticles were constructed with electrospun carbon nanofibers for simultaneous detection of trace Cd^{2+}, Pb^{2+}, and Cu^{2+} by SWASV with a sensitivity of 0.10 mM. The excellent sensitivity and low detection limit for HMI detection were ascribed to the high conductivity of carbon nanofibers, the fast response of platinum-gold alloy nanoparticles, and the high specific surface area of the hybrid structure [76].

Porous carbon nanofibers co-doped with nitrogen and sulfur were used to modify a glassy carbon electrode. Compared to a bare GCE, the one modified shows improved sensitivity for Cd^{2+} in DPASV [77]. A novel elaborated electrochemical sensor was investigated, which was based on a nanocomposite of ionic liquid, 1-ethyl-3-methylimidazolium bis(trifluoromethyl sulfonyl) imide, carbon nanofibers, and bismuth particles modified carbon paste. The sensor exhibited excellent electroanalytical performance for the determination of Pb^{2+} and Cd^{2+} with LOD for Pb^{2+} and Cd^{2+} equal to 0.12 and 0.25 μg/L, respectively. A wide linear response range and low LOD were obtained, along with high sensitivity, selectivity, and reproducibility [78].

A trace amount of As^{3+} detection was instead reported by using a sensing platform made of a polyaniline nanosheet array on an electrospun iron-

containing carbon nanofiber substrate followed by self-deposition of gold nanoparticles. High sensitivity with a detection limit of 0.5 ppb was registered by SWASV [79].

A few other reports have reported on other kinds of pure, hybrid, and composite nanofibers for multiple HMI detection. Reduced graphene oxide/polyvinyl butyral nanofibers on glassy carbon electrodes were used for fabricating an electrochemical sensor for Cu^{2+} detection by DPASV. The as-fabricated sensor showed good analytical performance with a low detection limit of 4.1 nM [80].

Zinc oxide nanofibers with high surface area, fabricated by electrospinning, have demonstrated optimum sensitivity for Cd^{2+} and the simultaneous analysis with Cu^{2+}, Pb^{2+}, Cd^{2+}, and Hg^{2+} is feasible in water samples. The strong affinity between zinc oxide and Cd^{2+} was exploited by SWASV and the reported LOD was equal to 1.8 x 10^{-9} mol/L [81]. A zinc oxide nanofiber/L-cysteine nanocomposite was used as electrodes for the electrochemical sensing of Pb^{2+} ions. The high porosity of nanofibers combined with the Lewis acid-base interaction of L-cysteine makes it a great material for Pb^{2+} detection in a real sample. SWASV displayed excellent sensitivity, selectivity, and stability with a LOD of 0.397 μg/L [82].

To test Cu^{2+} ion contamination in real environmental samples, an amino-rich organosilica-nanofiber-modified gold electrode was obtained upon electrospinning. The three-dimensional porous fiber promoted Cu^{2+} ions accumulation inside the structure. By using SWASV, a very sensitive response to Cu^{2+} ions was obtained, with a wide linear range, high stability, and a low detection limit down to 2.6 pM [83].

Finally, it is noteworthy to highlight that, as inferred by the analysed literature, the pivotal role in the sensing mechanism of HMIs by ASV was strictly dependent on the material features. Despite a very broad diameter distribution ranging from 40-60 nm [64] to 2.44 μm [63] for the reported cases, the high surface area to volume ratio of fibres and membrane porosity were always ensured for each system due to different electrospun fibres (such as pure, hybrid, doped, and functionalized).

2

Electrochemical Impedance Spectroscopy (EIS)

This chapter describes in detail the electrochemical impedance spectroscopy technique, including its instrumentation, the influence on measurement parameters, the graphical representation of results, and the equivalent circuits usually used.

Electrochemical impedance spectroscopy is an important electrochemical technique used to measure the impedance of a circuit. EIS has several advantages over the other electrochemical methods since it is a steady-state technique, uses small signal analysis, and can probe signal relaxations over a very wide range of applied frequency, from less than 1 mHz to greater than 1 MHz, using commercially available electrochemical working stations (potentiostat).

2.1 Instrumentation

In the process of developing the EIS measurement technique, instruments with various measurement principles, such as alternating current bridges, phase-sensitive detection and lock-in amplifiers, Lissajous curves, frequency response analyser (FRA), wavelet transforms and Laplace transforms, have been proposed. Most of the contemporary EIS devices use frequency response analysers, coupled with a potentiostat/galvanostat, to calculate the real and imaginary components of the complex impedance at a specified frequency.

As well described by Orazem and Tribollet [84], a potentiostat is designed to maintain a constant potential difference between a working electrode and a reference electrode. **Figure 4(a)** depicts the simplest connection of the reference electrode to the inverting input of the operational amplifier. The potential of the working electrode is referenced to the ground potential, and

the potential of the reference electrode is maintained at a value V_{set} that is also referenced to the ground potential. **Figure 4(a)** shows a potentiostat that regulates the voltage difference between the working and reference electrodes. Additionally, the potentiostat requires a method for monitoring the current. **Figure 4(b)** illustrates one method for measuring the potential difference across a resistance. Current is represented by $I = V_m/R_m$. The current in the working electrode circuit is measured using a current follower in the second method (see **Figure 4(c)**. In the last case, the working electrode is not directly connected to the ground but is instead at a virtual ground potential. In each of the **Figure 4** combinations, the working electrode's potential is regulated relative to the reference electrode. The reference electrode is at ground, and the potential V between the + input of the operational amplifier and ground represents the potential difference between the reference electrode and the WE. There is no potential difference between the entries + and -. The operational amplifier delivers the current through the counter electrode so that the reference electrode and the WE have the corresponding potential difference.
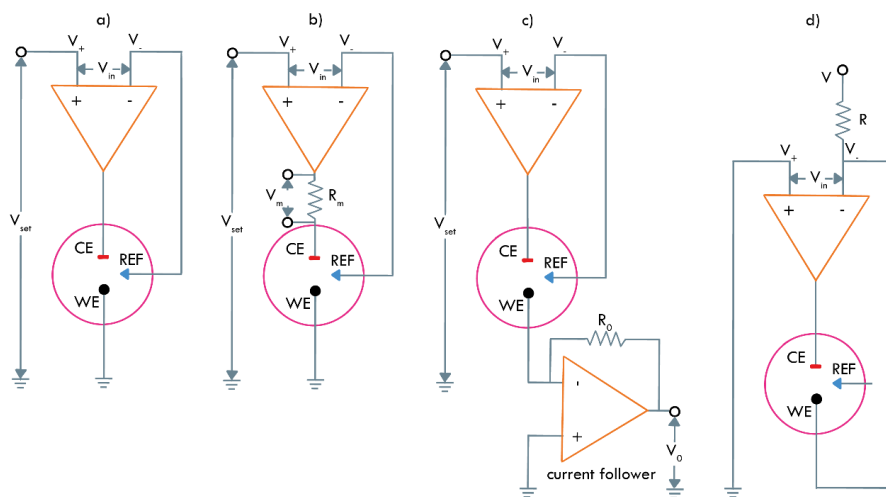
Figure 4 - Simple electric schemes of a) potentiostat for controlling the potential of a working electrode with respect to a reference electrode, b) potentiostat with current measurement by potential drop across a measuring resistor, c) potentiostat with current measurement by use of a current follower and d) galvanostat for controlling the current through a working electrode. Adapted from [84].

A galvanostat scheme is shown in **Figure 4(d)**. Point A and the working electrode are both at a virtual ground potential. The current I is obtained by

the equation I = V/R. Either R or V could be modified to modify the current value. The potential between the reference electrode and the working electrode is easily observable.

$$V_0 = R_0 \left({V_1}/{R_1} + {V_2}/{R_2} \right) \quad (2)$$

By modifying the potentiostat as represented in **Figure 4(c)**, it is possible to conduct impedance measurements under potentiostatic control. In **Figure 5**, a voltage adder is used to combine the DC potential corresponding to the polarisation point and the ac potential supplied by the frequency function analyser's generator. With an appropriate choice of R_0, R_1 and R_2 in equation (2), it is possible to have an AC input with a potential divided by 100 (e.g., $R_0 = R_1 = 100R_2$).
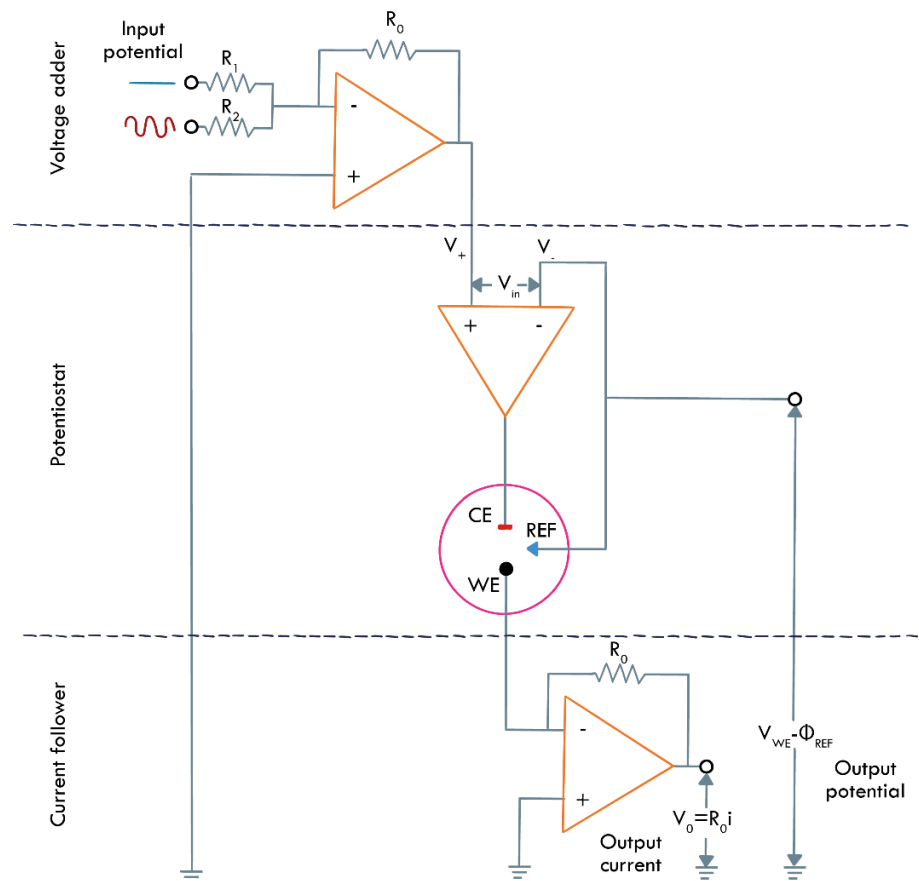
Figure 5 -Electric scheme of potentiostat for EIS measurement. Adapted from [84].

2.2 Experimental Considerations

The experimental design parameters are affected by the system under examination, the purpose of the investigation, and the instrumentation's capabilities. The aim is to optimize the information content of a measurement while avoiding bias and stochastic errors.

Typically, the purpose of impedance measurements is to capture the frequency response of the system under investigation. To achieve this, the measured frequency range must contain frequencies sufficiently large and sufficiently small to reach asymptotic limits where the imaginary impedance approaches zero. In certain instances, such as when blocking electrodes are utilised, the low-frequency asymptotic behaviour does not exist. Due to the nonstationary nature of the system, a true DC limit cannot be achieved in other scenarios. At high frequencies, instrument artefacts may affect the performance. Instead, the potential determines the linearity of electrochemical systems. Utilizing a perturbation with small amplitude permits the application of a linear model to the interpretation of spectra. The optimal amplitude is a balance between the desire to minimise nonlinear response (by selecting a small amplitude) and noise in the impedance response (by using a large amplitude). The amplitude is dependent on the investigated system.

2.3 Instrumentation Parameters

Measurements of impedance necessitate a trade-off between minimising bias errors, limiting stochastic errors, and maximising the information content of the resulting spectrum. To limit the impact of stochastic errors in impedance measurements and to improve signal-to-noise ratio, the following actions could be taken:

- *Use the optimal current measuring range*: the potentiostat converts the current into a potential signal. Potentiostats may utilise an alternative version of the current follower. A mismatch between the measured current and the potentiostat's range setting can result in either excessive

stochastic noise (if the range is set too high) or bias errors due to current overloads (if the set range is too low). Some instrument manufacturers require the operator to estimate the appropriate current measuring range. For studies conducted with DC current, estimating the current range is straightforward. Under open-circuit conditions, the range of required current varies significantly with frequency. Automatic selection of the current measuring range is avoided if the method may produce a change in system attributes by imposing a current on the system.

- *Increase the integration time/cycles*: for impedance measurements, time-domain data are converted to complex values for each frequency. This measurement's stochastic errors can be decreased by allowing more time for integration at each frequency. The number of cycles necessary to reach a predetermined error threshold at each frequency depends on the measurement frequency. At high frequencies, several cycles are necessary, whereas at low frequencies, only three or four cycles are required. Some instruments permit the configuration of autointegration modes in which the system decides the required number of cycles to converge to a specific criterion. Selecting the more stringent convergence criterion helps lower the noise levels.

- *Ignore the first frequency measured*: a starting transient frequently corrupts the recorded impedance at the initial frequency of measurement. When fitting regression models to data, it is preferable to exclude the initial frequency measured.

- *Increase the amplitude of modulated signal*: the size of the modulation amplitude that can be utilized while maintaining a linear system response is determined by the system's polarisation curve. Numerous high-impedance systems exhibit a reasonably large linear potential range. By employing a large modulation amplitude in such scenarios, stochastic mistakes can be considerably decreased.

- *Introduce a delay time*: measurements of impedance are performed at a sinusoidal steady state, meaning that the sinusoidal response to the

sinusoidal input does not vary with respect to time. As the system responds to a change in frequency, a transient is observed, and this transient is incorporated into the impedance's integrated value. According to Pollard and Compte [85], this transient can generate an error of up to 4% in the impedance response measured by integration over the first cycle. To prevent this unwanted inaccuracy induced by the transient, it is preferable to introduce a one or two-cycle delay between the frequency change and impedance measurement.

- *Avoid the frequency of the electric line and its first harmonic*: modern impedance instruments offer extremely effective filters for stochastic noise, but these filters are typically insufficient for measurements conducted at the electric line frequency (i.e., 50 ± 5 Hz and 100 ± 5 Hz in Europe and 60 ± 5 Hz and 120 ± 5 Hz in the United States). In general, the resulting measurements appear as outliers in an impedance spectrum, and such outliers have a substantial effect on the nonlinear regression used to extract parameters from the data.

- *Avoid exposure to external electric fields*: electric fields emitted by external devices such as electric motors, pumps, and fluorescent lighting can significantly contribute to the apparent noise in a system. This effect, which is most evident in high-impedance systems, can be reduced by using a Faraday cage, which will be discussed in detail below.

Systematic bias errors in impedance measurements can be reduced by acting on the parameters described below. The bias errors caused by non-stationary effects have a greater influence at low frequencies, where each measurement requires considerable time.

- *Reduce measurement time*: reducing the time permitted for integration at each frequency increases the degree of stochastic errors in the measurement, hence reducing the total time needed to measure an impedance spectrum. This solution requires the acceptance of additional stochastic noise in order to obtain a smaller bias error. Minimizing the frequency range or the number of frequencies monitored every decade is a second method for reducing the number

of frequencies measured. Since a greater number of observed frequencies generates more accurate parameter estimates, this method necessitates sacrificing model discrimination to achieve a smaller bias error.

- *Select an appropriate modulation technique*: the presence of bias errors can be significantly affected by the selection of an appropriate modulation strategy. Utilizing potentiostatic modulation in a system where the potential varies with time can increase the measurement time for autointegration. The user may consider what must remain constant (e.g., potential or current).

- *Avoid the frequency of the electric line and its first harmonic and introduce a delay time*: to minimize bias errors, it is possible to employ the same approach as previously described.

Instead, at high frequencies, especially for systems with a low impedance, instrument bias errors are frequently observed. To reduce this type of error, it is possible to proceed with the following steps:

- *Use a Faraday cage*: a Faraday cage consists of a metallic conductor that completely covers and shields the cell under study from the influence of external electric fields. The conductor may consist of a wire mesh or metal sheets. The cage is typically grounded. For systems with a high impedance and a low electrical current, Faraday cages are required. The wires operate as an antenna, accumulating stray electric fields that induce an additional current. If the cell current is tiny, this current may constitute a substantial percentage of the signal.

- *Use faster potentiostat*: the effect of high-frequency bias errors can be lessened by selecting an appropriate potentiostat. Different brands of potentiostats are capable of high-frequency measurements to varying degrees.

2.4 Graphical representation of results

The representation of data is a crucial feature of EIS analysis, upon which interpretation depends. Potential–current versus time, Lissajous curves, and Bode and Nyquist representations are frequently used [86]. The first data representation mentioned above is the relationship between the sinusoidal potential and current as a function of time at a specific frequency. The amplitude and phase shift provide essential impedance data information. In the Lissajous curve, which is created by showing the output signal as a function of the input signal at a certain frequency, the phase shift between the input and output signals is more evident. In the early years of EIS, Lissajous plots were employed to examine EIS at both low and high frequencies. In addition, the Lissajous plot provides numerous advantages when observed during the experiment. If Lissajous figure distortions are seen, the perturbation amplitude applied to the system must be decreased, at least in the frequency domain where the ellipse degeneration is observed. The measurement is considered linear if the Lissajous plot can be produced an elliptical form by altering the perturbation amplitude. Moreover, a change of the electrical signal along the x or y axis, which typically occurs in the low-frequency region, indicates a movement of the system to a non-stationary condition, resulting in an inaccurate measurement in this frequency domain. In contrast to the Lissajous curve, the Bode and Nyquist representations are obtained over a wide frequency range (typically 100 kHz to 10 mHz) and are thus 3D representations of the experimental results, namely frequency, modulus, and phase angle for the Bode diagram, or frequency, real part, and imaginary part for the Nyquist diagram. The most common in the literature, the Nyquist and Bode representations permit a preliminary study of the system, leading to the identification of elementary processes engaged in the mechanism. The phase angle and modulus are displayed as a function of frequency in a typical Bode graph. The phase angle and modulus are calculated from the measurements' real and imaginary components. The Bode plot is an understandable representation of the frequency-dependent impedance change. A typical Nyquist plot in which the imaginary part of the impedance data is shown

against the real part. The Nyquist format highlights greater impedance values that demonstrate the effect of mass transfer and reaction kinetics. Each symbol represents a data point measured at a particular frequency, and solid dots represent typical frequencies.

2.5 Equivalent Circuits

In general, an electrochemical cell can be thought of as a simple impedance to a small sinusoidal excitation, thus, its performance should be represented by an equivalent circuit of resistors and capacitors that pass current with the same amplitude and phase angle as the real cell does under a given excitation. Several models were constructed for the impedance response based on hypotheses concerning reaction sequences, mass transfer, and physical processes. Frequently, these models can be described using the mathematical formalisation of electrical circuits. Because the total current through the working interface is the sum of contributions from the faradaic process (i_f) and double-layer charging (i_c), parallel elements are introduced. The impedance response of electrochemical systems can also be accounted for via electrical circuits. These models are formed by passive elements such as resistors, inductors and capacitors, and by distributed elements such as the Warburg element in **Table 2**.

2.5.1 Resistors

Various and frequently contradictory physical explanations are provided in the literature for the experimental data represented by the Nyquist diagram [87]. These interpretations are dependent on the results of the various EIS applications, such as for Nyquist plots with one or two semicircles. Some examples of the use of resistance to describe electrochemical phenomena are:

- *Ohmic or uncompensated resistance:* represents the voltage drop between the working and reference electrodes. At high frequencies, its value is determined by the intersection of the measured impedance and the abscissa of the Nyquist diagram. The ohmic resistance is generally

expressed as R_Ω or R_S and depends on the geometry of the working electrode and the conductivity of the electrolyte solution.

- *Polarization resistance*: polarizing an electrode means applying an external potential, modifying the equilibrium that occurs in open circuit conditions (OCV). The polarization of an electrode causes a current flow on its surface and in the electrolyte, which the system generates to restore a condition of equilibrium. In the study of corrosion of metallic materials, a high value of the polarisation resistance indicates a high resistance to corrosion of the material. The value of the polarization resistance is obtained by subtracting the ohmic resistance from the resistance value, given by the impedance projection on the axis of real values at low frequency. The polarization resistance is mainly given by the sum of the charge transfer resistance (R_{ct}) and the diffusion resistance (R_d). The latter will be discussed in the paragraph relating to the elements that model the diffusion phenomenon. As for the charge transfer resistance, it represents the faradaic impedance limit for frequency, which tends to infinity and for the AC wave amplitude, which tends to zero [88]. In the simplest cases, it corresponds to the ohmic resistance value, while in the cases of more complex reactions, it will be the place where the mid-frequency loop reaches the real axis.

2.5.2 Inductors

Generally, the results of impedance spectroscopy are always represented within the first quadrant of the Nyquist diagram, but on some occasions, it can drop below the x axis, therefore into the fourth quadrant. In order to represent this type of behaviour, the inductor element is used during the modelling of the equivalent circuit. Inductive phenomena can occur at both high and low frequencies. In the first case, they are due to instrumental artifacts, to the structure of the working electrode (for example, sandwich or with a wound wire) or to the incorrect position of the reference electrode with respect to the working one (usually it is advisable to position the reference electrode at a distance of two-three times the size of the WE) [89]. As for the structure of the

working electrode, it is often at a certain distance from the connection with the potentiostat, so for WE with low impedance, the inductive loop is more marked. While the inductive loop that occurs at low frequencies is normally found in EIS analyses of PEMFCs (Proton-Exchange membrane fuel cells)[90].

2.5.3 Capacitors and Constant Phase Element

In an electrochemical system, the presence of a capacitive component may be due to dielectric capacitance and double layer capacitance. Electrical double layer capacitance (C_{dl}) refers to the polarisation of ionic charge at the surface of EIS system electrodes. The first occurs when there is a dielectric layer on the electrode's surface, such as in the presence of oxide layers or polymeric coatings. The value of the double layer capacitance depends on various elements, such as electrode potential, temperature, ionic concentrations, ion types, oxide layers, electrode roughness, impurity adsorption, etc. Due to the presence of so many variables, the behaviour of an ideal capacitor almost never occurs; therefore, a constant phase element (CPE) is used to model the equivalent electrical circuit in these cases. CPE is utilized to optimize data fitting but has no physical significance. Typically, the equation (3) for calculating the impedance of this element contains two constant-phase parameters, Q_0 and n. When n = 1, this corresponds to an ideal capacitor, when n = 0, to an ideal resistor, and when n = -1, to an ideal inductor.

$$Z_{CPE} = \frac{1}{Q_0(j\omega)^n} \ (3)$$

Among the proposed physical explanations for CPE behaviour is electrode roughness. For a fractal surface with a rough surface, the fractal dimension (D) is between 2 and 3. This indicates that the surface varies between two dimensions (i.e., it is perfectly flat) and three dimensions (i.e., the surface fills three dimensions, branching every which-way through space and resembling a porous cube). It has been shown [91] that an exponent, n = 1/(D-1), affects the interfacial impedance (electron transfer or double layer capacitance) of these electrodes. For a smooth surface, the fractal dimension (D) is 2.0, n = 1,

and the impedance value remains unaltered, however for a severely contorted surface (D = 3) and n = 0.5, the impedance value is unaffected. Another explanation is heterogeneous surface reaction rates. This may be observed on polycrystalline metal surfaces or carbon electrodes with a distribution of active sites (with various activation energies). Kim et al. [92] show that for a glassy carbon electrode, the CPE exponent corresponds with the proportion of edge plane orientation rather than the fractal dimension of the surface. This behaviour is not seen with mercury which, unlike polycrystalline metals, is atomically homogenous and does not exhibit CPE behaviour. A third possible interpretation could be the coating's variable thickness or composition. For instance, if the bulk conductivity of a coating varies with distance through the coating [93] , the resulting impedance spectrum can be approximately like that of a CPE.

2.5.4 Diffusion elements

In electrochemical reactions, diffusion plays an essential role. The first distributed element to be introduced to electrochemistry was the infinite-length Warburg impedance. The infinite-length Warburg impedance is derived from the solution of Fick's second law, the diffusion equation, for one-dimensional diffusion of a particle in a semi-infinite space, which is mathematically equivalent to wave transmission on a semi-infinite distributed RC transmission line [94] .However, actual physical circumstances never include infinite lengths. The solution for the diffusion of particles in a finite-length region (equivalent to a finite-length, shorted transmission line) seems to have been presented for the first time by Llopis et al. [95] for the supported situation, where the finite length considered was the thickness of the Nernst diffusion layer, suitable for a stirred electrolyte or a rotating electrode. In contrast, particles diffusing in an electrode with a thickness of l_e or in an electrolytic cell of unstirred liquid or solid material are free to migrate over the full region of thickness l_e or l. In cases of current interest, it is fair to consider the finite-length zone where diffusion occurs to be l or l_e. Therefore, the Warburg element can be utilized to model a semi-infinite, unrestricted linear diffusion to a wide planar electrode. The

Warburg impedance is an example of a constant phase element whose phase angle is $-\pi/4$ and is independent of frequency. As expected for a CPE with an n-value of 0.5, the amplitude of the Warburg impedance is inversely proportional to the square root of the frequency. The Warburg is unique among CPEs in that the real and imaginary components are identical at all frequencies and are frequency dependent. The following equations (4) define a Warburg Impedance:

$$Z_W = \sigma/\sqrt{\omega} - j\sigma/\sqrt{\omega} \quad (4)$$

Where σ is given by:

$$\sigma = \frac{RT}{n^2 F^2 A \sqrt{2}} \left(\frac{1}{D_O^{1/2} C_O^b} + \frac{1}{D_R^{1/2} C_R^b} \right) \quad (5)$$

Both reversible and quasi-reversible processes in which both components are soluble satisfy the equation for sigma. The subscripts O and R describe the oxidized and reduced forms of the species, respectively, while C^b indicates the concentration in bulk. D is the species' diffusion coefficient. The Warburg coefficient can also be derived from the slope of the Nyquist plot or by fitting to an equivalent circuit model containing a Warburg impedance. However, most identical circuit modeling algorithms yield Y_O instead of σ. Y_O denotes the admittance magnitude (= $1/Z$) at $\omega = 1$ rad/s (0.16 Hz).
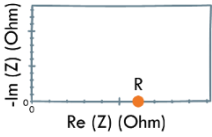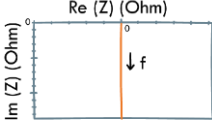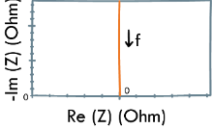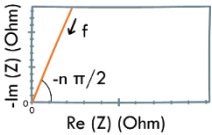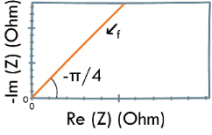
$$\sigma = \frac{1}{\sqrt{2}Y_O} \left[ohm/\sqrt{s} \right] \quad (6)$$

The Gerischer impedance is a distributed element that shares several characteristics with the Warburg impedance, which occurs when an electroactive species performs a bulk chemical reaction. In the high frequency limit, the Gerischer function is indistinguishable from the finite-length Warburg, and like it, it yields purely resistive behaviour in the low frequency limit. However, the Gerischer function differs from the finite-length Warburg in its detailed frequency dependence, yielding, for example, an arc closer to the real axis in the Z plane. Similar to the infinite length Warburg impedance, the Gerischer impedance can be represented by a semi-infinite transmission line

with a series resistance per unit length and a parallel resistance per unit length added to the transmission line capacitance per unit length.

Table 2 - Circuit elements used in EIS modelling.

Circuit Element	Symbol and Equation	Nyquist plot
Resistor (R) Represents the transfer of electrons across an interface	$Z = R$	
Inductor (L) Represents magnetic inductance	$Z(f) = Lj2\pi f$	
Capacitor (C) Represents non-faradaic charging at an interface	$Z(f) = 1/(Cj2\pi f)$	
Constant Phase Element (CPE) Represents a non-ideal capacitor	$Z(f) = 1/[Q(j2\pi f)^n]$	
Warburg semi-infinite diffusion (W) Represent diffusion of ions/electrons in solid o liquid phases	$Z(f) = \sqrt{2}\sigma/\sqrt{j2\pi f}$	

Warburg convective diffusion (Wd) Represents diffusion on a rotating disk electrode in a finite length	$$Z(f) = R_{d1}\tanh(\sqrt{\tau_{d1}j2\pi f})/\sqrt{\tau_{d1}j2\pi f}$$	
Gerischer element (G) Represents an electrochemical reaction coupled with an irreversible chemical reaction, also coupled to diffusion. It has also been used to model a porous electrode	$$Z(f) = R_{G1}/\sqrt{1 + \tau_{G1}j2\pi f}$$	
Modified Gerischer element (Gα) Derived from the Gerischer diffusion element expression by adding the parameter α_1	$$Z(f) = R_{G1}/\sqrt{1 + (\tau_1 j2\pi f)^{\alpha_1}}$$	
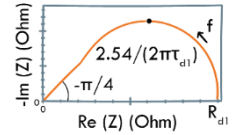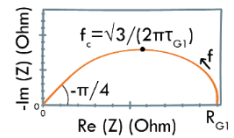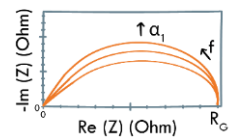
2.5.5 Common Equivalent Circuits

In the following section, common equivalent circuit models are shown. These models can be utilized to analyse simple EIS data. The first model is purely capacitive and is employed when an electrode is covered with an undamaged coating and therefore has a very high impedance. The model combines a resistor (due mostly to the electrolyte) in series with the coating capacitance. The corresponding Nyquist plot for such a perfectly polarized

electrode will have a straight vertical intersecting the Re(Z) axis, with the X-intercept representing the resistance. Due to the porosity, roughness, and impurity of the electrode, it is possible to observe the straight line intersecting the Re(Z) axis at an angle less than 90°. Consequently, CPE will replace the ideal capacitor in the equivalent circuit [96]. The second example is the simplified Randles circuit, which is one of the most used cell models. This model includes a double-layer capacitor with solution resistance and charge-transfer or polarization resistance. The polarization resistor is connected in parallel with the surface deposited double layer capacitor and in series with the solution resistor. The Nyquist plot of a simplified Randle cell is always a semicircle. The solution's resistance can be calculated by reading the real axis value at the high frequency intercept. At the opposite (low frequency) intercept, the real axis value is the sum of the polarization resistance and the solution resistance. In cases where semi-infinite linear diffusion influences the kinetic and diffusion control of an electrochemical system, the Warburg impedance is utilized in the equivalent circuit model and the Nyquist plot results in a semicircle with one extended arm at low frequency. Similarly, more sophisticated models can be built based on the physical characterization of the electrode, such as a partially blocked electrode, an electrode covered with an inert porous layer, a totally porous electrode, an electrode coated with numerous layers of inert porous layers, etc., as described in detail in previous reviews on EIS measurements [97], [98].

The state of the art described up to now, regarding the detection techniques for heavy metals and the different types of sensors, has served to better contextualize the work described in this thesis.

3

Methods for production and characterization of active layers for sensor device

In this chapter, the general principles behind the experimental equipment and techniques used for this research are outlined. The first paragraph describes the electrospinning technique, all the parameters that influence it, and the characterization techniques used.

3.1 Electrospinning technique

Electrospinning is a straightforward process that has the potential to be the most successful and advanced electrohydrodynamic method for producing continuous fibres with diameters as small as few nanometres. It possesses characteristics similar to those of two standard methods, namely conventional dry or melt spinning and electrospraying. Applying high voltage to induce the production of a liquid jet, which is quickly solidified by evaporating the solvent or freezing the melt, enables the manufacture of nanofibers. This versatile technique is applicable to both natural and manufactured polymers, polymer alloys, ceramics and metals [99]. Various fiber structures, such as hollow fibers, helical fibers, core-shell fibers, porous fibers, etc., can be generated utilizing the electrospinning technique and specialized equipment. In addition, the method is capable of manufacturing a variety of single-fiber structures consisting of organized fiber configurations. Depending on their physical, biological, or chemical properties, electrospun fibers are very attractive for a variety of applications, such as sensors, biomedicine, filtration, etc. [100]. Since the late 1990s, not only the electrospinning process has been carefully revaluated in laboratories to assure its acceptability at the mega scale, but it has also been widely implemented in industry [101], [102].

3.2 Electrospinning setup, procedure and parameters

A standard electrospinning setup consists mainly of a high-voltage power source, a needle spinneret and a grounded conductive collector, as shown in **Figure 6**. There are no special laboratory requirements, and the area needed to put up lab-scale electrospinning devices is on the order of one square meter. Considering these, it has not been unexpected the implementation of electrospinning apparatus in a large number of laboratories around the world during the past few decades. However, it is essential to recognize that electrospinning is not a simple technology, easy to comprehend in its nature and to control in its performance. It is, in fact, a tremendously sophisticated approach at its core, both in terms of theoretical comprehension and experimental manipulation. In addition, electrospinning has advanced significantly in basic research and applications over the past few decades, making it increasingly challenging to develop innovative methodologies, concepts, and applications, as well as building more advanced electrospinning setups able to give precise control over a wide range of electrospinning parameters.
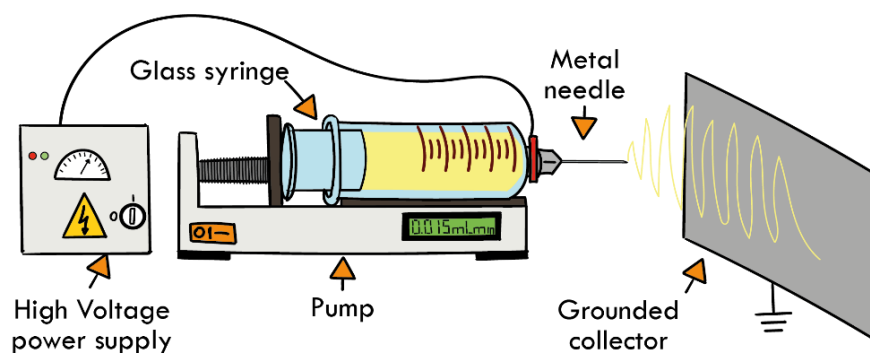
Figure 6 – Electrospinning setup.

Typically, the spinning solution, located inside the syringe, is moved by a pump that discharges a specified volume per unit time. The high voltage is applied to the metal needle, that generally acts as one of the electrodes, and the counter electrode, which is usually represented by a grounded conductive collector. Under these conditions the electrospinning process takes place. The strong electrostatic force has been recognized to be the driving power behind

the electrospinning process. Indeed, under the influence of a strong electrostatic field, the charged solution jet at the tip of the spinneret adjusts its size to maintain force equilibrium and, as the strength of the electrostatic field increases, the surface induction charges reject one another and generate shear stresses. These repulsive forces work in the opposite direction of the surface tension, causing the solution drop to extend into a Taylor cone and contributing to the initiation of the surface. When the electrostatic field reaches the critical voltage V_c, the equilibrium of repulsive forces is disturbed, resulting in the ejection of a charged jet from the tip of the conical drop. Based on Taylor's calculation [103], the critical voltage V_c for electrospinning is (Equation 7):

$$V_c^2 = 4\frac{H^2}{h^2}\left[ln\left(\frac{2h}{R}\right) - 1.5\right](1.3\pi R\gamma)(0.09) \ (7)$$

where H represents the distance from the spinneret tip to the collector, h is the length of the liquid column, R represents the inner radius of the spinneret, and g is the surface tension of the spinning solution (H, h, and R are measured in cm whereas g is measured in dyn/cm). To predict the voltage, the value 0.09 is inserted. After fiber elongation and solvent evaporation, solid ultrathin fibers are eventually deposited onto the collector. In the end, a thin, fibrous nonwoven film is made by constantly collect fibers onto the collector.

Multiple parameters can influence the electrospinning technique and are generally categorized into three groups: solution parameters, process parameters, and ambient conditions, such as temperature and humidity. Solution parameters include molecular weight, conductivity, viscosity, and surface tension. Process parameters include applied electric field, distance from tip to collector, and feeding or flow rate. Each of these parameters has a substantial effect on the fiber morphology resulting from electrospinning, and by manipulating them appropriately, it is possible to produce nanofibers with the desired morphologies and diameters.

3.2.1 Applied Voltage

In the electrospinning process, the applied voltage is a very important parameter. After reaching the threshold voltage, that induces the required charge in the solution along with the electric field, fiber creation occurs. By increasing the applied voltage and fixing the flow rate of the solution, the Taylor cone that forms at the end of the needle becomes smaller, less stable [104], and may eventually recede within the needle [105]. There are different opinions about the effects of applied voltage on the morphology of nanofibers. Researchers have shown that higher voltages result in a higher polymer ejection, which facilitates the creation of fibers with a larger diameter [106], [107]. Other authors have observed that an increase in the applied voltage increases the electrostatic repulsive force on the fluid jet, which eventually favors the reduction in fibers diameter. In the case of a low-viscosity solution, for instance, a higher voltage induces greater stretching of the solution due to the increased columbic forces in the jet and a stronger electric field; these effects result in a reduction of fibers diameter and quicker evaporation of solvent from fibers. However, there have been reports of an exception to this theory, and it is hypothesized that at a lower voltage close to the critical voltage, the flight time is increased, giving the solution more time to be stretched prior to the deposition [108]. According to a study by Wu et al. [109], fibers diameters decreased with increasing voltage to a minimum before the trend reversed with further voltage increases. Other investigations have demonstrated that the diameter of the fiber may initially increase with an increase in voltage, but above a certain voltage, the diameter begins to decrease [110]. While higher voltage may increase the stretching of the solution droplet, it may also accelerate the droplet toward the collector due to the increased potential difference, resulting in a less flight time for the jet to stretch prior to the deposition. This leads to an increase in fibers diameter. In addition, increasing the applied voltage, there is a greater probability of beads formation [111], [112].

3.2.2 Flow Rate

The rate at which the polymer is ejected from the syringe is an essential process parameter because it influences the velocity of the jet and the transport of the material. The morphology of electrospun nanofibers (NFs) is controlled by the polymer solution that flows through the metallic needle's tip. By determining the optimal critical flow rate for a polymer solution, uniform beadless electrospun NFs can be produced. The threshold value for each polymer system varies. A lower flow rate is preferred since the solvent will have sufficient time to evaporate [113] and more time will be available for polymerization, producing smooth fibers with a small diameter. In the case of polystyrene fibers, it has been found that the fiber diameter and pore diameter increase as the polymer flow rate increases, and that the morphological structure can be altered slightly by varying the flow rate. Systematically, Megelski et al. [111] and Zong et al. [104] investigated the effect of solution flow rate on fibers shape and size. When the solution flow rate is excessively high, periodic solution dripping and beaded fibers are observed. Several studies have reported the production of ribbon [114] fibers as the flow rate increases, and further increases may lead to the formation of droplets and wet fibers. This is a result of the increased volume and initial radius of the electrospinning jet, which reduces bending instability and thus causes fibers diameter to increase. However, when the flow rate is insufficient to satisfy the fiber drawing rate, the spinning process is interrupted and the formation and disappearance of the Taylor cone within the nozzle leads to a greater divergence in fibers diameter [115].

3.2.3 Collectors

The various types of collectors have a considerable effect on the nanofibers production and arrangement, as well as the structure of the collected film [116]. The collector can affect fibers productivity by affecting the ability of charges on deposited fibers to be carried to ground, hence affecting the number of

fibers collected on the substrate. A collector serves as a conductive substrate for collecting nanofibers. It has been demonstrated that even slight alterations in the electric field profile on the collector surface can affect fibers deposition [117]. Despite variations in the effect of charge retention due to collector material, its impact on the diameter of electrospun fibers appears to be minor. Aluminium foil is frequently utilized as a collector. Adomaviciute and Stanys [118] investigated the effects of different support materials (polypropylene, polyethylene, polyethylene terephthalate, aluminium, acetate fiber, and paper) and grounding electrodes (cylindrical, wire, or support material 40 mm from the wire electrode) located behind the support material on the collection of polyvinyl alcohol via free surface electrospinning. It was discovered that the type of grounding electrode influences the quantity of fibers gathered, more than the support material, with the cylindrical electrode collecting most fibers. This is likely owing to the greater potential difference between the solution surface and the larger surface area of the cylindrical grounding electrode. The electrospinning technique typically produces a layer of nanofibers on any collector, and the nanofiber collection is typically a nonwoven mesh on a flat plate. Controlled fiber structures have many applications in different fields. For instance, it has been shown that cells cultured on aligned nanofiber scaffolds proliferate in the direction of the fiber orientation [119]. In order to produce these kinds of fibers, other collectors, such as conductive cloth, conductive paper, wire mesh [120], pin [121], parallel or gridded bar [122], rotating rod, rotating wheel [119] and liquid non-solvent [123], among others, are commonly employed.

3.2.4 Distance Needle Tip to Collector

Due to its dependence on deposition time, evaporation rate, and whipping or instability interval, the nanofiber morphology can be easily altered by the distance between the metallic needle tip and the collector [124]. Therefore, a certain distance must be maintained to produce homogeneous and smooth electrospun nanofibers, and any deviations of the critical distance will affect the

nanofibers' morphology [102]. Several researchers have examined the effect of the distance between the needle tip and the collector concluding that defective nanofibers with a large diameter are produced when this distance is kept small, whereas the nanofiber diameter and electrical density decrease as it is increased [125]. A large distance may not be suitable for solvents with fast evaporation, but a minimum distance is required for the formation of fibers. There are examples in which a change in the distance between the metallic needle and the collector has no influence on the nanofibers' morphology [106].

3.2.5 Solvent type

The solvent selection represents one of the most important aspects in the development of smooth and bead-free electrospun nanofibers. Typically, two considerations must be made before choosing the solvent. First, the preferred solvents for the electrospinning process must completely solubilized polymers. Second, the boiling point of the solvent, that indicates its volatility, should be from low to medium. In general, volatile solvents are preferred because their high evaporation rates facilitate the evaporation of the solvent from the nanofibers as they flight from the needle tip to the collector. However, highly volatile solvents are typically avoided due to their low boiling temperatures and fast evaporation rates, which result in jet drying at the needle tip with its consequent obstruction. Additionally, fewer volatile solvents are avoided because their high boiling temperatures prevent them from drying throughout the flight of the nanofiber jet. On the collector, the deposition of solvent-containing nanofibers will result in the development of beaded nanofibers [126], [127]. In addition, the solvent is crucial to the manufacturing of highly porous nanofibers. When a polymer is dissolved in two solvents, one of them may behave as a non-solvent. The different evaporation rates of the solvent and non-solvent will cause phase separation, resulting in the production of extremely porous electrospun nanofibers. By changing the ratio of tetrahydrofuran (THF) to dimethylformamide (DMF), Megelski et al. [111] produced nanofibers with a porous structure. In addition to the solvent's volatile character, its conductivity and dipole moment are also crucial.

Methods for production and characterization
of active layers for sensor device

Jarusuwannapoom et al. [128] tested 18 solvents to see how they affected conductivity and dipole-moment. They found that only ethyl acetate, DMF, THF, methyl ethyl ketone, and 1,2-dichloroethane could be used for the electrospinning of polystyrene polymeric solutions, because these solvents had better conductivity and dipole-moment values. In **Table 3** the main properties of most common solvent are reported.

Table 3 - Properties of several solvents used in the electrospinning process [102].

Solvents	Surface tension (mN/m)	Dielectric constant	Boiling point (°C)	Density (g/mL)
Chloroform	26.5	4.8	61.6	1.498
Dimethyl formamide	37.1	38.3	153.0	0.994
Hexafluoro isopropanol	16.1	16.7	58.2	1.596
Tetrahydrofuran	26.4	7.5	66.0	0.866
Trifluoro ethanol	21.1	27.0	78.0	1.393
Acetone	25.20	21.0	56.1	0.786
Water	72.8	80.0	100	1.000
Methanol	22.3	33.0	64.5	0.791
Acetic acid	26.9	6.2	118.1	1.049
Formic acid	37.0	58.0	100.0	1.21
Dichloro methane	27.2	9.1	40.0	1.326
Ethanol	21.9	24.0	78.3	0.789
Tri fluoro acetic acid	13.5	8.4	72.4	1.525

3.2.6 Polymer concentration and solution viscosity

During the spinning of polymeric fibers, the viscosity of the solution plays a critical role in determining fibers size and morphology. The viscosity of polymers, their concentration and molecular weights are all correlated. The relationship between electrospun fibers and polymer viscosity and

concentration has been studied in a variety of cases, including polyethylene oxide [129], polyvinyl alcohol [130], polymethyl methacrylate [131] and polystyrene [128]. Considering that the electrospinning process depends on the uniaxial stretching of a charged jet, the concentration of the polymeric solution has a substantial effect on this. Low polymer concentration results in electrospraying rather than electrospinning because the solution's low viscosity and high surface tension cause the entangled polymer chains to fragment before reaching the collector [132]. At a slightly higher concentration, both beads and fibers are found to develop. In general, fibers with a smooth surface are produced by electrospinning at a suitably high concentration. Eventually, fibers diameter will increase as the solution concentration increases. In addition, increasing the concentration beyond a critical value (the concentration at which beadless uniform nanofibers are formed) impedes the flow of the solution through the needle tip (the polymer solution dries at the tip of the metallic needle and obstructs it), resulting in nanofibers with defects or beads. Therefore, in order to produce nanofibers without beads, it is also necessary to determine the critical ratio between concentration and viscosity.

3.2.7 Molecular weight

Molecular weight is another crucial solution parameter that influences the structure of electrospun fibers. The molecular weight of a polymer represents the number of entangled polymer chains in a solution and, consequently, the viscosity of the solution. Polymer solutions with a high molecular weight are usually used for electrospinning because they have the right viscosity to make fibers. Filip et al. [133] have studied the relationship between the diameter of electrospun polyvinyl butyral (PVB) fibres and their molecular weight and polymer concentration. This study demonstrated that the solution containing PVB with the highest molecular weight and a fixed polymer concentration produced fibers with a major mean diameter. Lee et al. [134] have demonstrated how the molecular weight of atactic polyinyl alcohol (A-PVA) impacts the structure of nanofibers produced by electrospinning. The average diameter of A-PVA nanofibers decreased slightly as the molecular weight increased. In

terms of crystalline characteristics, thermal stability, and mechanical qualities, an A-PVA nanofabric with a larger molecular weight outperformed one with a lower one.

3.2.8 Solution Conductivity

The conductivity of a solution is primarily determined by the type of polymer, the solvent, and the salt. The conductivity of the solution influences the formation of the Taylor cone and contributes to the regulation of the nanofiber diameter. Angammana et al. [135] analyzed the role of solution conductivity in polyethylene oxide fiber synthesis. The results of this study demonstrate that the average jet current initially increases as the conductivity of the solution increases and then decreases modestly. In contrast, the average fibers diameter decreases as the conductivity of the solution increases. These phenomena can be completely explained by the distribution of the surface charge around the electrospun jet and the variation of the tangential electric field along the fluid's surface. Very low-conductivity polymer solutions cannot be electrospun because there is no surface charge at the fluid droplet's surface to form a Taylor cone. Likewise, solutions with extremely high conductivity will not form a Taylor cone due to the depleted tangential electric field along the fluid droplet's surface. When the conductivity of the polymer solution is increased, additional phenomena can be observed, including the generation of multi-jets at fluid droplets and fibers protrusions.

3.2.9 Surface tension

Surface tension, which is more likely a result of the solvent compositions of the solution, plays an important role in the electrospinning process, and fibers can be produced without beads by decreasing the surface tension of the solution. Solvents may affect surface tension differently. In general, the high surface tension of a solution limits the electrospinning process due to the jet instability and the formation of sprayed droplets [136]. The creation of

droplets, beads and fibers is dependent on the solution's surface tension and a lower surface tension of the spinning solution facilitates electrospinning with a lower electric field [137]. However, a solvent with a lower surface tension is not necessarily more suitable for electrospinning. If all other parameters remain constant [106], [138], surface tension determines the upper and lower boundaries of the electrospinning window.

3.2.10 Relative Humidity and Temperature

The diameter and morphology of nanofibers are influenced by environmental variables such as relative humidity and temperature. Both a higher and lower relative humidity results in increased fibers diameter. For high humidity [139], this is due to the rapid precipitation of the polymer when water condenses on the surface of the electrospinning jet, preventing further elongation of the polymer and resulting in thicker fibers. For low humidity, the fast solvent vaporization, with the resulting increase in solidification rate, increases fibers diameter. Sometimes the rate of evaporation is faster than the speed at which the solvent is removed from the needle's tip, and this would be a problem for electrospinning. Therefore, electrospinning can only be performed for few minutes before the needle tip becomes clogged [140]. Casper et al. [141] have investigated the effect of humidity variation when polystyrene solutions are spun. They discovered that when humidity increases, little circular pores appear on the surface of the fibers, and as humidity increases more, these pores merge. When the temperature increases, the rate of solvent evaporation increases and the viscosity of the solution decreases. This causes the average fibers diameter to decrease [142].

3.3 Characterization of active layer

Several techniques are frequently applied to characterize materials. The most common are scanning electron microscopy (SEM), X-ray diffraction (XRD), micro-Raman spectroscopy (MRS) and thermogravimetry (TGA), that allows the extrapolation of diverse and complementary information regarding sample morphology, crystalline structure, and thermal stability.

Methods for production and characterization
of active layers for sensor device

Scanning Electron Microscopy (SEM)

The scanning electron microscope provides information regarding the topography, morphology, composition, and crystallography of samples. Numerous applications are associated with this technology for micro and nanostructured investigation. A scanning electron microscope consists of an electron optical column in which an electron beam is generated by a suitable source, often a tungsten filament, and accelerated by a high voltage between 20 and 60 kV. Using appropriate lenses, the electron beam is concentrated onto a spot on the surface of the sample. This beam is raster-scanned over the specimen, and the intensities of various signals formed by interactions between the beam electrons and the specimen are detected and represented as variations in brightness on the image display. These signals, which include backscattered electrons, secondary electrons, X-rays, and Auger electrons, are illustrated in **Figure 7**. The penetration of electrons to varying depths produces distinct signals, and consequently, each interaction can reveal information regarding the material's composition, surface topography, and morphology [143]. Conventionally, SEM operates under high vacuum conditions using conductive samples. Eventually, non-conductive samples are coated with a thin layer of heavy metal or carbon to prevent the accumulation of electron charges on the specimen surface, that in turn causes distortion. In low voltage SEM, LV-SEM, residual gas in the specimen chamber is ionized to form a cloud of positive charge around the sample, which dissipates the electron beam energy without the need to coat the sample physically. Image formation in the LV-SEM is typically the result of backscattered electrons, which are generated more strongly from high atomic number material. As a result, areas of the sample with a high atomic number appear brighter than areas with a lower atomic number. Energy-dispersive X-ray spectroscopy (EDX), an analytical technique used for elemental analysis or chemical characterisation of a sample, is typically coupled with scanning electron microscopy (SEM). It depends on the observation of the interaction between X-rays and the specimen. The fundamental principle that each element has a unique atomic structure, hence

permitting a unique collection of peaks in its X-ray spectrum, is largely responsible for its characterisation capabilities.
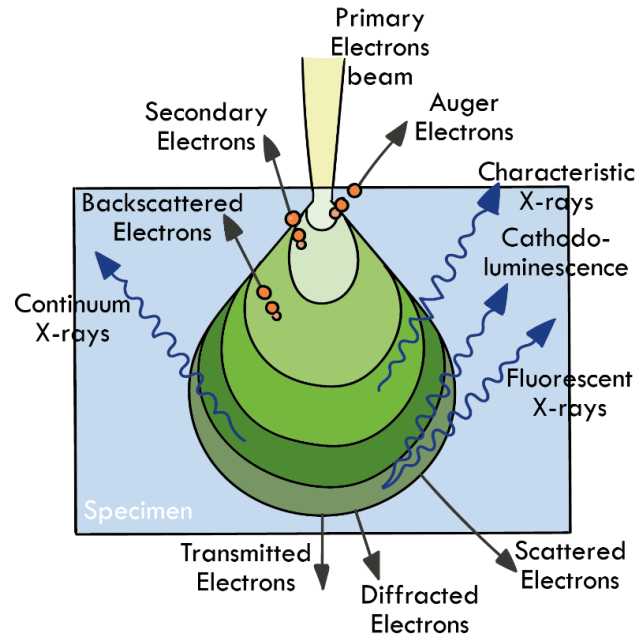
Figure 7 - Schematic diagram of the interaction of radiation-matter: Auger electrons, secondary electrons, backscattered electrons, and X-rays.

The incident beam may excite an electron in an inner shell, causing it to be ejected from the shell while simultaneously producing an electron hole. The hole is subsequently filled by an electron from a higher-energy outer shell, and the energy difference between the higher-energy shell and the lower-energy shell may be emitted as characteristic X emission. An energy-dispersive spectrometer can measure both the number and energy of the X-rays emitted by a specimen. Since the X-ray energy depends on the energy difference between the two shells and the atomic structure of the emitting element, it is feasible to determine the elemental composition of the sample.

A Phenom Pro-X scanning electron microscope equipped with an energy-dispersive X-ray spectrometer was utilized for the preliminary characterization of electrospun materials. A detailed investigation was performed through a high-resolution scanning electron microscope, Jeol JSM-7900F, specialized in low accelerating voltages studies and low vacuum measurements. The system was coupled with a chemical microanalysis system using X-ray spectrometry (BRUKER Esprit).

Methods for production and characterization
of active layers for sensor device

X-ray diffraction (XRD)

X-ray diffraction is an analytical technique that is mostly employed to collect data on crystalline substances [144]. Variations in crystal structure, phase quantification and identification, shape and size of crystallite, distortion of lattice and its size are examples of this type of data. It is based on the interaction between X-rays and matter, as described by Bragg's Law:

$$2d \sin \theta = n\lambda \quad (8)$$

where d is the distance between crystal plane layers, q represents the incident angle, n is an integer (the diffraction order), and λ represents the incident wavelength (**Figure 8**). When the path difference equals any integer multiple of the wavelength, constructive interference will occur. Common X-ray sources are tubes in which a tungsten filament is brought to a negative potential of 30-60 kV and produces electrons, that are directed by the electric field to a target of pure metal (Cu, Cr, Fe, Co, etc.). Copper is the most encountered target material, with K(Cu) = 1.5418 Å.
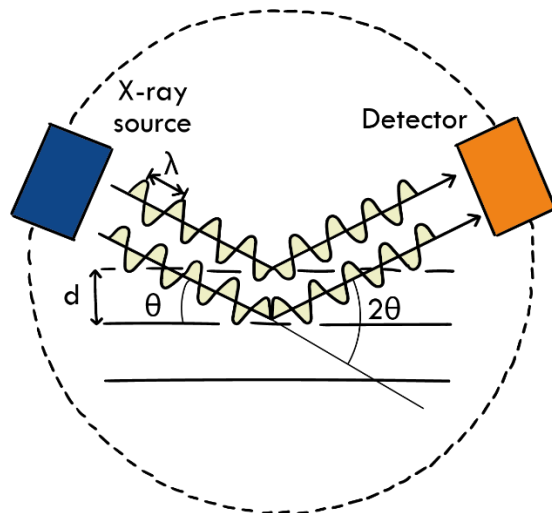
Figure 8- Instrumental sketch and geometry for interference of a wave scattered from two planes separated by d spacing.

By scanning the sample through a range of 2θ angles, it is possible to acquire all potential diffraction directions of the lattice. The result is displayed as a

diffractogram in which the diffraction intensity is plotted against the 2θ angle. Peaks can be allocated unambiguously, enabling material identification.

To this purpose a Bruker D2 Phaser with CuKα radiation at 30 kV and 20 mA was used. Peaks attribution was made according with COD (Crystallographic Open Database). The diffraction angles 2θ were varied between 10° and 80° in steps of 0.02° and a count time of 5 s per step.

Thermogravimetry (TGA)

Thermogravimetry (TGA) and coupled differential scanning calorimetry (DSC) are two characterization techniques that can be used to examine the changes that occur in a sample when the temperature varies. Specifically, thermogravimetry is a technique that allows one to study the change in weight of a given sample when it is heated by a controlled temperature rise. During the thermogravimetric analysis of samples, heating triggers chemical reactions that typically result in the creation of volatile compounds by the splitting of bonds. Consequently, TGA is mostly utilized to comprehend thermal processes such as absorption, adsorption, desorption, vaporization, sublimation, breakdown, oxidation, and reduction [145]. In addition, the capacity to anticipate the thermal stability of samples permits the investigation of the kinetics of chemical reactions under varying conditions. In fact, TGA is used to measure a substance's thermal stability based on its ability to retain its properties essentially unaltered despite exposure to heat. Upon increasing the temperature of a sample, the sample will certainly lose weight. The information concerning weight loss is necessary to establish the composition of a sample in order to comprehend the reaction stages involved in the decomposition procedure. Through the weight loss profile, it is also feasible to identify the unknown compound contained in the sample or to determine the amount or percentage of a specific compound present in the sample's mixture of various compounds. The result of this analysis is represented by a thermal decomposition curve, which indicates the temperature or time on the abscissa and the absolute value or percentage change in mass on the ordinate.

Methods for production and characterization
of active layers for sensor device

Differential scanning calorimetry is an analysis that offers quantitative information on the energy exchanges occurring within a sample, specifically the difference in thermal flux between the examined sample and a standard sample. The heat flux between the sample and the reference sample is proportional to the temperature difference between them, which is caused by processes occurring within the sample.

Instrumentation consists mostly of a microbalance put inside a furnace with precise temperature control (**Figure 9**). The system as a whole is operated by a computer that regulates the weight and heating or cooling of the sample at the same time, logging the sample's mass and temperature measurements over time. A gas system device also permits the regulation of the surrounding atmosphere's pressure and composition.

Thermogravimetric TGA/DSC analysis was performed with a Netzsch instrument. The temperature-programmed experiments were carried out in the range 25-1000°C, under a total air flow rate of 100 cc/min with a heating rate of 5°C min^{-1}.
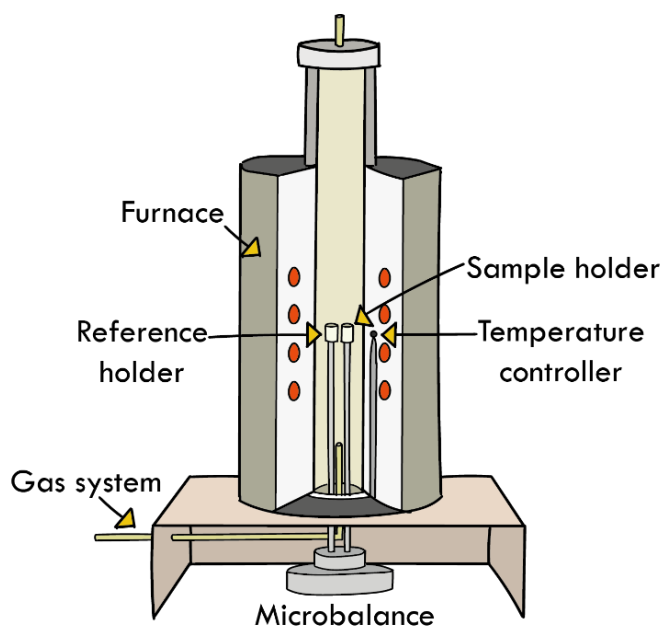
Figure 9 - Schematic representation of TGA-DSC instrument.

Micro-Raman Spectroscopy

Micro-Raman Spectroscopy is an analytical technique that can provide information regarding the sample's molecular composition, bonds, chemical environment, phase, and crystalline structure. In a Raman scattering experiment, the sample is investigated by a laser-emitted monochromatic electromagnetic radiation. The interaction between the electromagnetic radiation and the electrons of molecules produces an oscillating electric dipole. This dipole is responsible for the dispersion of the incident radiation. The diffuse radiation consists of energy-variable components. The Rayleigh component, which accounts for most of the dispersed radiation, is produced by an elastic diffusion process that does not require energy exchange with the system and has the same energy as the incident radiation. Inelastic diffusion processes generate the Stokes components with lower energies and the anti-Stokes components with greater energies than the incident radiation. **Figure 10** depicts a schematic of the diffuse radiation's constituents.
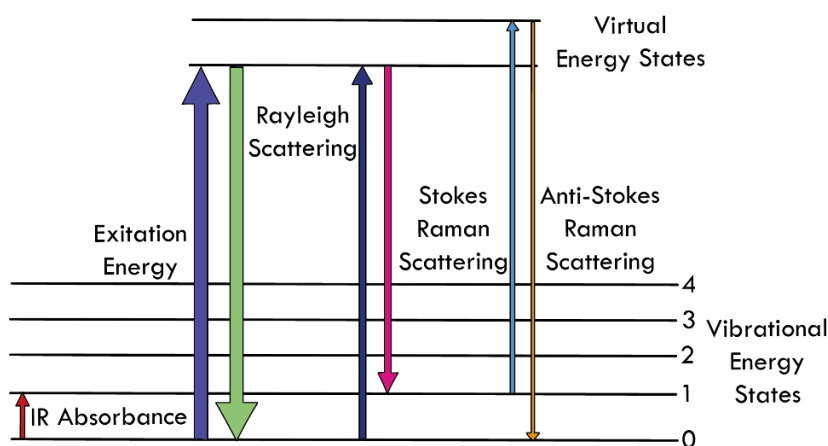
Figure 10 - Energy levels of a molecule and Raman effect.

The information that a Raman spectrum may provide is nearly entirely dependent on the Stokes lines. Rayleigh radiation provides little information because it is identical in every sample, and anti-Stokes lines are typically too weak to be discerned. Since the Stokes lines are related to the functional groups and vibrational modes of the molecules in the sample, they are utilized for the qualitative identification of compounds present in the sample. In the Raman spectrum, the ordinate represents the intensity of light emission, while the

abscissa reports the absolute frequency in cm^{-1} or, more often, the Raman shift, which is the difference between the wave numbers of the measured radiation and the incident radiation.

4

Design and characterization of active layers for sensor device

The first paragraph of this chapter describes in detail production and characterization of active layers. The second section of this chapter is dedicated to the innovative production technique of the single fiber sensor.

4.1 Production of active layers by electrospinning

Materials

Poly(methyl methacrylate)(PMMA) (average Mw = 996,000), poly(vinyl acetate) (PVAc) (average Mw = 500,000), poly(styrene) (PS) (average Mw = 192,000), ethanol (96% purity), ethylenediaminetetraacetic acid disodium salt dihydrate (Na$_2$EDTA), dimethylformamide (DMF), trimethoxy(propyl)silane (97%) were used for the production of fibers.

Fibers fabrication

In order to produce the optimal active layer for heavy metal detection, several sensing materials were produced, using three different polymers, PMMA, PVAc and PS, with or without the addition of Na$_2$EDTA, in numerous experimental conditions. These three polymers were chosen for their hydrophobicity and cost-effectiveness. Typically, the polymer is dissolved in its solvent to produce the electrospinning solution, whereas, in the preparation of polymeric solutions with the addition of the disodium salt of EDTA (Na$_2$EDTA), a further step is required. First, the additive is dispersed in the solvent using an ultrasonic bath, the mixture is stirred for few minutes and finally the polymer is added. All the prepared solutions were stirred at room temperature, at different speed rate, depending on the solution type. Several tests, as detailed in **Table 4**, were carried out in order to optimize the parameters

related to the preparation of solutions to produce the active layer made of fibers.

Table 4 – List of realized solution, solvents and their parameters preparation.

Sample name	Solvent	Weight Ratio Polymer/Solvent	Weight Ratio Additive/Polymer	Speed and time stirring
PVAc	EtOH (96%)	12.3/87.7	-	500 rpm- 3h
PMMA	DMF	7.5/92.5	-	600 rpm - 4h
PS	DMF	21.9/78.1	-	600 rpm - 4h
PVAc-Na$_2$EDTA (1:0.1)	EtOH (96%)	12.3/87.7	9.1/90.9	500 rpm- 3h
PMMA-Na2EDTA (1:0.1)	DMF	7.5/92.5	9.1/90.9	600 rpm - 4h
PMMA-Na$_2$EDTA (1:0.25)	DMF	7.5/92.5	20.0/80.0	600 rpm - 4h
PMMA-Na$_2$EDTA (1:1)	DMF	7.5/92.5	50.0/50.0	600 rpm - 4h
PS-Na$_2$EDTA (1:0.1)	DMF	21.9/78.1	9.1/90.9	600 rpm - 4h
PS-Na$_2$EDTA (1:0.25)	DMF	21.9/78.1	20.0/80.0	600 rpm - 4h
PS-Na$_2$EDTA (1:1)	DMF	21.9/78.1	50.0/50.0	600 rpm - 4h

For the electrospinning process, polymeric solutions were loaded into a 10 mL glass syringe connected to a 0.7 mm metal needle. A pump (KDS 100 Legacy) was used to control the flow rate, while different applied voltage and

needle-to-collector distance (NCD) were tested. The electrospinning process was performed at 25 °C with a relative humidity of 30%. The **Table 5** provides a summary of the electrospinning parameters used for each sample.

Table 5 – Electrospinning parameters.

Code	Voltage (kV)	Flow rate (mL/h)	NCD (cm)
PtIDE-PVAc	13.0	0.800	13.0
PtIDE-PMMA	12.5	0.600	13.0
PtIDE-PS	12.5	0.900	15.0
PtIDE-PVAc-Na$_2$EDTA	11.5	0.800	13.0
PtIDE-PMMA-Na$_2$EDTA (1:0.1)	11.5	0.600	13.0
PtIDE-PMMA-Na$_2$EDTA (1:0.25)	11.5	0.600	13.0
PtIDE-PMMA-Na$_2$EDTA (1:1)	11.0	0.600	13.0
PtIDE-PS-Na$_2$EDTA (1:0.1)	11.5	0.900	15.0
PtIDE-PS-Na$_2$EDTA (1:0.25)	11.0	0.900	15.0
PtIDE-PS-Na$_2$EDTA (1:1)	10.5	0.900	15.0

Fibers were directly collected over the sensing substrate, fixed on aluminium foils and connected to the ground. In detail, two interdigitates (Pt-IDEs), the working electrode (WE) and the counter electrode (CE), made of platinum on a glass substrate from Metrohm DropSens (Herisau, Switzerland), were used for the realization of the sensing device, as shown in **Figure 11**. The dimensions of the glass substrate are 22.8 mm in length, 7.6 mm in width, and 0.7 mm in thickness. Each of the interdigitated electrodes has 125 digits with a bands/gaps equal to 5 microns, and each one is 6760 microns long. In order to increase the adhesion with the fibers, Pt-IDEs's surface was coated with a silane solution obtained by hydrolysing 2.33 g of trimethoxy(propyl)silane with 36.0 g of EtOH and 2.50 g of distilled water. The solution was stirred for 24 hours and finally spin-coated over supports. The thickness of the deposited layer is 200±20 microns.
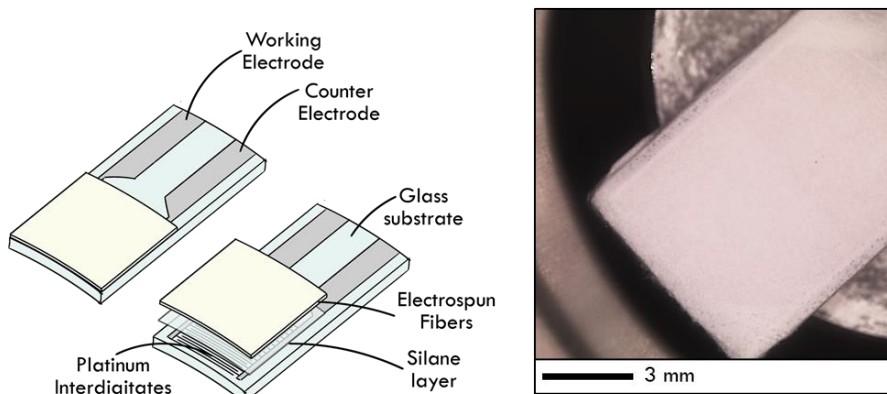
Figure 11 – Schematic representation of active layers electrospun over supports.

4.2 Results of Characterizations

In this paragraph, the results of the characterization of the fibers produced will be illustrated.

Scanning Electron Microscopy (SEM)

SEM images for the electrospun PVAc fibers are reported in **Figure 12**. The morphology results in ribbon/flat fibers, probably due to the use of a high volatile solvent, ethanol. The rapid vaporization of the solvent within the electrospinning jet leads to the formation of a skin layer, that collaps to form ribbons. However, the solvent volatility is not the only cause for the formation of ribbon-like fibers. Indeed, it is not just dependent on the polymer and solvent combination but also on the concentration of the solution. Koski et al [130] reported flat ribbon fibers when the concentration of polyvinyl alcohol (PVA) was high or eventually when higher molecular weights of PVA were used. On the contrary, both lower concentration and molecular weights produced circular cross-section fibers. As shown in the detailed picture, some beads are also detected, probably formed on a jet with skin, so that the skin covers both the jet and the beads. According to Koombhongse et al [146], when the solvent escapes from the interior and, as a consequence the jet collapses, the skin on the beads collapses too, forming a toroid with a membrane that covers the hole.
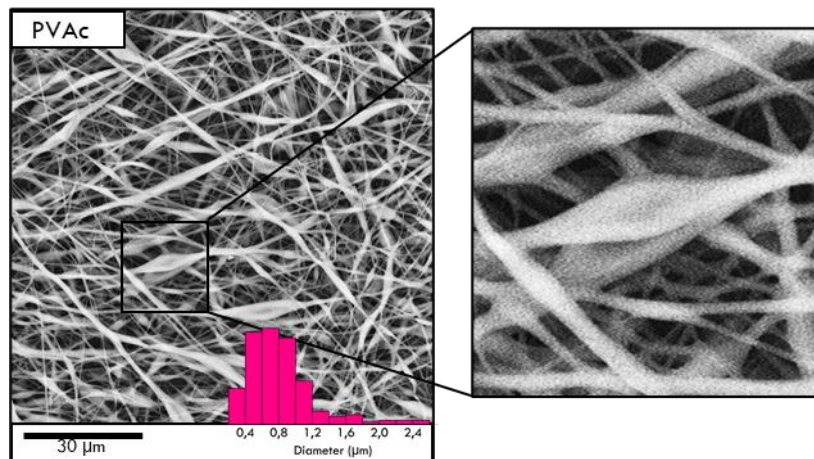
Figure 12 – SEM images of PVAc sample.
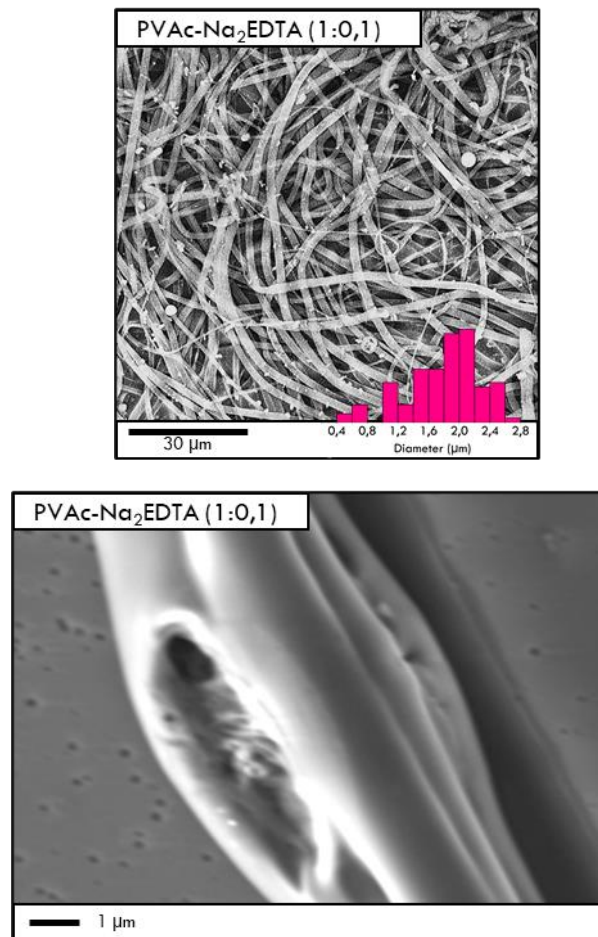
Figure 13 - SEM image of PVAc- Na₂EDTA (1:0,1) sample.

The addition of Na$_2$EDTA in the electrospun solution empathizes the formation of the flat ribbons morphology (**Figure 13**), and moreover, it promotes the enlargement of fibers, from around 0,8±0,2 μm to 2±0,2 μm.

The increase of the salt content further evidences the flat morphology, resulting in a poor encapsulation of Na$_2$EDTA particles. Therefore, high salt concentrations were not considered.

The morphology of electrospun polystyrene systems results in rounded type fibres with median dimension of 1,2 ±0,2 μm, as shown in **Figure 14**. The addition, and further increase of Na$_2$EDTA content, promotes the change of morphology from rounded to flat. The formation of ribbon cross-section fibers is due to the higher solution viscosity of systems added with salt. Furthermore, the increasing of Na$_2$EDTA amount in the electrospun solution causes a slight increase of fibers dimension, achieving, for the higher concentration of the salt, a value of 1,6±0,2 μm. In addition, for all the tested concentrations, Na$_2$EDTA particles resulted well encapsulated in the structure of fibers.
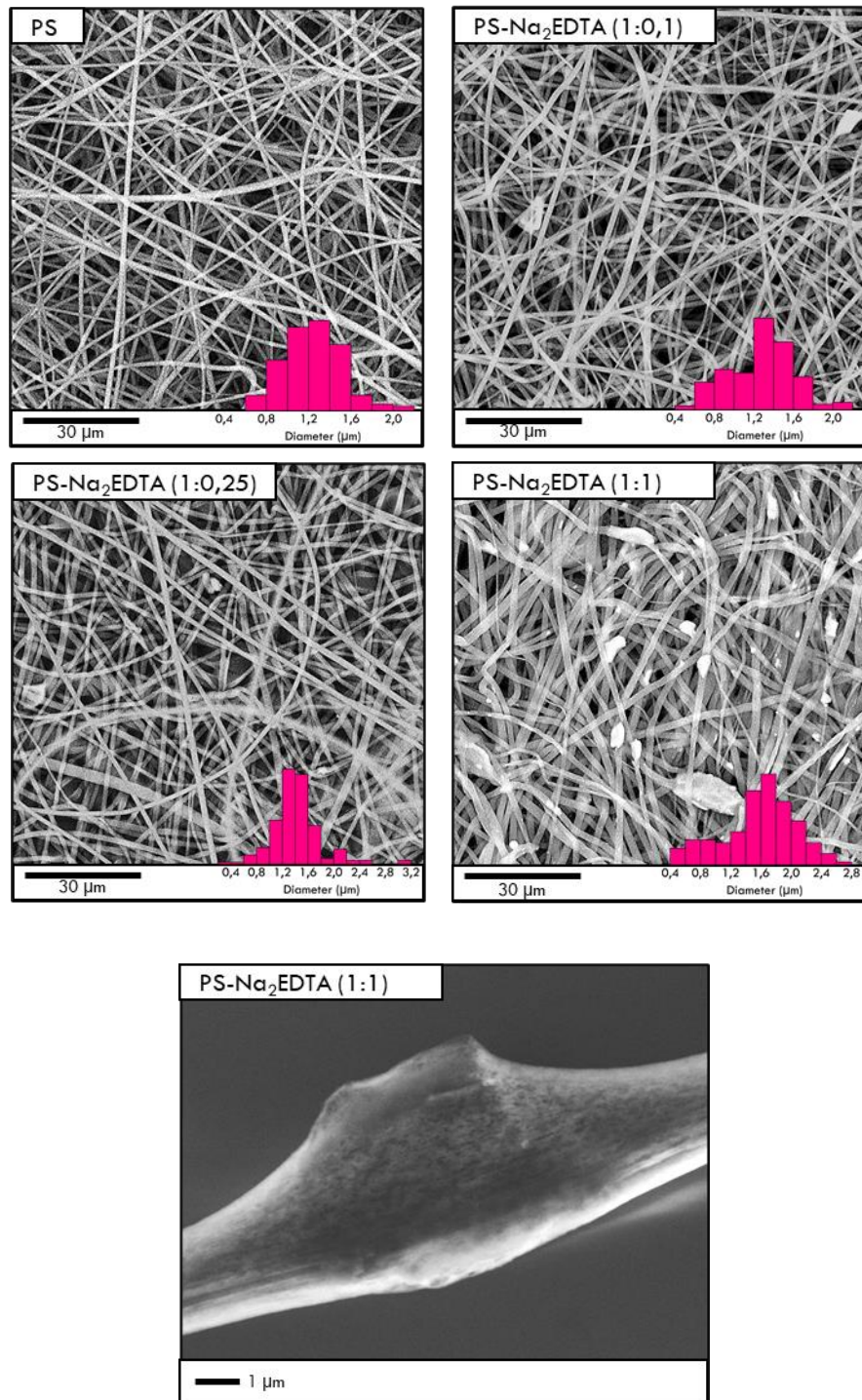
Figure 14 – SEM images of PS, PS- Na$_2$EDTA(1:0,1), PS- Na$_2$EDTA(1:0,25) and PS- Na$_2$EDTA(1:1) samples.

The morphology of electrospun PMMA systems results in rounded type fibres with median dimension of 0,9 ±0,2 μm, as shown in **Figure 15**. The addition of Na$_2$EDTA salt seems not to significantly affect the morphology

and the dimension of fibers. In this case the addition of the salt does not modify the viscosity of the electrospun solution. Na_2EDTA particles resulted intercalated between fibers segments but not completely encapsulated.
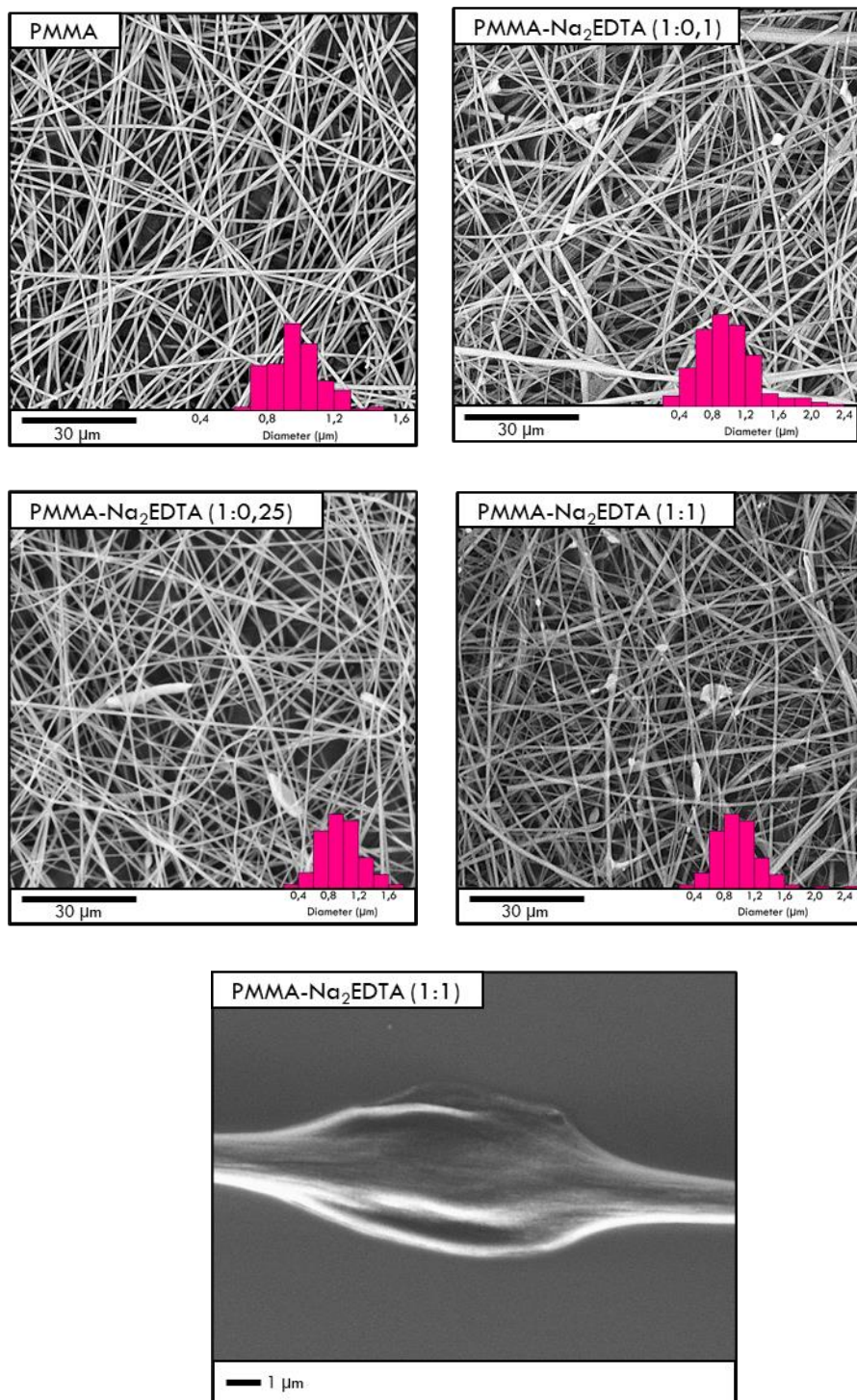
Figure 15 – SEM images of PMMA, PMMA-Na_2EDTA(1:0,1), PMMA-Na_2EDTA(1:0,25) and PMMA-Na_2EDTA(1:1) samples.

Moreover, it is interesting to highlight that PS-EDTA fibers are characterized by a porous structure with respect to PVAc-EDTA and PMMA-EDTA fibers, that indeed tended to swell in the first case and to be completely compact in the other case.

Micro-Raman

All recorder micro-Raman spectra showed the overlapping of the pristine polymers with the Na_2EDTA salt. Each spectrum is reported together with a schematic map where the salt dispersed over the single polymeric fiber is shown.

The Raman spectrum of polystyrene is much more complex because the molecule is less symmetric and has hydrogen atoms in addition to carbon atoms. There are also different bond types connecting the atoms. The masses of the atoms involved, and the strength of their bonds, affect the vibration's frequency. Low Raman shifts are found in heavy atoms and weak links. Strong bonds and light atoms have instead high Raman shifts.

The polystyrene spectrum exhibits high frequency carbon-hydrogen (C-H) vibrations at a wavelength of roughly 3000 cm^{-1}. Around 800 cm^{-1} is where the low frequency carbon-carbon (C-C) vibrations occur. Because hydrogen is lighter than carbon, the C-H vibrations have a greater frequency than the C-C vibrations. At about 1600 cm^{-1}, the vibration of two carbon atoms bound together by powerful double bonds (C=C) is observed. Compared to the two carbon atoms connected by a weaker single bond, this occurs more frequently (C-C, 800 cm^{-1}). Bond vibration rates are also influenced by the strength of the bond. As shown in the **Figure 16**, the C-H vibration of polystyrene can be seen in two bands at about 2900 and 3050 cm^{-1}. The carbons in the former case are part of a carbon chains (referred to as "aliphatic"), whilst in the latter case are part of a carbon ring (referred to as "aromatic").
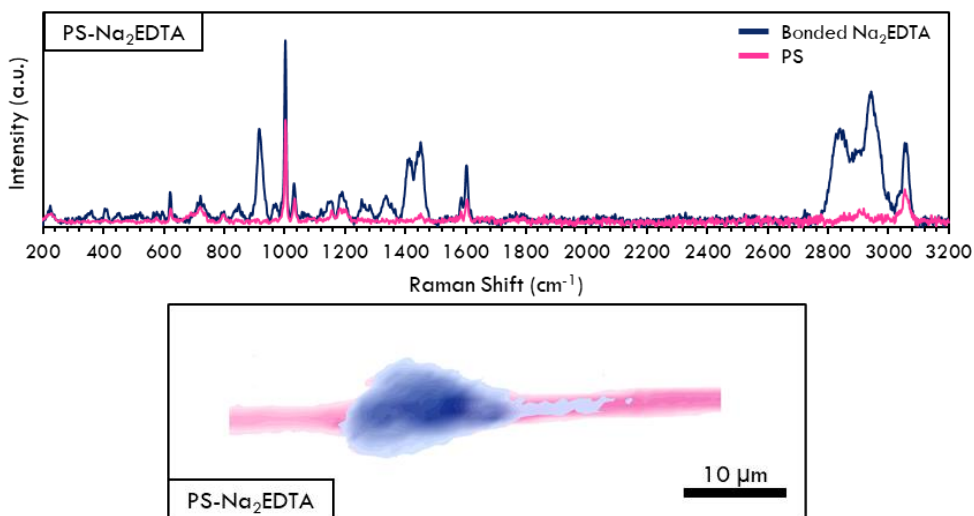
Figure 16 – Raman spectra of PS and PS-Na₂EDTA samples.

A complex molecule's vibration can be thought as being made up of numerous simple diatomic vibrations. However, it is only by taking into account the vibration of bigger groups of atoms that the entire complexity of the Raman spectrum can be fully appreciated (such as the aromatic carbon ring's expanding/constricting "breathing mode" that can be seen at 1000 cm^{-1} in polystyrene).

Raman spectrum of PMMA (**Figure 17**) showed the characteristic band of PMMA at 2952 cm^{-1}. This band indicates C–H stretching and is the most prominent in the PMMA structure. The bands at 1645 cm^{-1} can be attributed to the combination band arising from ν(C-C) and ν(C–COO). The other Raman bands, such as those appearing at 604, 833, 995, 1264, 1470,1739, and 3001 cm^{-1}, were in conformity with literature data [147].
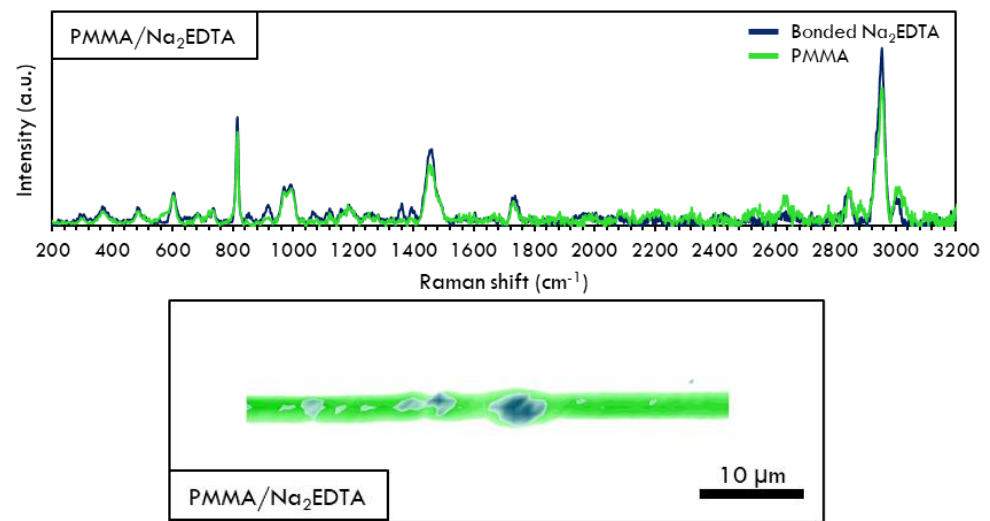
Figure 17 - Raman spectra of PMMA and PMMA-Na$_2$EDTA samples.

For the PVAc system the bands at 646, 921, 1428, 2112 and 2913 cm^{-1} were seen with large-intensity changes for each irradiation and they correspond to the modes of wagging of OH group (γw(OH)), stretching of C–C (ν(C–C)), bending of CH$_2$ and OH (δ(CH$_2$), δ(OH)), no assignment, stretching of CH of CH$_2$ group (ν(CH)), respectively (**Figure 18**).
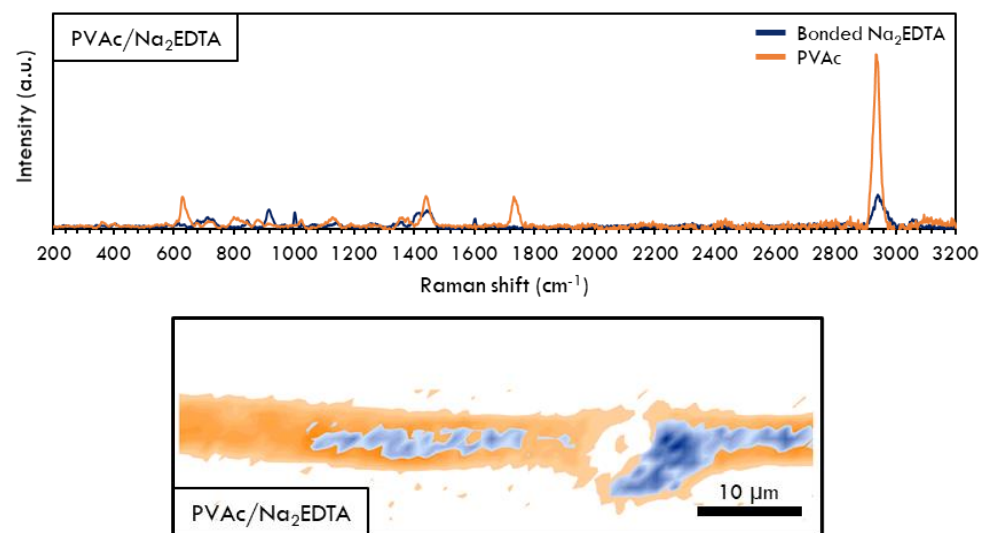
Figure 18 - Raman spectra of PVAc and PVAc-Na$_2$EDTA samples.

Disodium ethylenediaminetetraacetate (Na$_2$EDTA) is a chelating agent containing carboxyl and amino groups, with a wide range of coordination properties. Through the Raman spectrum several infrared coherent bands can

71

be distinguished. In the region from 2884 to 3021 cm^{-1}, the ν(C–H) stretches of the aliphatic CH$_2$ groups are detected. The small band at 3389 cm^{-1} corresponds to the deformation ν(O–H) of the waters of hydration and another, at 1608 cm^{-1}, is caused by the angular deformation δ(H–O–H). It is worth mentioning that the bands of water are always of very low intensity, since this solvent is an extremely weak Raman spreader.

Thermogravimetry Analysis

The thermal behaviour of disodium salt of EDTA was studied by means of thermogravimetric and differential scanning calorimetry analyses. The data collected, as shown in **Figure 19**, indicate that the first mass loss, around 4.5%, relates to the dehydration of the salt at 164 °C, whereas the melting point is at 266 °C. At 1000 °C, the residual mass is equal to 24.4%. Thermogravimetric curves of neat polystyrene fibers are displayed in **Figure 19**, thermal decomposition of the sample takes place in a programmed temperature range of 380-420°C. The onset temperature of polystyrene is 354° C, with 99.69% of final weight loss.
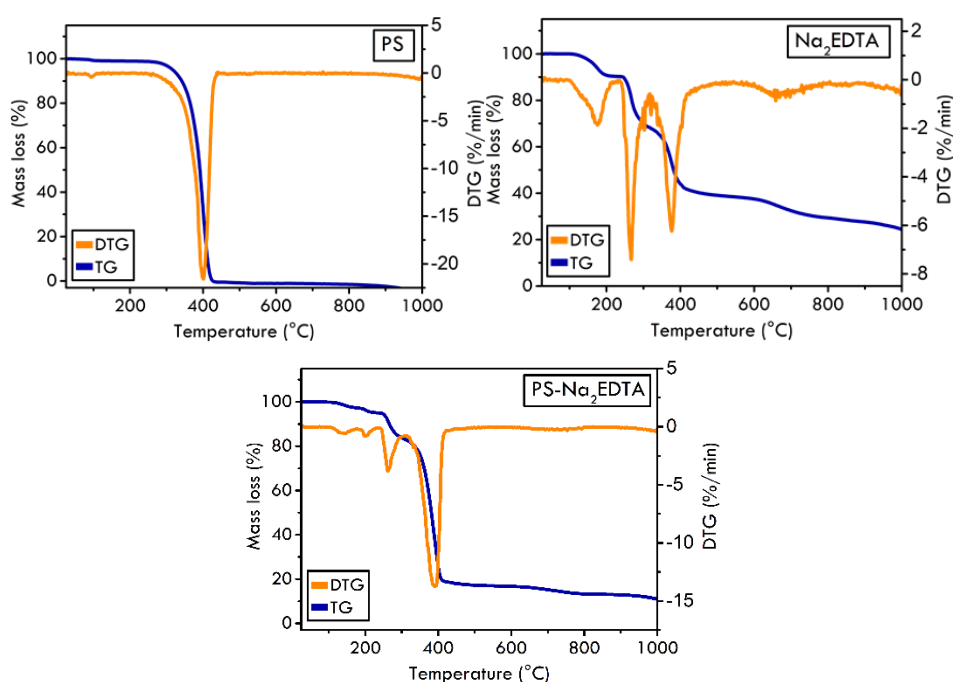
Figure 19 – TGA-DTG curves of PS, Na$_2$EDTA and PS-Na$_2$EDTA samples.

The addition of Na₂EDTA does not improve the thermal stability of polystyrene since the weight loss starts earlier with respect to the fibres without salt. Likely, this is due to the presence of the salt that is not chemically bonded to the polystyrene fibres but encapsulated inside the polystyrene fibers. The final residual mass, around 12% of the initial mass of the system polystyrene/Na₂EDTA, corresponds to the proportions of the salt used for the preparation of the polymeric solution. Thermogravimetric curves of neat PMMA are given in **Figure 20**. Two stages in the PMMA decomposition are evident. The first is near 200°C and the second is extended from 200°C to 400°C. The addition of Na₂EDTA affects the thermal profile of neat PMMA. As visible in **Figure 20**, there are three main stages of PMMA/Na₂EDTA degradation.
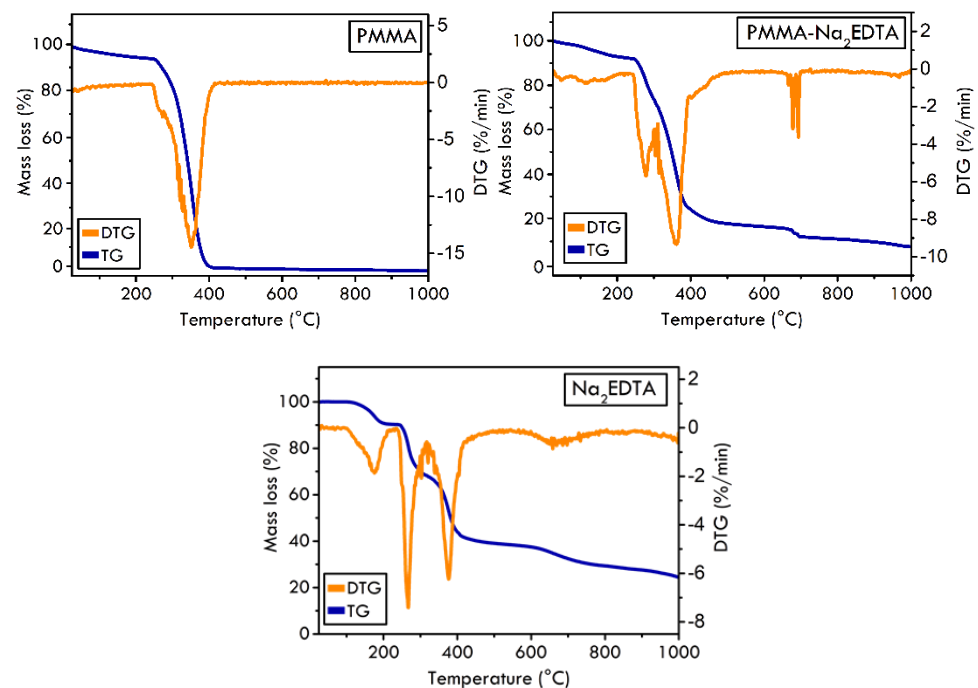
Figure 20 - TGA-DTG curves of PMMA, Na₂EDTA and PMMA-Na₂EDTA samples.

These stages are not completely separated (the first and the second stages partially overlap). The complexity of these stages may be a result of the overlapping decomposition of PMMA and Na₂EDTA salt. The third stage is attributable to decomposition of the amount of salt that resulted not totally entrapped into the fibres.

X-Ray Diffraction

X-ray diffraction studies can reveal much information about solid materials and is the most common method to determine the crystallinity of a polymer. However, polymers used in this study are totally amorphous, showing no long-range inter-molecular order and exhibiting a continuous pattern without diffraction peaks. The addition of Na₂EDTA allows the recording of diffraction peaks due to the crystallinity of the salt. The recorded XRD spectra for PS and PMMA based samples are reported in **Figure 21**.
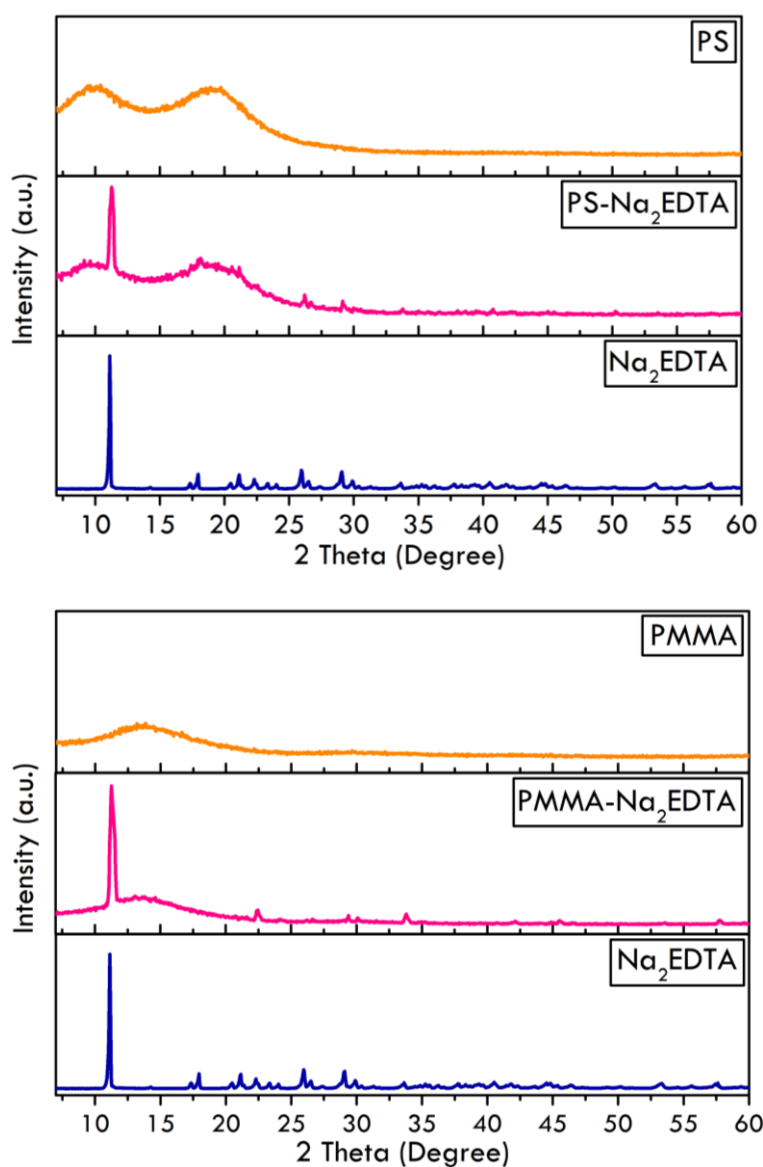
Figure 21 – XRD spectra of polymers, Na₂EDTA and composite samples, PS-Na₂EDTA and PMMA-Na₂EDTA.

Owing to the featuring structure, as well as to the optimized configuration, PS-EDTA(1:1) sample, characterized by the highest content of Na_2EDTA salt, was finally used as the active layer for the implementation of the sensing device.

4.3 Single Fiber Sensor (SFS)

Alongside the production and optimization of fibrous mats, the experimental activity over a sensor device based on a single fiber was also carried out. To this purpose, it was necessary to produce aligned and well-spaced fibers so to create electrodes directly on the fibers. In order to create good electrical contacts between the single fiber and the electrodes, the photolithography technique was used.

Photolithography is one of the most used microfabrication processes to produce specific features on a photosensitive chemical, known as photoresist, spin-coated on a substrate (usually silicon or glass). The photoresist is then exposed to a UV light and a user-defined pattern through the photomask is transferred. Photolithography has numerous applications, including the production of Integrated Circuits (IC) in the semiconductor industry [148], conductive tracks in the Printed Circuit Board (PCB) sector [149], organic field effect transistors [150], and sensors [151], [152]. Photolithography is a rigorously methodical procedure that must be carried out in a cleanroom using a succession of carefully regulated procedures. These techniques begin with cleaning the substrate's surface with acetone or isopropyl alcohol and deionized water, followed by spin coating the substrate with photoresist. Positive photoresist, whose solubility in developer solution increases after exposure, or negative photoresist, whose solubility in developer solution decreases after exposure, may be used. The photoresist is then soft-baked to remove the solvent, followed by exposure to ultraviolet light (photo-polymerization) through a photomask, which is typically composed of quartz covered with an opaque substance such as chromium. The non-crosslinked photoresist is dissolved in a developer solution and the substrate is dried in order to complete the fabrication.

There are numerous physical vapour deposition techniques for producing coatings in a vacuum environment, and they can be divided into two main groups: those involving thermal evaporation techniques, in which material is heated in a vacuum until its vapour pressure exceeds the ambient pressure, and those involving ionic sputtering techniques, in which high-energy ions strike a solid and knock off atoms from its surface [153]. Diode sputtering, ion-beam sputtering, and magnetron sputtering are ionic sputtering techniques. Magnetron sputtering is a deposition technique involving the generation and confinement of a gaseous plasma in a space containing the material to be deposited: the target. The surface of the target is eroded by high-energy ions within the plasma, and the released atoms travel through a vacuum environment before depositing on a substrate to form a thin film.

In order to obtain oriented and well-separated fibers through the electrospinning process, a different collector was used than the one described previously. The collector was designed using the Autodesk Fusion software and printed using an Elegoo Mars LCD-UV printer, which presents an XY resolution of 0.047 mm and a Z axis accuracy of 0.00125 mm. The resin used to realize the collector is a photopolymer resin containing methacrylate monomers that polymerizes at a wavelength of 405 nm due to the presence of photo-initiators.

The shape of the collector has been designed according to literature references [154]–[157], and various tests have been conducted to determine the optimal dimensions, particularly in terms of the distance between A and B points, as shown in **Figure 22**. An adhesive aluminium foil connected to the ground was applied to one of the two faces of the collector to make it conductive. The polymeric solutions were prepared using the same mixtures described previously and the fibers produced were collected on a microscope slide. The **Table 5** shows the electrospinning parameters used for making

aligned fibers, which are the same as those used for fiber mats.
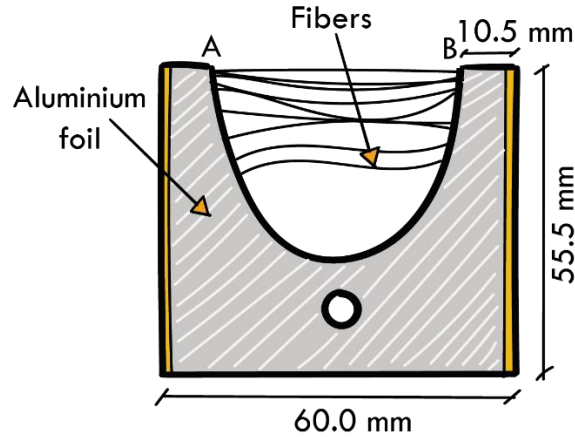
Figure 22 - Schematic representation of the designed collector.

Using the atomic layer deposition technique (ALD), the single fiber is coated with a layer of alumina with a thickness of 6.3 nm, in order to resist the various solvents used in the lithography process.

The ALD processes were carried out in a Fiji 200 ALD reactor (Cambridge Nanotech Inc.) configured with a plasma system and operating with argon as the gas carrier. Al_2O_3 was grown from Trimethylaluminium (TMA) (from Strem Chemicals, 98%) and deionized water (ϱ= 18.2 MΩ·cm) that were stored in dedicated canisters at room temperature (RT). The ALD cycle for alumina deposition consisted of four phases composed by successive pulses and alternate purges of TMA and H_2O. The pulse duration was 0.06 s, while the purge duration was 10 s.
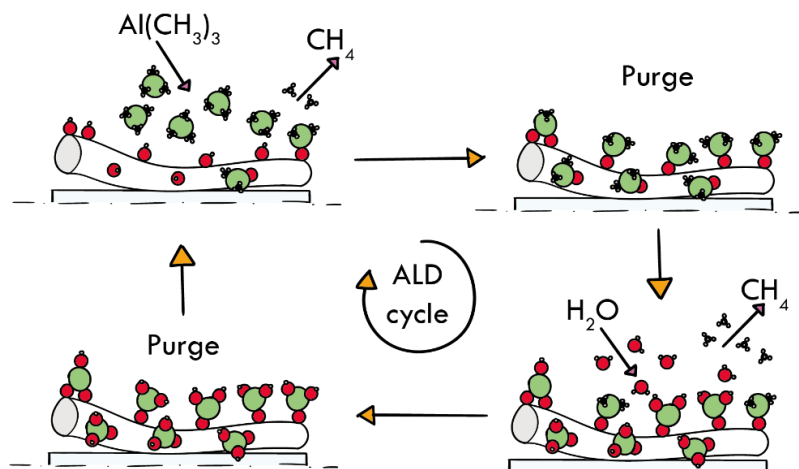
Figure 23 - Phases of ALD cycle for alumina depositions.

The thickness of the deposited material was adjusted by altering the number of cycles, which in this case is equal to 83. The reaction chamber was maintained at 80°C. The deposition conditions were set according to [158], [159].

Once the fiber was coated, the photolithography procedure for the production of the electrodes was initiated. To remove humidity from the sample, the microscope slides on which the fiber was collected were heated for one minute at 90 °C. The positive photoresist MICROPOSIT S1813 G2 was subsequently deposited by utilizing a spin coater (SPS Spin 150). The parameters for the spin coating process were a rotation speed of 2000 RPM, an acceleration of 500 RPM/sec, and a rotation time of 60 seconds. The sample was then baked for 2 minutes at 115°C on a hot plate. The mask used for the realization of the electrodes was designed and built in order to have the dimension of the electrodes as follows: each finger with a width of 5 microns and a length of 100 microns, and the distance between each finger equal to 5 microns. These fingertips are linked to 40,000 micron-square contact areas. The theoretical surface area of a single electrode is 56,920.56 microns squared.
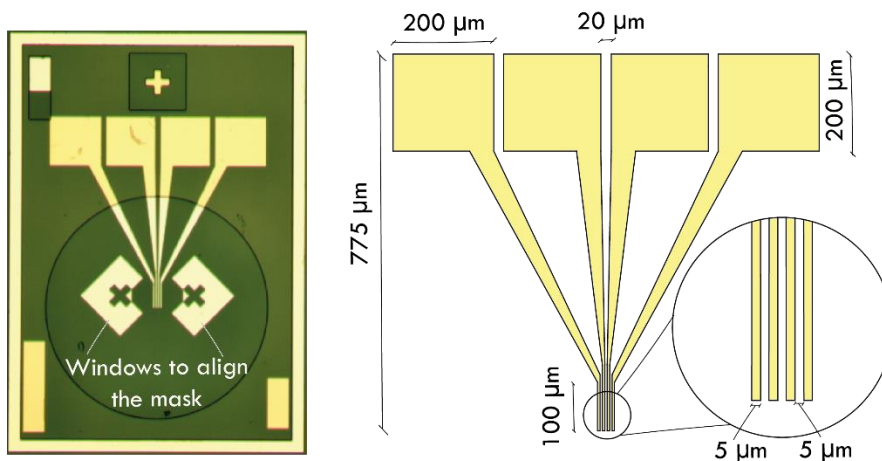
Figure 24 - Photo of microelectrodes realized with an optical microscope and its relative dimensions.

Markers, previously drawn using a personalized shadow mask, were used to find and locate each individual fiber. After that, the MJB4 Mask Aligner (Süss

Microtec) was used to align the mask with the single fiber across the specific windows (**Figure 24**) and to expose the sample to UV light for 12 seconds.

Using an optical microscope (**Figure 24**), the success of the lithography was checked, and then, using a profilometer (Bruker Dektak XT Profilometer), the average thickness of the photoresist was estimated to be 2.106 microns. This thickness was achieved by adjusting the spin coater's rotation speed in order to completely cover and not damage the fibers. The sample was then coated with 40 nm of titanium and 20 nm of gold using sputtering deposition with a deposition rate of 200 Å per second. As the deposition of the material is more or less isotropic, sputtering was chosen over thermal evaporation to create a more robust electrical connection between the fiber and the electrode. Since thermal evaporation is a process for depositing films in a specific way (often vertically with respect to the source), and since the fiber is cylindrical in shape, the electrical contact would not have been optimal. During the lift-off process, the sample is immersed in an organic solvent, such as acetone, in order to remove any remaining photoresist. The immersion time depends on the thickness of the deposited material. In the case of the single fiber sensor, the sample was superficially wetted with acetone for two minutes. Once the acetone was removed, a large part of the metallic coating was lifted using adhesive tape. The sample was then immersed in acetone for one minute to eliminate any residual material. It was then placed in a 0.1 M NaOH solution and sonicated for a few seconds to remove any remaining metal coatings and the Al_2O_3 layer that had been deposited on the fibers using the ALD technique, in order to protect them from the action of various organic solvents.

Micrographs obtained by SEM analyses, performed to verify the success of the single-fiber sensor production process, are shown in **Figure 25**.
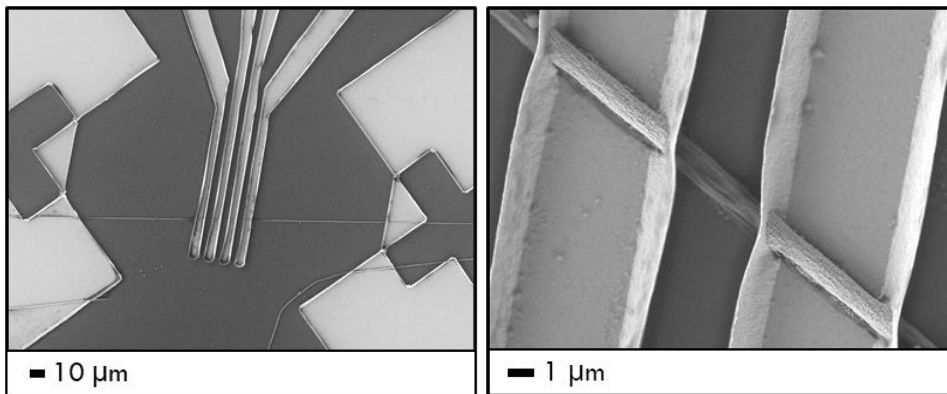
Figure 25 - SEM images of the single fiber sensor.

Four micro-manipulators, coupled with a ModuLab XM ECS (Solartron), were used to carry out a preliminary test of electrical conductivity, but the results showed that the external interference exceeded the signal read, even though the entire measurement setup was electrically shielded with a faraday cage. Photos of the test rig are shown in **Figure 26**.
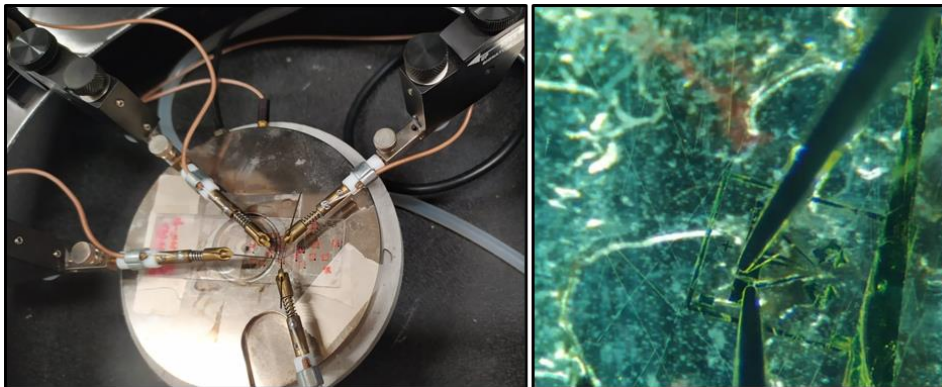
Figure 26 – Singe fiber sensor operating configuration.

In conclusion, preliminary tests on the single-fiber sensor have shown promising prospects. However, the singularity and complexity of the manufacturing process of the single fiber and of its relative implementation as a sensor, influence the cost-effectiveness, simplicity, and rapidity of this approach, making it impractical to apply in the context of environmental monitoring, where other solutions are preferable. But niche applications, like those that have to do with human health, have a lot of possibilities for improvement and optimization.

5

Impedance measurement of sensor

In this chapter the results of the test sensing of the active layers produced are illustrated and commented. Furthermore, the comparison between sensing mechanisms of PtIDE-PS and PtIDE-PSNa2EDTA sensors are shown and discussed.

Electrochemical impedance spectroscopy (EIS) is a widely applied technique to analyse system and material properties using alternate electrical signals of different frequencies and evaluating the electrical output signals. It is a sensitive and robust technique for the investigation of the electrical resistance of a system, the sensitivity towards the changes in bulk, and the interfacial properties at the electrode surface [43].

EIS measurements were carried out using AMEL 7050 galvanostat/potentiostat coupled with AMEL 7200 frequency response analyser with a three-electrode configuration. As described in the previous chapter, platinum interdigitates electrodes (PtIDEs) covered with microfibrous sensing layers were used as working and counter electrodes. As the third electrode, the reference electrode, a platinum wire with a diameter of 0.5 mm and a length of 100 mm was used. As a buffer solution, 0.012 M stock was prepared using concentrated acetic acid (CH_3COOH) and sodium acetate (CH_3COONa). This 4.5 pH solution was obtained using equimolar mixtures of acetic acid and sodium acetate. Baldrianova et al. [160] investigated the effect due to the variation of sodium acetate concentration in the buffer solution during the voltammetric detection of Pb (II) and Cd (II) ions, using in situ bismuth-plated carbon microelectrodes. This study demonstrates that with concentrations below 0.1 M, the signal of the peaks relative to the investigated metal ions increases.

Lead nitrate ($Pb(NO_3)_2$) and thallium nitrate ($TlNO_3$) were used as reagents for the preparation of the electrolytic solutions used during the sensing tests.

The solutions were prepared at different concentrations, using the buffer solution as a base. The concentrations are respectively 10 μg/L, 100 μg/L, 1 mg/L and 100 mg/L for each contaminant examined. The volume of solution used for each measurement is 3 mL and the electrochemical cell was shielded with a Faraday cage, from exposure to external electric fields generated by external devices (such as motors, neon lights, etc.). The EIS measurements were performed with a half-wave amplitude of 10 mVpK and a frequency range of 0.1 Hz to 100.000 Hz. No potential bias was applied. Ten measurement cycles were performed for each concentration, with a 45-second interval between each. This was done to determine the stability and repeatability of each measurement. All measurement cycles for each concentration of the single contaminant were conducted using the same electrodes.

As described in Chapter 2, the first measured frequencies and the last measured frequencies were cut-off in order to improve the quality of the fitting during the analysis of the results and to eliminate possible corrupted values due to the transient phase that occurs at the beginning of each measurement cycle.

The EC-Lab-demo software (BioLogic, France) was used to fit the EIS response based on the various possible equivalent electrical circuit models for such systems. On the basis of the accuracy of the fitting procedure, the most relevant equivalent electrical circuits model was selected for each system, and different elements were quantified. The result of an EIS measurement is an electrochemical impedance spectrum that can be represented as a combination of electrical (resistance, capacitance or inductance) and electrochemical (faradaic) impedances. Moreover, thin films on an electrode surface, such as in this case, behave like dielectrics, as does the double layer that forms spontaneously on an electrified interface. Collected data were interpreted using the Nyquist plot, in which impedance is plotted as a complex number (j = −1) with ZIm (Z") along the y-axis and ZRe (Z') along the x-axis.

EIS curves are reported for both PS and PS-EDTA sensors, using the Nyquist plot (**Figure 27**). Each point on the Nyquist plot is an impedance value at a frequency point. In the X-axis, impedance at the right side of the plot is

registered at low frequency, while, at higher frequencies, the generated impedances are read on the left.
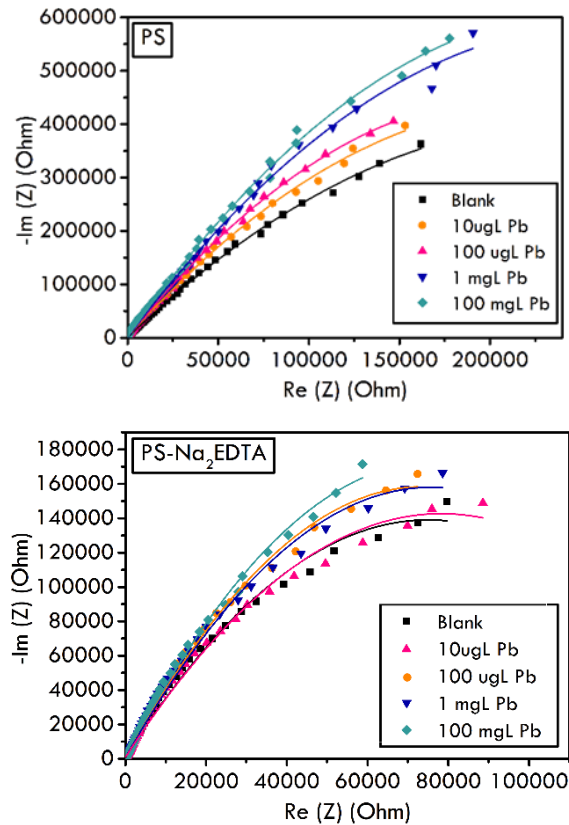
Figure 27 – Impedance curves registered for PS and PS-Na2EDTA samples at increasing Pb(II) concentration.

As evidenced by the obtained results, impedance values in doped sample, PS-EDTA, was lower than in the case of pure PS for all the tested concentrations of Pb, hindering that Na_2EDTA had a great influence on the conductivity of the sample. Indeed, it has been reported in literature that Na_2EDTA dissolved in aqueous solution can work as an electron donor, promoting the accumulation of electrons in the conduction band [161].

It should be also considered that the electrochemical reactions that occur at the metal/film and film/solution interfaces of the barrier layer contribute to the impedance of a system. Since the total impedance of the system comprises all the contribution of the interfacial phenomena, including those at the metal/film/solution interphase and the resistance of the solution, electrical circuits are often used to analyse experimental results [162].

Impedance measurement of sensor

Indeed, more precise consideration can be obtained by impedance curve modelling. In particular, it is well known that in the Nyquist diagram an arc represents a process, whose electrical nature is simultaneously resistive (charge conduction mechanism) and capacitive (polarization or charges separation mechanism), with an associated time constant (t = RC). To this purpose a simplified Randles circuit was used for PS-EDTA sample whereas a CPE (Constant Phase Elements) model was adopted for the pure PS sample, characterized by a straight line in the Nyquist plot.

From the equivalent electrical model **Figure 28**, the values of the electrical components are obtained using least-squares minimisation fitting of the electrochemical impedance spectroscopy spectrum. The variables that are involved in this technique are the resistance solution (Rs), the charge transfer resistance (Rct), and double layer capacitance (CPE) [163].
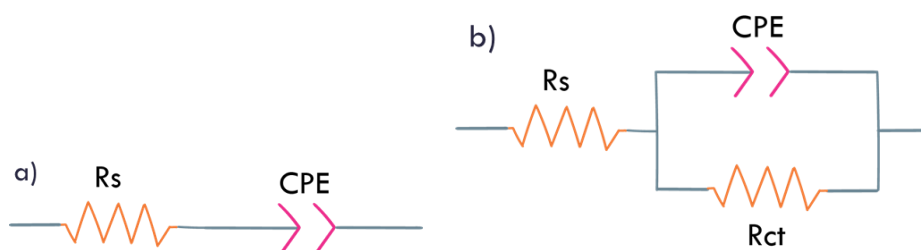
Figure 28 -a) Resistance solution in series with CPE, b) Simplified Randles circuit.

Main extrapolated parameters are reported in the following tables (**Table 6**)(**Table 7**):

Table 6 - Values relative of PtIDE-PS

Solution	Rs (Ohm)	Q (F*s^(n-1))	n
Blank	100.1	1.86e-6	0.898
10 µg/L Pb	96.52	1.69e-6	0.930
100 µg/L Pb	97.06	1.64e-6	0.931
1 mg/L Pb	93.75	1.25e-6	0.924
100 mg/L Pb	91.44	1.25e-6	0.930

Table 7 - Values relative of PtIDE-PSNa$_2$EDTA

Solution	Rs (Ohm)	Rct (Ohm)	Q (F*s^(n-1))	n
Blank	44.3	0.285e6	4.90e-6	0.878
10 μg/L Pb	44.3	0.366e6	4.70e-6	0.882
100 μg/L Pb	44.9	0.376e6	4.67e-6	0.880
1 mg/L Pb	45.09	0.479e6	4.68e-6	0.881
100 mg/L Pb	45.15	1.056e6	4.75e-6	0.880

PS curves were approximated to straight lines over a frequency range of 2500 Hz–1 MHz. The fitted Rct was very large in this case, and the corresponding circuit was simplified by a CPE [164]. In this case the ion transport was hard to occur since due to the absence of the chelating agent, the coverage of Pb on the film surface was not continuous. Indeed, only a bare adsorption of Pb ions, proportional to its concentration in the solution, could be observed as proved by the slight increase of the impedance values. A schematic representation of the detected phenomenon is reported in **Figure 29**.

The characteristic semicircle arc, arisen indeed from the parallel combination of a resistor and capacitor in the case of PS-EDTA sample, suggested the presence of ionic charge carriers due to the presence of the chelating agent. Moreover, the significant deformation of the impedance semicircles, flattened with respect to the ideal case, is caused by the higher Rct values, whose trends increased by increasing the concentration of Pb. Indeed, Rct is associated with electron transfer reactions such as electron-hole recombination. As resulted by the complementary characterizations, since the chelating agent Na$_2$EDTA was well dispersed and encapsulated in the structure of porous PS fibres, an equilibrium in the salt dissociation (EDTA^{-2}/Na^{+2}) was reached when PS-Na$_2$EDTA sensor was conditioned in the buffer solutions. In this condition a distribution of negative charges on the surface of the active layer/solution barrier is formed and EDTA^{-2} is able to bind Pb^{+2} ions. The

complex obtained is stable and proportional to the content of lead ions. Indeed, increasing the contaminant concentration, the Rct increased hindering the decrease of EDTA negative charges and the consequent formation of stable PS-PbEDTA complexes on the surface of the active layer, as depicted in the scheme of **Figure 29**.
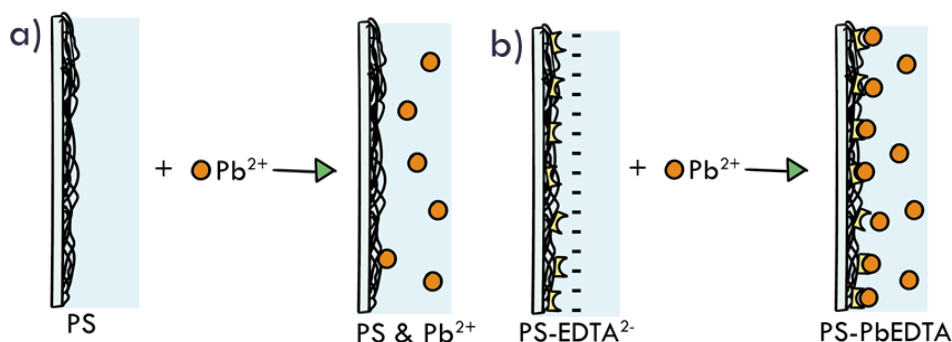
Figure 29 – Schematic representation of the interaction between the surface of the active layer and Pb ions.

The variation of Rct values of PS-EDTA sample, normalized with respect to the Rct_0 value registered in the blank solution, is reported towards the increasing lead concentration in the solution, **Figure 30**. As evident, the normalized Rct value exponentially increases by increasing Pb concentration. The limit of detections (LODs) for Pb(II) ions was calculated using the following formula [165]:

$$LOD = 3.3 * \frac{standard\ deviation\ of\ the\ regression\ line\ (\sigma)}{Slope\ (S)} \quad (9)$$

The calculated value of the limit of detection for Pb(II) was 0.31 μg/L.

It is important to highlight that the reported measurements were recorded at a fixed pH value of the buffer solution, equal to 4.5 and suitable to favour the interaction mechanism between $EDTA^{-2}$ and Pb^{+2}. Indeed, it is well known that both the adsorbent as well as the pH of the working condition influence the Pb adsorption process, including cation exchange, complexation, and precipitation [166].
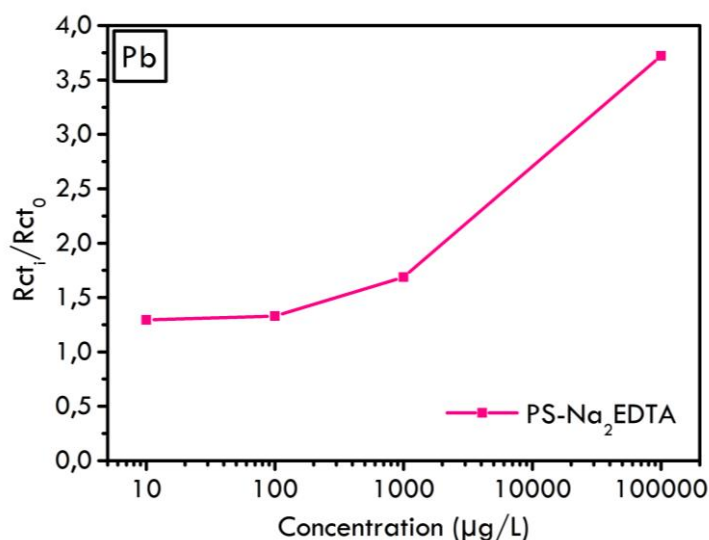
Figure 30 - Normalized Rct values detected in the case of increasing Pb concentrations.

Specifically, in the case of lead in aqueous system, it should be considered that the initial pH influences significantly the adsorption processes, regarding both the states of the functional groups on the surface of the adsorbent and the existing form of the metal ions in solution. In aqueous solution with pH ranging between 2.0 and 8.0, it is known that lead species can exist in three forms: Pb^{2+}, $Pb(OH)^+$ and $Pb(OH)_2$ [23]. For a pH value lower than 6.0, the dominant species is Pb^{2+}, then at pH 3.7 the hydrolysis of Pb^{2+} to form $Pb(OH)^+$ starts and proceeds to form $Pb(OH)^2$ at a pH of 6.8. Finally, over pH > 7.5, the dominant species becomes $Pb(OH)^+$, **Figure 31**.

The strong pH dependent adsorption suggested that the adsorption of Pb (II) was dominated by ion exchange and surface complexation. Under acidic conditions, the functional groups of dissociated EDTA were negatively charged, showing an electrostatic attraction to Pb^{2+} and finding it easy to donate their electron pairs to coordinate with Pb^{2+}. This in order provides first the Pb adsorption and then Pb-EDTA complexation, enhancing Pb immobilization onto the EDTA.
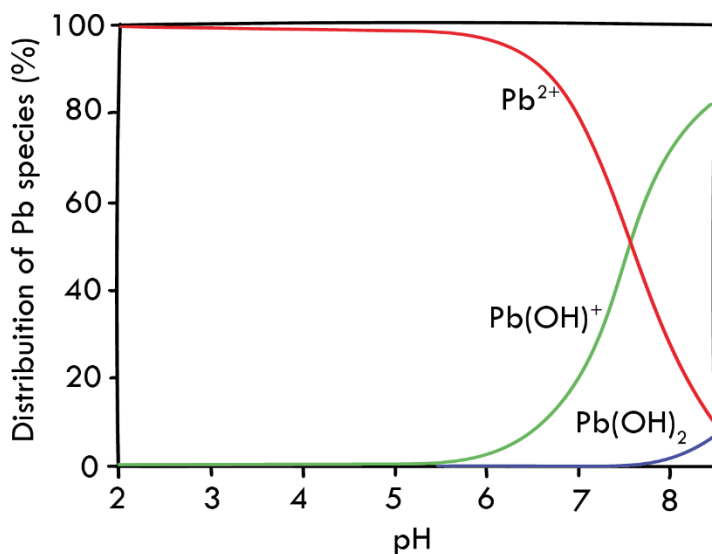
Figure 31 - The distribution of Pb (II) species as a function of pH based on the equilibrium constants (total concentration 100 mg L−1, 25 °C). Adapted from [23].

Finally, considering that EDTA shows a high selectivity to numerous heavy metal ions by regulating the pH of the solution [22], it was evaluated the formation of EDTA complexes with other heavy metal species as a function of pH. Based on the equilibrium constants, thallium (Tl^+) was chosen as an interfering species, **Figure 32**.
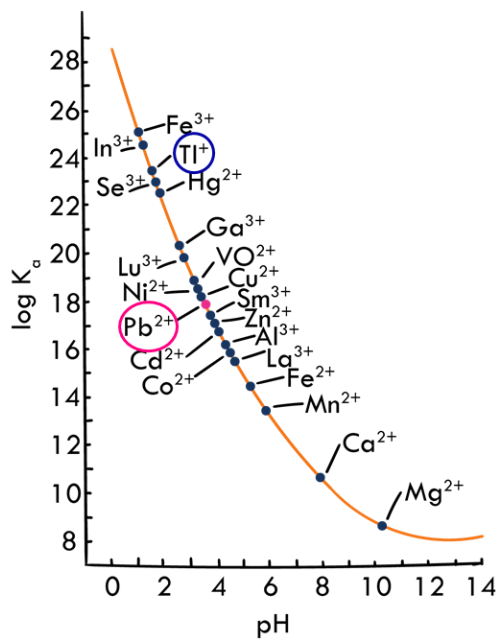
Figure 32 – Equilibrium constants of main heavy metals versus pH values.

Thallium is an extremely toxic heavy metal even if at low concentration, posing substantial risks to ecosystem and human health. As well as lead it is widely discharged from industries in wastewaters [167].

Therefore, the performance of the PS-EDTA sensor was tested through EIS measurements in the same operational conditions as described in the case of lead, at a pH value of 4.5 but using Tl^+ as a new contaminant. By increasing the thallium concentration, registered impedance values showed similar trends with very slight differences. As shown by normalized Rct values, the sensor did not show a significant response hindering its high selectivity to a specific heavy metal when the pH value is precisely regulated.
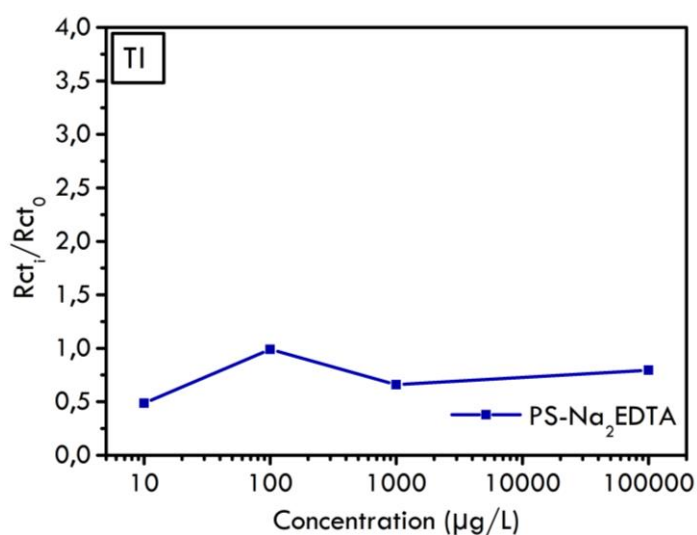
Figure 33 – Normalized Rct values detected in the case of increasing Tl concentrations.

6

Classification and regression learner of experimental data

The topic of data analysis and the training of classification and regression models are discussed in this chapter. The first section describes the two supervised learning techniques and their respective algorithms. Subsequently, all the analysis of the dataset and its engineering is illustrated. Finally, the training of the various algorithms and the discussion on their performance are discussed.

Machine learning (ML) is a type of artificial intelligence (AI) that enables software applications to make more accurate predictions of future occurrences without being explicitly programmed to do so. Inputs for machine learning algorithms consist of historical data used to predict future output values. There are multiple approaches to train machine learning algorithms, each with its own advantages and disadvantages. To understand the benefits and drawbacks of each sort of machine learning, we must first examine the types of data they use. There are two types of data in machine learning: labelled data and unlabelled data. The input and output parameters of labelled data are totally machine-readable, but labelling the data involves a substantial amount of human labour. One or none of the parameters are in a machine-readable format for unlabelled data. This eliminates the requirement for human labour but necessitates more complicated solutions. Different types of machine learning occur: supervised, unsupervised, semi-supervised, reinforcement, transduction and learning to learn [168].

Using supervised learning, the machine is trained using a labelled dataset, and based on this training, the machine predicts the output. Here, the labelled data indicates that some inputs have been mapped to the output. Specifically, we first train the machine with the input and output, and then ask it to predict the outcome using the test dataset [169].

In unsupervised machine learning [170], the algorithm is trained using an unlabelled data set, and the output is predicted without supervision. The models are trained with unclassified and unlabelled data, and the models behave autonomously based on this data. The primary objective of the unsupervised learning algorithm is to group or classify the unsorted dataset based on similarities, patterns, and differences. Instructing machines to discover hidden patterns inside an input dataset.

Semi-supervised learning is an algorithm for machine learning that falls between unsupervised and supervised machine learning [171]. It represents the middle ground between supervised (with labelled training data) and unsupervised (no labelled training data) learning methods and combines labelled and unlabelled training datasets. Although semi-supervised learning is the middle ground between supervised and unsupervised learning and operates on data with a few labels, the majority of the data in semi-supervised learning is unlabelled. As labels are pricey, they may have few labels for business objectives. In contrast to supervised and unsupervised learning, which are based on the presence or absence of labels, unsupervised learning is not dependent on labels. The notion of semi-supervised learning was introduced to solve the shortcomings of supervised and unsupervised learning algorithms. The primary objective of semi-supervised learning is to utilize all accessible data, as opposed to only labelled data as in supervised learning. Initially, similar data is clustered with the aid of an unsupervised learning algorithm, and then the algorithm assists in labelling unlabelled data as labelled data. This is because it costs more money to get labelled data than it does to get unlabelled data.

Reinforcement learning is a feedback-based approach in which an artificial intelligence agent automatically explores its environment by hitting and trailing, taking action, learning from experience, and enhancing its performance [172]. The agent is rewarded for every positive action and penalized for every negative action. Therefore, the reinforcement learning agent's objective is to maximize rewards. In reinforcement learning, unlike supervised learning, there are no labelled data and agents simply learn from their experiences.

Transduction is similar to supervised learning, except it does not explicitly build a function [173]. Instead, it tries to predict new outputs based on training inputs, training outputs, and new inputs. In the process of learning to learn, an algorithm develops its own inductive bias based on what it has learned in the past.

6.1 Supervised Learning

Training and testing are the two main phases that make up the learning process in a model of machine learning that is very straightforward. Throughout the training phase, features are learned by the learning algorithm or learner, and the learning model is constructed using those learned features. Samples of the training data are taken as input during the training process. During the process of testing, the learning model consults the execution engine in order to formulate an estimate for either the test data or the production data. The output of a learning model is tagged data, which can either be the final prediction or the data that has been categorised (**Figure 34**).

As aforementioned, supervised machine learning is one of the most popular and effective methods of machine learning. Several well-known supervised learning algorithms will be explained in this paragraph, along with a more thorough description of supervised learning [168]. When attempting to anticipate a particular output from a given input and having examples of input/output pairings, supervised learning is utilized. These input/output pairings, which constitute our training set, are used to develop a machine learning model. Based on new, never-before-seen data, our aim is to create precise forecasts. Building the training set is frequently labor-intensive, but once it is done, supervised learning automates and frequently accelerates a time-consuming or impossible operation. One of the common issues of supervised learning algorithms are the collection and pre-processing of data. The initial phase is data collection.
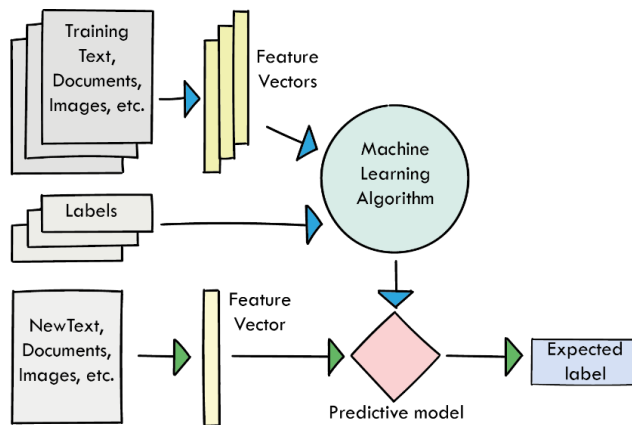
Figure 34 -Supervised Learning Model. Adapted from[168].

If the necessary expert is present, s/he could recommend the most informative fields (attributes, characteristics). If not, the simplest way is brute force, which means measuring all accessible features with the goal of isolating the appropriate (informative, relevant) ones. Nonetheless, a dataset acquired by the brute-force technique is not immediately suited for induction. It typically consists of noise and missing feature data, necessitating extensive pre-processing. There are three aspects necessary for data preparation: real-world data is skewed, high-performance mining algorithms require high-quality data, and high-quality data produces high-quality patterns [174].

- Incomplete, noisy, and inconsistent real-world data might mask useful patterns. This is because:
  a. Incomplete data: missing attribute values, missing particular attributes of interest, or just providing aggregated data;
  b. Noisy data contains errors or outliers;
  c. Inconsistent data comprises code or name conflicts.

- Data preparation reduces the size of the original dataset, which can considerably enhance the efficacy of data mining. The process of selecting relevant data can involve attribute selection (using filtering and wrapping approaches), the removal of anomalies, or the deletion of duplicate entries. Sampling and instance selection are two approaches to data reduction.

- The preparation of data results in the generation of quality data, which in turn results in the generation of quality patterns. For instance, it is possible:
  a) Recover data that is incomplete by either filling in the values that were left out or by minimizing ambiguity;
  b) Clean up the data by eliminating any anomalies or mistakes and deleting any outliers (unusual or exceptional values);
  c) Find a solution to the data conflicts by using your knowledge of the subject area or the judgment of an expert.

As may be deduced from the aforementioned three considerations, the processes of data pre-processing, cleaning, and preparation are not simple undertakings. Consequently, the development of new techniques and approaches for the processing of data is a task that is not only challenging but also essential. Classification and regression are the two primary supervised learning types. Both are examined in depth in the sections that follow.

6.1.1 Classification

In classification, a model predicts unknown values (outputs) based on a set of known values (inputs) (a set of inputs). When the output of an issue is in a categorical format, it is referred to as a classification problem. In classification, instances of a dataset are typically categorised according to different classes [175]. Both structured and unstructured datasets are applicable for classification. Classification terms include classification model, classification method, and feature. A classification algorithm, also known as a classifier, learns from the training dataset and assigns a class to each new data point. In contrast, a classification model predicts the class label for test data using a mapping function determined by the model from the training dataset. Finally, a feature is added to the dataset to aid in the development of a more precise prediction model. There are two classification types unique to one another: binary and multi-label. A binary classification is employed when the outcome has two classes or is binary. In an ambiguity detection procedure, for instance,

the model predicts whether or not phrases are ambiguous, resulting in only two possible outcomes/classes; this is known as binary classification. Nonetheless, multi-label classification consists of an assortment of classes.

6.1.2 Regression

Regression is a supervised learning method that enables the identification of correlations between variables and the prediction of continuous values based on these variables [176]. When the output is continuous, the problem is referred to as a regression problem; for example, predicting a person's weight, age, or salary, predicting the weather, or predicting property prices. X (input variables) is transferred to Y in regression (continuous output). Classification is the process of predicting discrete input labels. In contrast, regression is concerned with the forecasting of continuous data. Simple Linear and Multiple Regressions are the two primary types of regression. In simple linear regression, the relationship between two variables is depicted by a straight line (X and Y). Multiple regression, on the other hand, uses more than one variable and can be further broken down into linear and nonlinear types.

6.2 Supervised learning algorithms

Since the turn of the century, numerous techniques and algorithms for supervised learning have been suggested. It is possible to categorize supervised learning as logic-based, statistics-based, instance-based, support vector machines, etc [177].

Logically Learning Algorithm

Logic-based algorithms respond to the problem through the sequential streaming of data with logic at each stage. The decision tree is seen as a classic example of a logic-based algorithm. It is utilized in regression and classification and is a statistical approach. A decision tree is an example of a conceptually learning supervised algorithm that is mostly used for classification. It provides a collection of decision sequences that, if followed, will lead to predicting the

label of an unlabelled dataset given a dataset of features and their right labels [177]. A logical tree-based decision-support tool has a variety of conditions and conclusions as nodes, and branches connect the circumstances and conclusions. At each level of the process, the decision tree makes decisions and analyses different courses of action, ultimately selecting the most pertinent possibilities. A decision tree is a mathematical model utilized for decision-making. It employs estimations and probabilities to assess potential outcomes and aids in determining if a decision's net gain is worthwhile. The input to the method is an object specified by a set of features. The output for the associated input is a decision. Each internal node in the tree structure evaluates an attribute and is awarded a classification. This method builds a sequential decision stream-based model from the actual values of the dataset's features. The division of decisions into tree-like structures, where at each node of this tree, a judgment is made unless a prediction is produced for a certain input data item. Decision trees are trained on data for classification problems. Frequently, this method demonstrates satisfactory levels of speed and accuracy. It is a popular and widely used technique in machine learning, and it also performs well on relatively smaller datasets. This algorithm divides the set of data into two or more similar sets based on the most important attribute so that as many different groups as possible can be made. A decision tree has the advantages of being simple to understand and interpret, quick, requiring minimal data pre-processing, and able to handle both categorical and numerical data. The problem with this method is that it can lead to a complicated tree structure that isn't generalized enough, and the model itself is very unstable.

Support Vector Machine (SVM)

Support vector machine is an elaborate supervised method that can handle both regression and classification tasks, albeit it is more suitable for classification. It can manage many instances of both continuous and categorical data. It represents the dataset items or records, each with a "n" number of features represented as points in an n-dimensional space, separated into classes by the hyperplane's largest margin (**Figure 35**). In the same n-dimensional space, data points are mapped to predict the category to which they belong

based on which side of the hyperplane they fall. These data points' coordinates are referred to as "support vectors". If a linear hyperplane exists between these classes, the problem becomes quite straightforward [178]. The manual insertion of these properties to have a hyperplane, however, raises the question of whether or not it is actually required. This method utilizes a technique known as "kerneltrick", so the correct response is "not really". Kernels are just a collection of functions that transform a low-dimensional input space into a higher-dimensional one. Some conversions and non-separable problems become separable by making data changes that are complex in nature but appear to be simple. It then determines how to split the dataset based on the labels you provided. This algorithm's advantages include a notable performance boost when the "n" of the n-dimensional space is bigger than the overall size of the sample set. Therefore, it is prudent to employ this approach while working with high-dimensional data. If the hyperplane is well constructed, it will exhibit great performance. Using a subset of training points in the decision function helps the memory economy. However, this algorithm's training period is rather long in comparison to others, so if the dataset is particularly huge, the prediction task will be visibly sluggish. When target classes overlap, i.e., when the dataset has more noise, the performance of the algorithm likewise falls. In the case of probability estimation calculations, an n-fold cross-validation is utilized, which is once again computationally intensive.
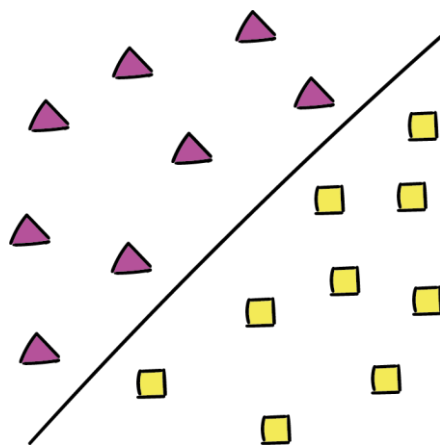
Figure 35 – Illustration of SVM classification with hyperplane.

Statistics-Based Algorithm

Algorithms based on statistics generalize problems using distributive statistics and examine the distribution structure to continue the prediction process. Naïve Bayes is an example of a statistics-based algorithm (**Figure 36**). Naïve Bayes is a basic yet unexpectedly potent predictive modelling technique. It is a collection of approaches for classifying data based on the Bayesian theory of probability. The classifier calculates probabilities for each case. Then, it predicts the outcome with the highest probability. A naive assumption is made that the features are independent and that each pair of features may be classified independently. These classifiers are able to handle an arbitrary number of independent categorical and continuous variables in a manner that is both effective and efficient. Considering a set of variables, X = x1, x2, ..., xt, it is necessary to determine the posterior probability for the event Cj using the sample space set C = c1, c2, ..., ct. The predictor is just X, and C is the collection of categorical levels present in the dependent variable. Using Bayes' rule:

$$P\left(C_j\middle|x_1, x_2, \ldots, x_t\right) * P\left(x_1, x_2, \ldots, x_t\middle|C_j\right)P\left(C_j\right) \quad (10)$$

P(Cj | x1, x2,..., xt) is the posterior probability, which indicates the likelihood that the event X belongs to the class Cj. In Naïve Bayes, the conditional probabilities of the independent variables are assumed to be statistically independent. A new case X is assigned the class level Cj with the highest posterior probability using Bayes' rule. Despite, the basic assumption that predictor variables are independent of one another is not always accurate. This assumption simplifies the classification process by allowing the class conditional densities P(xd | Cj) to be calculated independently for each variable, reducing a multidimensional task to several one-dimensional tasks. Specifically, it transforms a multidimensional density estimation task into a one-dimensional kernel density estimation. This assumption does not significantly alter the posterior probabilities, especially in regions near to the decision borders, so the classification task is unaffected. The assumptions made regarding the distribution of P(xi|Cj) distinguish the various naive Bayes classifiers. The Naïve Bayes algorithm has the advantage that it does not require a very large dataset in order to estimate the necessary parameters. In this case, a training

dataset with a limited amount of data is sufficient. In addition to this, it carries out detailed probability estimates for hypotheses. This approach also offers a helpful opportunity to have an understanding of a variety of learning algorithms.
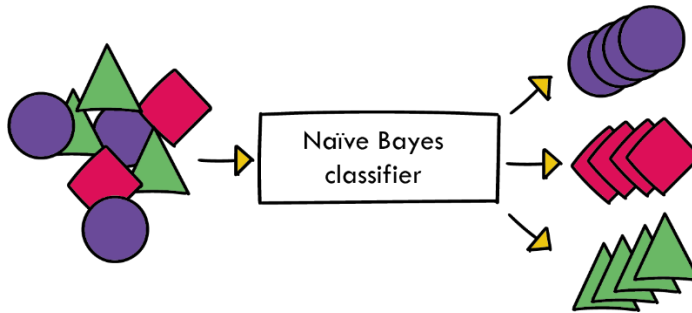
Figure 36 - Classification model of Naïve Bayes.

This classifier is also incredibly quick, especially when compared to other more subtle approaches. It is able to provide effective solutions to diagnostic issues. The results of this procedure are notoriously inaccurate, so it should be avoided.

Lazy Learning Algorithm

Instance-based or lazy learning delays generalization until after the classification process has been completed. It is referred to as "lazy learning" since it slows down the process, and its computational time during the training phase is quite low. In contrast, the classification process is relatively computationally intensive. K-Nearest Neighbor (KNN) is a common instance-based technique for classification and regression applications. KNN is an algorithm that is simple. It is used when there is limited information on the distribution of the data. K-Nearest Neighbor maintains all available records and estimates the class of a new instance based on similarity measures from the most likely nearest neighbours. This technique is considered a lazy learning method because the data members are stored simply in efficient data structures such as hash tables, thereby reducing the computation cost to check and apply the appropriate distance function between the new observation and all K different data points stored, and then to draw any conclusion about the label of the new data point without constructing a mapping function or internal

model, as is the case with other classification techniques. The outcome is determined by a simple majority vote of the KNN of each new data point. The "K" in the KNN algorithm refers to the number of neighbours whose vote is taken for a new record around which those neighbours are visualized just as big as to enclose only the four nearest neighbour data points on the map. This number is determined by the number of neighbours whose votes are taken for a new record. In this case K = 4.
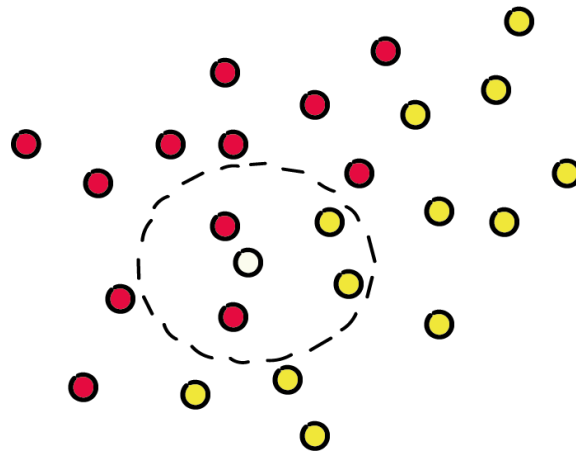
Figure 37 - KNN algorithm approach.

Then a circle with the new data item as the centre will be planned, and the label of the new record will be determined by the virtue of the distance between the record and each of the neighbours. It is possible to construct the borders of each class based on a particular K-value. By utilizing these boundaries, it is possible to effectively separate one class from another. When the value of K is increased, it can be seen that the boundary takes on a smoother appearance. If the value of K is increased to an extremely high number and then continues to approach infinity, it all becomes one class, or the one with the total majority.

The validation error rate and the training error rate are two factors that must be obtained and evaluated using various K-values (**Figure 37**). Here, a new member is represented as a dotted circle, and its class must be anticipated based on its proximity to its four closest neighbours. Due to the fact that we are considering four nearest neighbours, the value of k is 4, and so a circle with the new member at its centre and just four previous members has been drawn. Based on the shortest distance, it is now evident that the next member will be

red. Consequently, we may forecast the label of an unclassified record based on its proximity to the closer the member, the greater the impact of its label on the new record.

Discriminant Analysis

The discriminant analysis (DA) classifier is among elementary and straightforward classifiers. There are two types of discriminant analysis (DA) classifiers: linear discriminant analysis (LDA) and quadratic discriminant analysis (QDA). The decision surface of the LDA classifier is linear, whereas the decision boundary of the QDA is nonlinear. Despite being one of the most well-known classifiers, the DA classifier suffers from a singularity problem. In the singularity problem, DA is unable to calculate the discriminant functions if the dimensions are significantly greater than the number of samples in each class. The covariance matrix is therefore unique and cannot be inverted. Various solutions to this problem have been presented. Regularised linear discriminant analysis is the first technique (RLDA). The identity matrix was multiplied by a regularisation parameter and added to the covariance matrix in this manner. The singularity problem was also solved with the subspace method by reducing the number of high-dimensional data points. A pattern or sample is represented by a vector or set of m features, each of which represents a point in an m-dimensional space (Rm) known as pattern space. The objective of the pattern classification procedure is to train a model to assign a class label to an unknown pattern using the labelled patterns. The class labels indicate the classes or categories of the labelled patterns used to generate the discriminant functions for each class. The decision boundary and regions for each class are then set using the discriminant functions [179], [180].
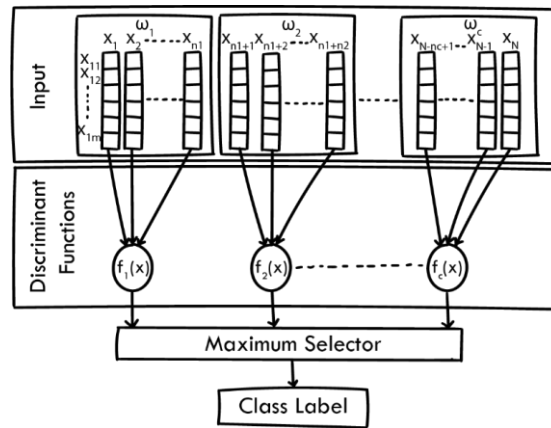
Figure 38 – The structure of a classifier building.

As depicted in **Figure 38** the classifier is represented by c decisions or discriminant functions ({f1, f2, ..., fc}), where c represents the number of classes. The decision functions are utilized to define the decision borders between classes as well as the region or area for each class. Consequently, the discriminant functions are used to determine the class label of the unknown pattern (x) by comparing c various discriminant functions and assigning the class label with the highest score to the unknown sample, as demonstrated by equation (11). Consequently, inside the region ωi the ith discriminant function (fi) will have the greatest value relative to all other discriminant functions [181].If the values of any two discriminant functions are equal (fi(x) = fj(x)), then the unknown pattern (x) lies on the class border.

$$f_i(x) > f_j(x), i, j = 1, 2, \ldots, c\ i \neq j \quad (11)$$

Discriminant functions are utilized to construct the decision boundaries that separate distinct classes into distinct regions (ωi, i = 1, 2,..., c). Consequently, the input space is partitioned into a number of regions, each of which is defined by a number of decision boundaries. In other words, each decision boundary (S_{ij}) consists of two discriminant functions, fi and fj, and separates two distinct areas, i.e., two classes ωi and ωj [181], [182]. Assuming there are two classes (ωi and ωj), there are two distinct discriminant functions (f1 and f2), and the decision boundary is determined as S_{12} = f1 - f2. Calculating the decision area or class label of an unknown pattern x is as follows[183].

$$sgn\big(S_{12}(x)\big) = sgn\big(f_1(x) - f_2(x)\big) = \begin{cases} Class\ 1\colon\ for\ S_{12}(x) \geq 0 \\ Undefined\colon\ for\ S_{12}(x) = 0 \quad (12) \\ Class\ 2\colon\ for\ S_{12}(x) < 0 \end{cases}$$

Linear Regression

The objective of linear regression is to model the relationship between two variables by fitting a linear equation to observed data. One variable is regarded as an explanatory variable, while the other is regarded as a dependent variable. Before attempting to fit a linear model to observed data, a modeler must first assess whether or not the variables of interest are related. This does not necessary indicate that one variable causes the other, but there is a strong correlation between the variables. A scatterplot can be used to determine the strength of the association between two variables. If there appears to be no relationship between the suggested explanatory and dependent variables (i.e., the scatterplot does not indicate a rising or decreasing trend), then fitting a linear regression model to the data will likely not result in a usable model. The correlation coefficient is a useful numerical measure of the relationship between two variables, with a value between -1 and 1 showing the degree of the association between the observed data for the two variables. The equation for a linear regression line is $Y = a + bX$, where X is the explanatory variable and Y is the dependent variable. The least-squares method is the most frequently used technique for fitting a regression line. This method determines the line that best fits the observed data by minimizing the sum of the squares of the vertical deviations between each data point and the line (if a point lies on the fitted line exactly, then its vertical deviation is 0).

Gaussian process regression

Gaussian processes, often known as GP, are a form of supervised learning method that can be utilized to address problems involving regression as well as probabilistic classification. A Gaussian processes regression (GPR) model is capable of making predictions that use prior knowledge (kernels) and providing uncertainty estimates for those predictions. In regression, given a set of observed data points, we wish to fit a function to these data points, then use this function to generate predictions for fresh data points [184]. There are an

endless number of functions that can be used to fit a given set of observed data points. Gaussian processes define a distribution over an unlimited number of functions to do regression in GPR.

In regression, we are attempting to predict an unknown function f using observable data points D (training dataset) from the unknown function f. Traditional nonlinear regression methods often produce a single function that is deemed to best match the dataset. However, it is possible that multiple functions match the observed data points equally well. A model of Gaussian processes describes a probability distribution over all conceivable functions that fit a given set of points. Because we have the probability distribution over all conceivable functions, we can calculate the mean as the function and the variances as measures of prediction confidence. (1) The function (posteriors) updates with new observations; (2) a Gaussian process model is a probability distribution over possible functions; and any finite samples of functions are jointly Gaussian distributed; and (3) the mean function calculated by the posterior distribution of possible functions is the function used for regression predictions [185].

The following is a list of the advantages of using Gaussian processes:

- The measurements are used to interpolate the prediction (at least for regular kernels).

- Because the prediction is probabilistic (Gaussian), one can generate empirical confidence intervals and determine based on those whether or not to retrofit the forecast in some region of interest using online fitting or adaptive fitting.

- Because the prediction is probabilistic (Gaussian), one can generate empirical confidence intervals and determine based on those whether or not to retrofit the forecast in some region of interest using online fitting or adaptive fitting. It is flexible in that it allows for the specification of a variety of kernels. Standard kernels are supplied, but users can also opt to define their own kernels.

The following are some of the disadvantages of using Gaussian processes:

- They do not use sparse representations, meaning that the information from all of the samples and features is used to make predictions.
- When working in high-dimensional areas, namely when the number of features reaches a few hundred, they become less efficient.

Ensemble learning

Ensemble learning methods use numerous machine learning algorithms to give weakly predictive results based on characteristics extracted from a variety of data projections, and then combine these results with various voting mechanisms to achieve higher performance than any single algorithm alone (**Figure 39**). A common ensemble classification model consists of two steps: (1) obtaining classification results with numerous weak classifiers, and (2) integrating multiple results into a consistency function to obtain the final result with voting methods[186]. Bagging, stacking, and boosting are the three primary classes of ensemble learning methods. Bagging is the process of fitting multiple decision trees to distinct samples of the same dataset and averaging the resulting predictions, stacking includes fitting multiple model types to the same data and utilizing a second model to determine the optimal way to combine the predictions and boosting is the sequential addition of ensemble members that correct the predictions provided by previous models and output a weighted average of those predictions.
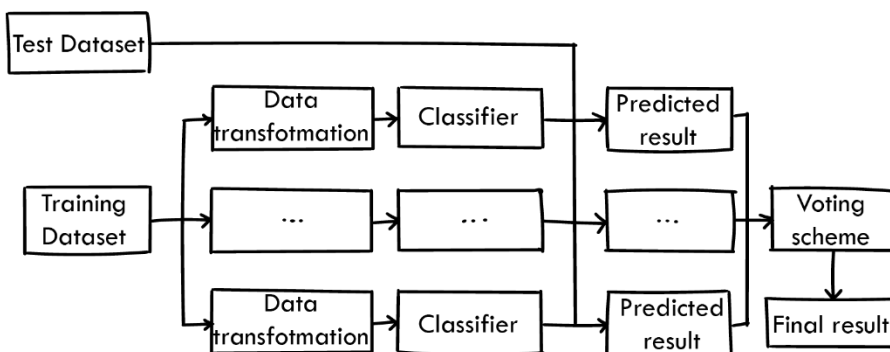
Figure 39 – The framework of ensemble classification.

6.3 Experimental results

In the field of supervised learning, there are two different purposes for which the training is performed: classification and regression. Assuming, as mentioned above, that in supervised learning the output of the model is known a priori, it will be possible to make a prediction on new data for which only the input is known. Based on the type of variable being predicted, it is possible to choose whether to train the model as a classification problem or a regression problem. Classification is used when the variable to be predicted is qualitative or categorical (also known as discrete). Instead, when the target variable is quantitative or continuous, regression models are used. In this study, the aim is to examine the data about environmental monitoring, specifically the detection of heavy metals, which is usually placed in the field of regression, also using a qualitative approach.

6.3.1 Dataset assembling

The dataset was created with the purpose of training various regression and classification models, and the basis for its realization were the results acquired from the impedance measurements of PtIDE-PS-Na$_2$EDTA sensor, tested with different concentration of lead, as well described in Chapter 4. Considering that the percentage difference between the results of the measurements is less than 2%, the original dataset was synthetically increased in size (number of observations) using the following equation (13):

$$V_m = random[-1,1] * 0.02 * V_o + V_o \ (13)$$

where V_o represents the experimental data and V_m the synthetic data. The measurements for each lead concentration have been synthetically expanded in equal numbers in order to maintain the same proportions as the original dataset, but with a larger number of observations. Consequently, the employed dataset has the shape depicted in the **Table 8**.

The frequency spectrum analysed ranges from 0.18 Hz to 50,000 Hz, for a total of 110 frequency points. For each frequency, the values relating to the real part and the imaginary part of the impedance were recorded. So, ultimately, the

Classification and regression learner of experimental data

dataset is composed of 330 features and 930 observations, 186 for each concentration analysed.

Table 8 – Structure of the dataset.

	Features										Response
Observations	Frequency$_{1-1}$	Re [Z]$_{1-1}$	-Im [Z]$_{1-1}$	Frequency$_{2-1}$	Re [Z]$_{2-1}$	-Im [Z]$_{2-1}$	...	Frequency$_{n-1}$	Re[Z]$_{n-1}$	-Im[Z]$_{n-1}$	Log [Concentration of Pb]
	Frequency$_{1-2}$	Re [Z]$_{1-2}$	-Im [Z]$_{1-2}$	Frequency$_{2-2}$	Re [Z]$_{2-2}$	-Im [Z]$_{2-1}$	...	Frequency$_{n-2}$	Re[Z]$_{n-2}$	-Im[Z]$_{n-2}$	Log [Concentration of Pb]
	...	...	...	...	...	...	...	...	...	...	...
	Frequency$_{1-m}$	Re [Z]$_{1-m}$	-Im [Z]$_{1-m}$	Frequency$_{2-m}$	Re [Z]$_{2-m}$	-Im [Z]$_{2-}$	...	Frequency$_{n-m}$	Re[Z]$_{n-m}$	-Im[Z]$_{n-m}$	Log [Concentration of Pb]

6.3.2 Scenarios

In order to analyse the influence of the various features and to work toward the objective of lowering the number of employed features while still maintaining the accuracy of the various models and reducing the amount of time needed for training, sixteen distinct scenarios were investigated. The different scenarios are labelled with the letters *a* to *r*, and each one will be described below. For scenario *a*, the brute force method was used, using all the features in order to demonstrate that some features present in the dataset are not relevant in terms of better accuracy. In contrast, they generate noise that could compromise the quality of the results.

The other scenarios represent a partition of scenario *a*. In fact, in scenario *b*, only the characteristics relating to the real and imaginary parts of the impedance were chosen for each frequency value, for a total of 220 characteristics. Instead, the scenarios *i* and *o* consider only the real and imaginary parts, and then reduce the number of features to 110 for each scenario. Additionally, various scenarios were created using Principal Component Analysis (PCA). PCA is utilized in exploratory data analysis and predictive model development. It is frequently used to reduce the dimensionality of datasets with many features by projecting each data point onto the first few principal components to produce lower-dimensional data while preserving as much of the data's variation as feasible. The first principal component can be defined as a direction that maximizes the projected data's variance. The i-th principal component is orthogonal to the first i - 1 principal components and optimizes the variance of projected data. According to this point of view, the scenarios *c*, *d*, *e*, *l*, *m*, *n*, *p*, *q*, and *r* represent 95%, 97%, and 99% of the variance in the scenarios *b*, *l*, and *o*, respectively. The remaining scenarios, *f*, *g*, and *h*, represent the partition of scenario *b* as a function of the frequency range. In fact, scenario *f*, with 32 features, includes the values of the real and imaginary parts of the frequency in the range between 0.18 and 1 Hz, scenario *g*, with 80 features, in the range between 1.2 and 100 Hz, while scenario *h*, with 108 features, represents the impedance values in the range between 120 and 50,000 Hz. This split was made to see if it is possible to lower the frequency

range of measurements, which would use fewer resources and speed up the process of gathering data. The **Table 9** summarizes all the scenarios previously described.

Table 9 – Summary of scenarios used.

Scenario	Number of features	Description
a	330	All features considered
b	220	Only Re and Im parts of Impedance considered
c	2	PCA of scenario b: 95% of the variance
d	5	PCA of scenario b: 97% of the variance
e	10	PCA of scenario b: 99% of the variance
f	32	Re and Im parts of Impedance in the range 0.18-1 Hz
g	80	Re and Im parts of Impedance in the range 1.2-100 Hz
h	108	Re and Im parts of Impedance in the range 0.12-50 kHz
i	110	Only Re part of Impedance considered
l	1	PCA of scenario i: 95% of the variance
m	2	PCA of scenario i: 97% of the variance
n	5	PCA of scenario i: 99% of the variance
o	110	Only Im part of Impedance considered
p	2	PCA of scenario o: 95% of the variance
q	4	PCA of scenario o: 97% of the variance
r	9	PCA of scenario o: 99% of the variance

6.3.3 Classification Learner

The Classifications Learner App contained in the Statistics and Machine Learning Toolbox for MATLAB R2021 was utilized in order to train and choose the best multi-class supervised classification model (**Figure 40**). After

training different models, their validation errors were compared side-by-side and the model with the lowest error was selected.
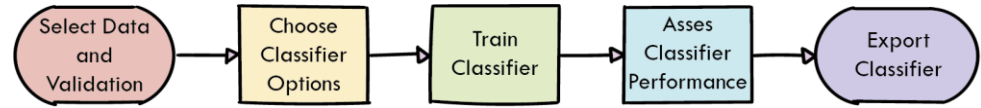
Figure 40 - Workflow for training classification models.

Choosing a validation method to evaluate the predicted accuracy of the fitted models is the initial step. Validation measures model performance on new data relative to training data and assists in selecting the optimal model. Validation assists in preventing overfitting.

Then, prior to train any models, a validation method was selected so that all models in the session could be compared using the same validation method. Specifically, the cross-validation method was selected. Five-fold cross-validations were selected in order to make the partition of data into five disjoint folds. A model was trained for each fold using the out-of-fold observations and the performance of the model was assessed using in-fold data. Finally, it was calculated as the average test error over all folds. The **Table 10** shows the various types of classifiers used. For each scenario, 24 classifiers are used, for a total of 384 trained models.

Table 10 - Classifier used for the training.

Classifier	Classifier type
Decision trees	Fine Tree
	Medium Tree
	Coarse Tree
Discriminant analysis	Linear Discriminant
	Quadratic Discriminant
Naive Bayes	Gaussian Naive Bayes
	Kernel Naive Bayes
Support vector machine	Linear SVM
	Quadratic SVM

	Cubic SVM
	Fine Gaussian SVM
	Medium Gaussian SVM
	Coarse Gaussian SVM
	Fine KNN
	Medium KNN
	Coarse KNN
Nearest neighbors	Cosine KNN
	Cubic KNN
	Weighted KNN
	Boosted Trees
	Bagged Trees
Ensemble	Subspace Discriminant
	Subspace KNN
	RUS Boosted Trees

Table 11 - Selection of models trained.

Scenario	Classifier type	Accuracy (%)	Prediction speed (Object/s)	Training time (s)
f	Medium Tree	97.1	38000	0.459
f	Quadratic Discriminant	100.0	30000	0.518
f	Medium KNN	100.0	13000	0.503
f	Cosine KNN	99.9	19000	0.330
f	Weighted KNN	100.0	19000	0.318
g	Medium KNN	100.0	11000	0.544
g	Cosine KNN	98.7	12000	0.495
g	Weighted KNN	100.0	12000	0.457
h	Weighted KNN	99.5	10000	0.548

o	Linear Discriminant	100.0	21000	0.392
o	Quadratic Discriminant	100.0	21000	0.437
o	Weighted KNN	100.0	10000	0.514

Considering a training time less than 0.55 seconds and an accuracy more than 97%, twelve models finally remained. (**Table 11**). The three models that present the best qualities, in terms of accuracy, training time, and number of features, are all related to scenario f, the one that includes the impedance values in the frequency range between 0.18 and 1 Hz. The three best-performing models were shown to be Weighted KNN, Cosine KNN, and Quadratic Discriminant. Comparing the results of the three models for each scenario in terms of accuracy, it emerged that, in addition to scenario f, equal or greater accuracy was also obtained for other scenarios. In particular, in the case of the Cosine KNN model, scenarios a, b, and o have an accuracy of 100% (blue bar in the **Figure 41**). In the Weighted KNN model, there are even five scenarios (a, b, g, i, o), in addition to scenario f, that have an accuracy of 100%, while for the Quadratic discriminant model, there are four scenarios with an accuracy of 100% (f, g, i, o). As noted previously, scenario f was selected due to its reduced number of characteristics and the low frequency range used for measurements.
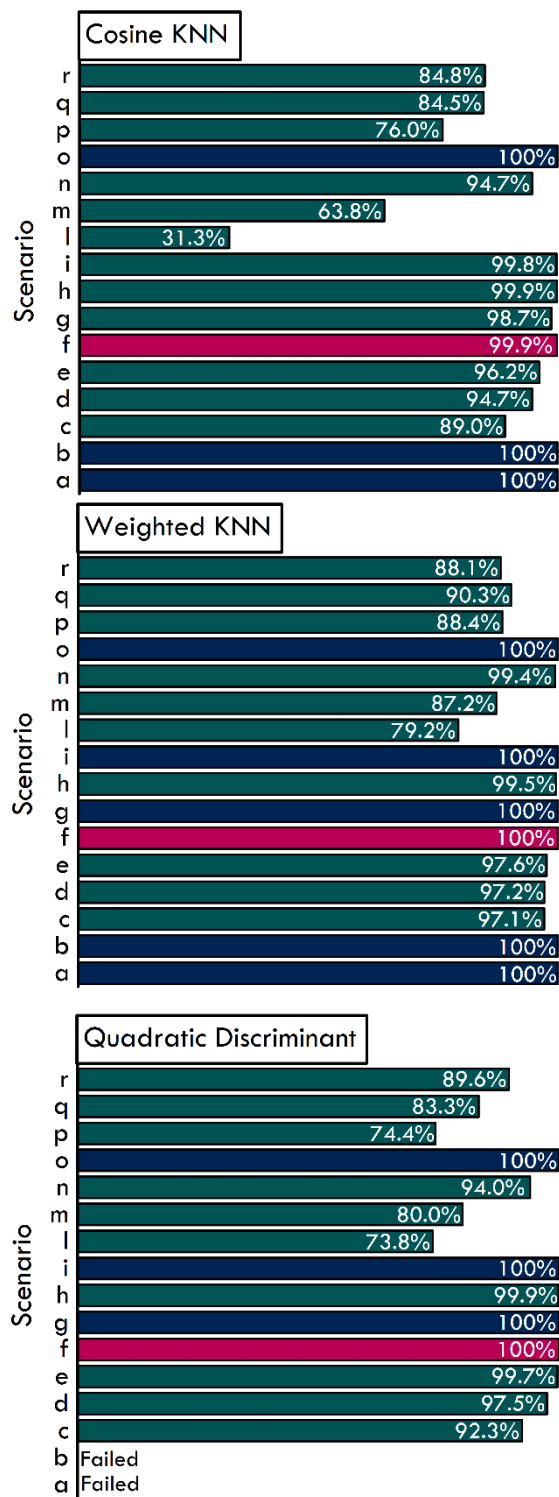
Figure 41 - Comparison of the results of the three best classifiers.
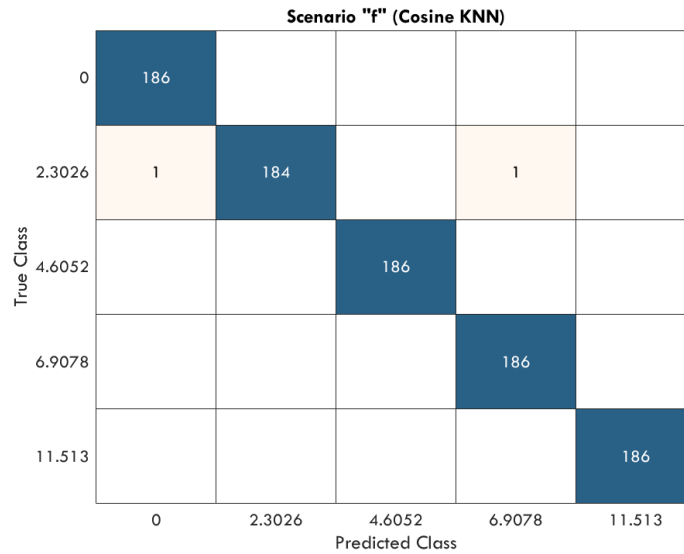
Figure 42 - Confusion matrix relative to model Cosine KNN trained with scenario f dataset.

The **Figure 42** shows an example of a confusion matrix (the one for the Cosine KNN scenario f model) that is a specific table layout that allows visualization of the performance of an algorithm. Each row of the matrix represents the instances in an actual class, while each column represents the instances in a predicted class.

6.3.4 Regression Learner

The Regression Learner App was contained in the Statistics and Machine Learning Toolbox for MATLAB R2021. It chooses, among various algorithms, to train and validate regression models, **Figure 43**. After training different models, their validation errors were compared side-by-side and the model with the lowest error was selected, with the same procedure explained in the previous paragraph dedicated to the classification learner.
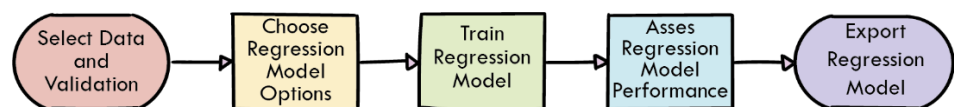
Figure 43 - Workflow for training regression models.

Prior to training any models, as well as for the classification learner, a validation method was selected so that all models in the session can be compared using the same validation method. Specifically, the cross-validation method was selected. Five-fold cross-validations were selected in order to make the partition of data into five disjoint folds. Following the validation phase, the training regression models (**Table 12**) were selected.

Table 12- Regression models used for the training.

Regression	Regression type
Linear Regression	Linear
	Interactions Linear
	Robust Linear
Tree	Fine Tree
	Medium Tree
	Coarse Tree
Support Vector Machine	Linear SVM
	Quadratic SVM
	Cubic SVM
	Fine Gaussian SVM
	Medium Gaussian SVM
	Coarse Gaussian SVM
Ensemble	Boosted Tree
	Bagged Tree
Gaussian Process Regression	Matern 5/2 GPR
	Exponential GPR
	Rational Quadratic GPR

For each scenario, 17 regression models are used, for a total of 272 trained models.

Table 13 - Selection of models trained.

Scenario		RMSE	R^2	Prediction Speed (Object/s)	Training time (s)
a	Medium Gaussian SVM	0.3833	0.99	10000	0.844
a	Bagged Tree	0.3790	0.99	8200	4.241
a	Matern 5/2 GPR	0.3373	0.99	8100	17.205
a	Exponential GPR	0.3545	0.99	7300	21.924
a	Rational Quadratic GPR	0.3377	0.99	7700	35.228
b	Cubic SVM	0.3981	0.99	13000	0.720
b	Bagged Tree	0.3853	0.99	8600	4.418
b	Matern 5/2 GPR	0.3384	0.99	10000	14.224
b	Exponential GPR	0.3527	0.99	11000	22.103
b	Rational Quadratic GPR	0.3390	0.99	9700	32.844
f	Matern 5/2 GPR	0.2796	1.00	17000	11.368
f	Exponential GPR	0.3237	0.99	16000	19.791
f	Rational Quadratic GPR	0.2785	1.00	18000	21.462

Thirteen models remain, considering a root mean square error (RMSE) less than 0.40 and an r-square (R^2) more than 0.99. (**Table 13**). The three models that present the best qualities, in terms of RMSE, R^2 and number of features, are all related to scenario *f*. The three best-performing models were shown to be Rational Quadratic GPR, Exponential GPR, and Matern 5/2 GPR.
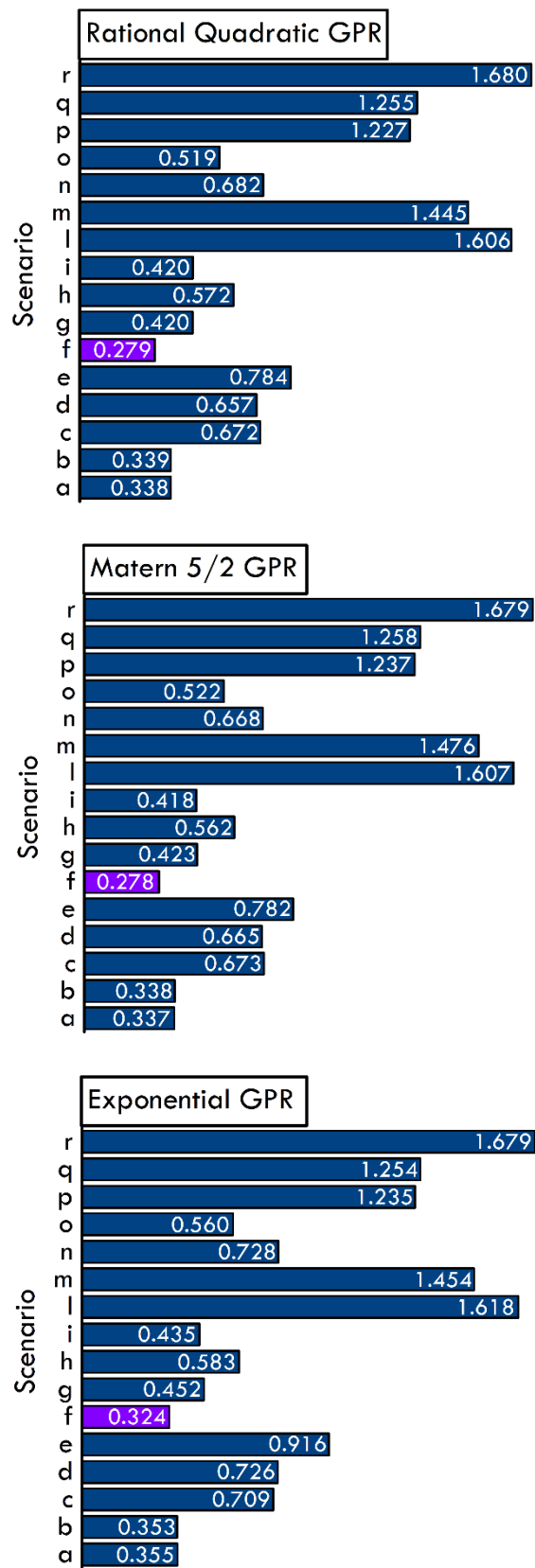
Figure 44 - Comparison of the results of the three best regression models, in term of RMSE.

Comparing the results of the three models for each scenario in terms of RSME, it emerged that, for each of the three models, the best results were attributed to scenario *f* (**Figure 44**).
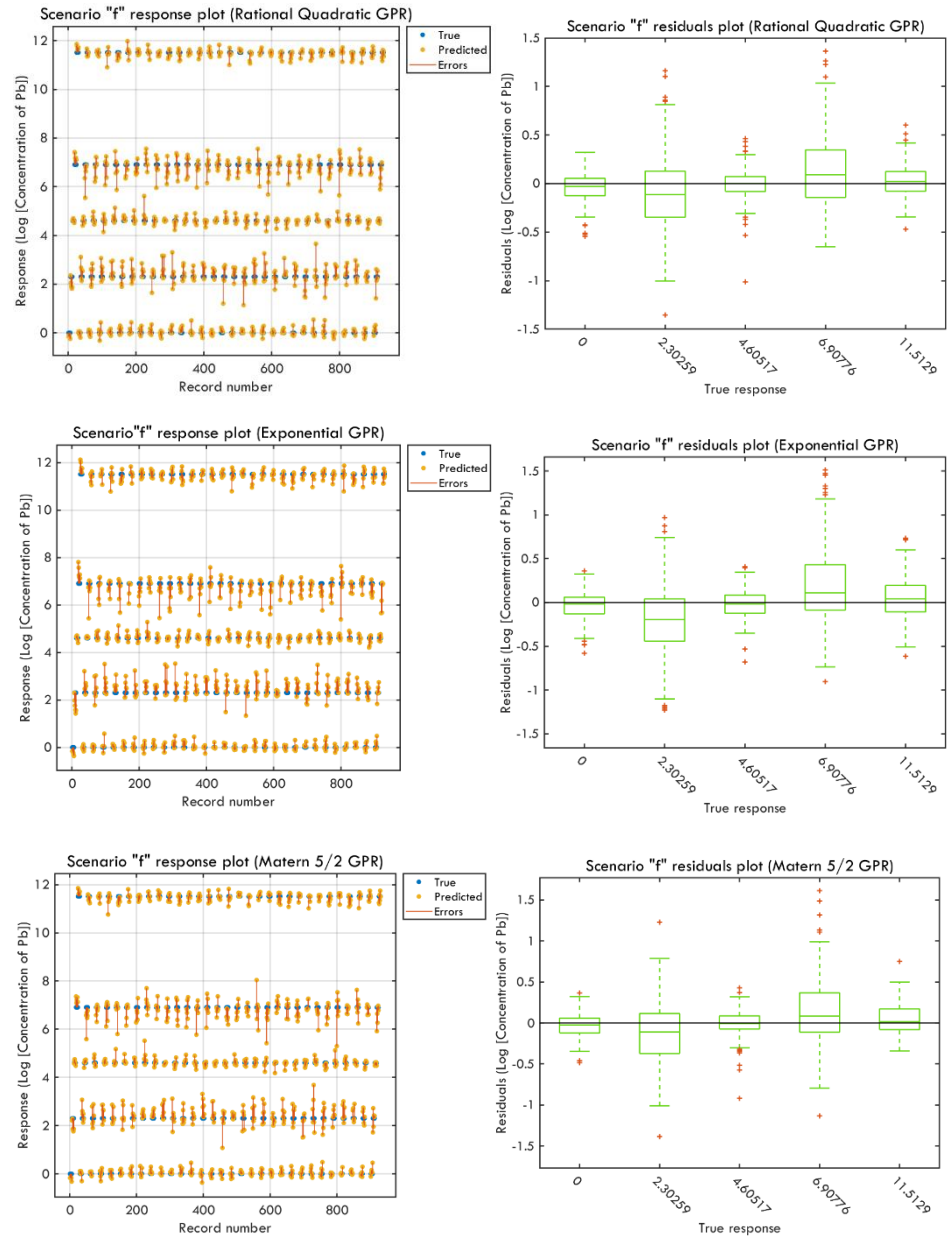
Figure 45 - Response plot and residual plots of the three best regression models trained with the scenario f dataset.

The response plot shows the number of observations in the abscissa and the responses in the ordinate, in terms of the logarithm of the various lead concentrations analysed. The vertical red lines between the prediction and the true value indicate the prediction error committed by the model. Another way

119

of representing the performance of trained regression models is the residuals plot. This plot displays the difference between the predicted and true responses. The analysis of these plots shows that the error value is higher for the response at 2.30259 than at 6.90776, i.e., for concentrations of 10 μg/L and 1 mg/L of lead. Furthermore, among the three regression models chosen, Matern 5/2 GPR is the best-performing one (**Figure 45**).

6.4 Future Goals: Edge Computing

The approach to machine learning, carried out in this study, is divided into two parts: i) training and choice of the most performing model, created on the desktop using the dataset described above, ii) performing runtime inference on a dedicated board, as shown in **Figure 46**. In this study, we focused on the training of different types of algorithms, both by following a qualitative and a quantitative approach. Obviously, this is a preliminary study for the feasibility of the technique using this type of data. In fact, in the future, the training will be carried out with the data acquired directly from a dedicated board and by increasing the number of observations for the creation of the dataset.
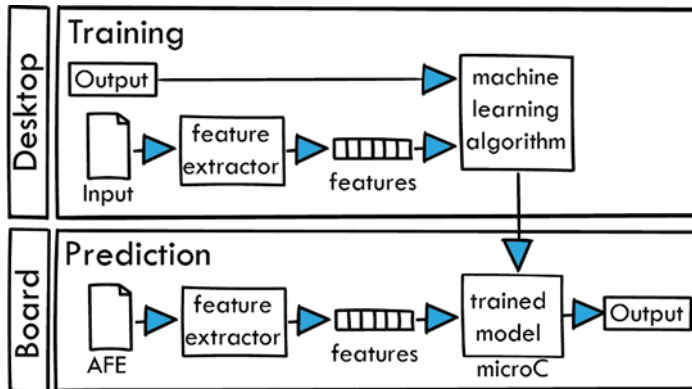
Figure 46 - Block diagram of machine learning approach.

All the measurements reported in this work were made by connecting the sensor (realized as described in Chapter 3) with a potentiostat/galvanostat coupled with a frequency response analyser (FRA), all controlled by a desktop PC. However, the same measurements can be carried out in runtime through a dedicated board on which there is a low-power AFE (analog front end), such

as the AD5941 (Analog Devices), and an ADuCM3029 (Analog Devices) microcontroller where the trained machine learning model can be implemented, as schematized in the **Figure 47**. In this way, it will be possible to predict the result of the measurements, which will be carried out directly in situ, by analysing the inputs collected at runtime.
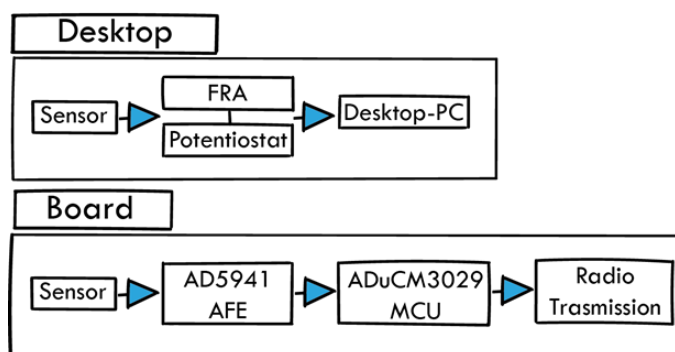
Figure 47 - Block diagram that represents the two ways of carrying out the measurement: using the laboratory instrument and using a dedicated board.

The choice of the various scenarios was focused, above all, on reducing the number of features. This was obtained by partitioning the results according to the different frequency ranges, taking into account only the real or imaginary part of the impedance, or by carrying out a PCA analysis of the different scenarios (*b*, *i*, *o*). Among all these, scenario *f*, which represents the impedance values acquired at low frequency (0.18 Hz–1 Hz), is composed of only 32 features, compared to the initial 330 (scenario *a*), and above all allows to reduce the duration of the acquisition phase as well as the data storage space, and therefore is more suitable for implementation on a resource-constrained device, such as a microcontroller. Furthermore, a model with fewer parameters and shorter inference times was obtained. Moreover, the analysis of the results, examined in Chapter 4, clearly shows that the greatest difference in impedance, at the different concentrations of lead tested, mainly occurs in the low frequency range, as confirmed by the results obtained from training the various models using scenario *f* as a dataset.

Considering also that the time to carry out the measurement in the complete frequency range (0.18–50,000 Hz) is about twenty minutes, using the scenario *f* (0.18–1 Hz) to train the classification and regression models, that, as

highlighted several times, maintains the same performance even by reducing the number of features, the data acquisition time drops to around five minutes. This leads to a reduction in the energy required to power the system, a fundamental aspect of the implementation of an IoT system. In addition, machine learning models have been chosen so that can be easily implemented in microcontrollers, able to deduce the correct prediction in an inference time in the order of ten milliseconds [187]. Ultimately, the data analysis carried out in this study was focused on a future implementation of an IoT system, ultra-low power, based on a microcontroller, powered by batteries, and equipped with a radio transmission system. Also, putting the trained model directly on the microcontroller will make it possible for the algorithm to keep learning.

7

Conclusions

This thesis work focused on the design and the development of a sensor device for the environmental monitoring, for the detection of heavy metals in aqueous solution.

The first step was to design and build the active layer of the sensor. This layer was obtained through the electrospinning technique, using three different polymers to produce microfibers both pure, containing only the polymer, and composite, added with the disodium salt of EDTA, known to be a chelating substance for heavy metals.

Two different ways to make the sensor were addressed: the single fiber sensor (SFS) and the fibers mat directly collected on interdigitate electrodes. The first approach showed promising results, but the singularity and complexity of the single fiber manufacturing process, as well as its implementation as a sensor device, resulted not feasible for its application in the environmental monitoring, where simpler and cheaper solutions are required, such as that adopted in the second approach.

The production of electrospun materials was optimized by controlling numerous parameters and finally, among the tested polymers, polystyrene was chosen for its good capability to maintain entrapped Na_2EDTA grains, the surface porosity, and the good resistance in the solution conditions. Then, the optimized active layer, in terms of Na_2EDTA concentration (additive/polymer weight ratio= 50.0/50.0) and stability, was implemented in the impedimetric PtIDE-PS-Na_2EDTA sensor.

The sensing tests of the active layer were carried out using the electrochemical impedance spectroscopy technique at different concentrations of lead and thallium, used as contaminants. The frequency range used for the measurements was set between 0.1 and 100000 Hz, with an amplitude of 10 mVpK.

Conclusions

The results of the sensing tests showed that PtIDE-PS-Na$_2$EDTA sensor was able to detect different Pb concentrations and to be selective, compared to other heavy metals, in particular thallium, according to the pH value of the solution.

In addition, using the obtained sensing data, this work also aimed at training a machine learning model, that can be implemented on a portable device using a low-power microcontroller. In order to analyse the influence of the various features and, at the same time, to lower the number of employed features while still maintaining the accuracy of the various models and reducing the amount of time needed for training, sixteen distinct scenarios were investigated. The choice of the various scenarios focused above all on reducing the number of features, which was obtained by partitioning the results according to the different frequency ranges, considering only the real or imaginary part of the impedance, or by carrying out a PCA analysis of the different scenarios (b, i, o).

The results of the training of classification and regression models, over the experimental data, highlighted that the scenario f, which represents the impedance values acquired at low frequency (0.18 Hz–1 Hz), and composed only by 32 features, compared to the initial 330 (scenario a), allowed to reduce the duration of the acquisition phase as well as the data storage space, and therefore resulted more suitable for the implementation on a resource-constrained device, such as a microcontroller.

In conclusion, the results of this work highlighted the feasibility to implement a sensing device able to discriminate lead in low concentration, among other contaminants. Moreover, the extensive analysis of sensing data, lay the basis for the real-life application of the device in the industrial field.

References

[1]   J. O. Duruibe, M. O. C. Ogwuegbu, and J. N. Egwurugwu, "Heavy metal pollution and human biotoxic effects," *Int. J. Phys. Sci.*, vol. 2, no. 5, pp. 112–118, 2007, doi: 10.1016/j.proenv.2011.09.146.

[2]   J.-J. Kim, Y.-S. Kim, and V. Kumar, "Heavy metal toxicity: An update of chelating therapeutic strategies," *J. Trace Elem. Med. Biol.*, vol. 54, pp. 226–231, 2019.

[3]   A. G. Mukherjee, U. R. Wanjari, K. Renu, B. Vellingiri, and A. V. Gopalakrishnan, "Heavy metal and metalloid-induced reproductive toxicity," *Environ. Toxicol. Pharmacol.*, p. 103859, 2022.

[4]   M. Balali-Mood, K. Naseri, Z. Tahergorabi, M. R. Khazdair, and M. Sadeghi, "Toxic mechanisms of five heavy metals: mercury, lead, chromium, cadmium, and arsenic," *Front. Pharmacol.*, vol. 12, p. 643972, 2021.

[5]   W. S. Chai *et al.*, "A review on conventional and novel materials towards heavy metal adsorption in wastewater treatment application," *J. Clean. Prod.*, vol. 296, p. 126589, 2021.

[6]   R. W. Herschy, "Water quality for drinking: WHO guidelines," *Encycl. Earth Sci. Ser.*, pp. 876–883, 2012, doi: 10.1007/978-1-4020-4410-6_184.

[7]   P. B. Tchounwou, C. G. Yedjou, A. K. Patlolla, and D. J. Sutton, *Molecular, clinical and environmental toxicicology Volume 3: Environmental Toxicology*, vol. 101. 2012.

[8]   M. Tiemann, "Safe Drinking Water Act (SDWA): A summary of the act and its major requirements," *Rural Water Syst. Challenges Drink. Water Needs*, pp. 55–80, 2015.

[9]   C. Zamora-Ledezma *et al.*, "Heavy metal water pollution: A fresh look about hazards, novel and conventional remediation methods," *Environ. Technol. Innov.*, vol. 22, p. 101504, 2021.

References

[10] J. O. Duruibe, M. O. C. Ogwuegbu, and J. N. Egwurugwu, "Heavy metal pollution and human biotoxic effects," *Int. J. Phys. Sci.*, vol. 2, no. 5, pp. 112–118, 2007.

[11] R. Li *et al.*, "Efficient and rapid removal of EDTA-chelated Pb (II) by the Fe (III)/flue gas desulfurization gypsum (FGDG) system," *J. Colloid Interface Sci.*, vol. 542, pp. 379–386, 2019.

[12] L. A. Malik, A. Bashir, A. Qureashi, and A. H. Pandith, "Detection and removal of heavy metal ions: a review," *Environ. Chem. Lett.*, vol. 17, no. 4, pp. 1495–1521, 2019.

[13] A. Pohl, "Removal of heavy metal ions from water and wastewaters by sulfur-containing precipitation agents," *Water, Air, Soil Pollut.*, vol. 231, no. 10, pp. 1–17, 2020.

[14] H. I. Syeda and P.-S. Yap, "A review on three-dimensional cellulose-based aerogels for the removal of heavy metals from water," *Sci. Total Environ.*, vol. 807, p. 150606, 2022.

[15] B. Nowack and J. M. VanBriesen, "Chelating agents in the environment," ACS Publications, 2005.

[16] T. A. Saleh, M. Mustaqeem, and M. Khaled, "Water treatment technologies in removing heavy metal ions from wastewater: A review," *Environ. Nanotechnology, Monit. Manag.*, vol. 17, p. 100617, 2022.

[17] S. J. S. Flora and V. Pachauri, "Chelation in metal intoxication," *Int. J. Environ. Res. Public Health*, vol. 7, no. 7, pp. 2745–2788, 2010.

[18] D. Leštan, C. Luo, and X. Li, "The use of chelating agents in the remediation of metal-contaminated soils: a review," *Environ. Pollut.*, vol. 153, no. 1, pp. 3–13, 2008.

[19] L. Wu, H. Wang, H. Lan, H. Liu, and J. Qu, "Adsorption of Cu (II)–EDTA chelates on tri-ammonium-functionalized mesoporous silica from aqueous solution," *Sep. Purif. Technol.*, vol. 117, pp. 118–123, 2013.

[20] S. Gluhar, A. Kaurin, and D. Lestan, "Soil washing with biodegradable chelating agents and EDTA: technological feasibility, remediation

efficiency and environmental sustainability," *Chemosphere*, vol. 257, p. 127226, 2020.

[21] E. Faulques, D. L. Perry, S. Lott, J. D. Zubkowski, and E. J. Valente, "Study of coordination and ligand structure in cobalt-EDTA complexes with vibrational microspectroscopy," *Spectrochim. Acta Part A Mol. Biomol. Spectrosc.*, vol. 54, no. 6, pp. 869–878, 1998.

[22] J. McMurry, *Organic Chemistry, 6 Eds.* 2004.

[23] J. Huang *et al.*, "Pb (II) removal from aqueous media by EDTA-modified mesoporous silica SBA-15," *J. Colloid Interface Sci.*, vol. 385, no. 1, pp. 137–146, 2012.

[24] J. Dong, Q. Fang, H. He, Y. Zhang, J. Xu, and Y. Sun, "Electrochemical sensor based on EDTA intercalated into layered double hydroxides of magnesium and aluminum for ultra trace level detection of lead (II)," *Microchim. Acta*, vol. 182, no. 3, pp. 653–659, 2015.

[25] M. Mahadik *et al.*, "EDTA modified PANI/GO composite based detection of Hg (II) ions," *Front. Mater.*, vol. 7, p. 81, 2020.

[26] H. Chen *et al.*, "Preparation of MgAl-EDTA-LDH based electrospun nanofiber membrane and its adsorption properties of copper (II) from wastewater," *J. Hazard. Mater.*, vol. 345, pp. 1–9, 2018.

[27] M. A. Deshmukh, G. A. Bodkhe, S. Shirsat, A. Ramanavicius, and M. D. Shirsat, "Nanocomposite platform based on EDTA modified Ppy/SWNTs for the sensing of Pb (II) ions by electrochemical method," *Front. Chem.*, vol. 6, p. 451, 2018.

[28] K. Siraj and S. A. Kitte, "Analysis of Copper, Zinc and Lead using Atomic Absorption Spectrophotometer in ground water of Jimma town of Southwestern Ethiopia," *Int. J. Chem. Anal. Sci.*, vol. 4, no. 4, pp. 201–204, 2013, doi: 10.1016/j.ijcas.2013.07.006.

[29] A. M. Massadeh, A. A. Alomary, S. Mir, F. A. Momani, H. I. Haddad, and Y. A. Hadad, "Analysis of Zn, Cd, As, Cu, Pb, and Fe in snails as bioindicators and soil samples near traffic road by ICP-OES," *Environ.*

References

Sci. Pollut. Res., vol. 23, no. 13, pp. 13424–13431, 2016, doi: 10.1007/s11356-016-6499-2.

[30] T. Daşbaşi, Ş. Saçmaci, N. Çankaya, and C. Soykan, "A new synthesis, characterization and application chelating resin for determination of some trace metals in honey samples by FAAS," *Food Chem.*, vol. 203, pp. 283–291, 2016, doi: 10.1016/j.foodchem.2016.02.078.

[31] J. Koelmel and D. Amarasiriwardena, "Imaging of metal bioaccumulation in Hay-scented fern (Dennstaedtia punctilobula) rhizomes growing on contaminated soils by laser ablation ICP-MS," *Environ. Pollut.*, vol. 168, pp. 62–70, 2012, doi: 10.1016/j.envpol.2012.03.035.

[32] L. A. Malik, A. Bashir, A. Qureashi, and A. H. Pandith, "Detection and removal of heavy metal ions: a review," *Environ. Chem. Lett.*, vol. 17, no. 4, pp. 1495–1521, 2019, doi: 10.1007/s10311-019-00891-z.

[33] F. Scholz, "Voltammetric techniques of analysis: the essentials," *ChemTexts*, vol. 1, no. 4, pp. 1–24, 2015, doi: 10.1007/s40828-015-0016-y.

[34] S. G. R. Avuthu *et al.*, "A Screen Printed Phenanthroline-Based Flexible Electrochemical Sensor for Selective Detection of Toxic Heavy Metal Ions," *IEEE Sens. J.*, vol. 16, no. 24, pp. 8678–8684, 2016, doi: 10.1109/JSEN.2016.2572184.

[35] A. A. Roselin, R. Karkuzhali, N. Anandhan, and G. Gopu, "Bismuth titanate (Bi4Ti3O12, BTO) sol–gel spin coated thin film for heavy metal ion detection," *J. Mater. Sci. Mater. Electron.*, vol. 32, no. 20, pp. 24801–24811, 2021, doi: 10.1007/s10854-021-06937-9.

[36] M. A. Deshmukh *et al.*, "EDTA-modified PANI/SWNTs nanocomposite for differential pulse voltammetry based determination of Cu(II) ions," *Sensors Actuators, B Chem.*, vol. 260, pp. 331–338, 2018, doi: 10.1016/j.snb.2017.12.160.

[37] C. A. Martínez-Huitle, N. Suely Fernandes, M. Cerro-Lopez, and M. A.

Quiroz, "Determination of trace metals by differential pulse voltammetry at chitosan modified electrodes," *Port. Electrochim. Acta*, vol. 28, no. 1, pp. 39–49, 2010, doi: 10.4152/pea.201001039.

[38] M. A. E. Mhammedi, M. Achak, M. Hbid, M. Bakasse, T. Hbid, and A. Chtaini, "Electrochemical determination of cadmium(II) at platinum electrode modified with kaolin by square wave voltammetry," *J. Hazard. Mater.*, vol. 170, no. 2–3, pp. 590–594, 2009, doi: 10.1016/j.jhazmat.2009.05.024.

[39] A. Terbouche, C. Ait-ramdane-terbouche, S. Djebbar, O. Benali-baitich, and D. Hauchard, "Sensors and Actuators B : Chemical Effectiveness study of sensor based on modified cavity microelectrode by Algerian humic acid – polyaniline composites using square wave voltammetry," *Sensors Actuators B. Chem.*, vol. 169, pp. 297–304, 2012, doi: 10.1016/j.snb.2012.04.085.

[40] M. Nodehi, M. Baghayeri, and A. Kaffash, "Chemosphere Application of BiNPs / MWCNTs-PDA / GC sensor to measurement of Tl (1) and Pb (II) using stripping voltammetry," *Chemosphere*, vol. 301, no. February, p. 134701, 2022, doi: 10.1016/j.chemosphere.2022.134701.

[41] A. Malara, A. Fotia, E. Paone, and G. Serrano, "Electrospun nanofibers and electrochemical techniques for the detection of heavy metal ions," *Materials (Basel).*, vol. 14, no. 11, 2021, doi: 10.3390/ma14113000.

[42] I. Jlalia *et al.*, "Adsorption Characteristics of WFD Heavy Metal Ions on New Biosourced Polyimide Films Determined by Electrochemical Impedance Spectroscopy," *J. Inorg. Organomet. Polym. Mater.*, vol. 31, no. 6, pp. 2471–2482, 2021, doi: 10.1007/s10904-020-01842-w.

[43] B. Petovar, K. Xhanari, and M. Finšgar, "A detailed electrochemical impedance spectroscopy study of a bismuth-film glassy carbon electrode for trace metal analysis," *Anal. Chim. Acta*, vol. 1004, pp. 10–21, 2018.

[44] B. A. Patel, *Electrochemistry for Bioanalysis*, 1st ed. 2021.

[45] Y. Lu, X. Liang, C. Niyungeko, J. Zhou, J. Xu, and G. Tian, "A review

of the identification and detection of heavy metal ions in the environment by voltammetry," *Talanta*, vol. 178, no. August 2017, pp. 324–338, 2018, doi: 10.1016/j.talanta.2017.08.033.

[46] Z. Zhang, Y. Hu, H. Zhang, and S. Yao, "Novel layer-by-layer assembly molecularly imprinted sol-gel sensor for selective recognition of clindamycin based on Au electrode decorated by multi-wall carbon nanotube," *J. Colloid Interface Sci.*, vol. 344, no. 1, pp. 158–164, 2010, doi: 10.1016/j.jcis.2009.12.022.

[47] J. M. Zen, C. C. Yang, and A. S. Kumar, "Voltammetric behavior and trace determination of Pb2+ at a mercury-free screen-printed silver electrode," *Anal. Chim. Acta*, vol. 464, no. 2, pp. 229–235, 2002, doi: 10.1016/S0003-2670(02)00472-5.

[48] J. Kim and S. Bae, "Fabrication of Ti / Ir-Ru electrode by spin coating method for electrochemical removal of copper," *Environ. Eng. Res.*, vol. 24, no. 4, pp. 646–653, 2019, doi: https://doi.org/10.4491/eer.2018.229.

[49] K. Pokpas, N. Jahed, O. Tovide, P. G. Baker, and E. I. Iwuoha, "Nafion-Graphene Nanocomposite in situ Plated Bismuth-film Electrodes on Pencil Graphite Substrates for the Determination of Trace Heavy Metals by Anodic Stripping Voltammetry," *Int. J. Electrochem. Sci.*, vol. 9, pp. 5092–5115, 2014.

[50] Q. Bao *et al.*, "Electrochemical performance of a three-layer electrode based on Bi nanoparticles , multi-walled carbon nanotube composites for simultaneous Hg (II) and Cu (II) detection," *Chinese Chem. Lett.*, vol. 31, no. 10, pp. 2752–2756, 2020, doi: 10.1016/j.cclet.2020.06.021.

[51] M. Abu, J. Mazumder, H. Sheardown, and A. Al-ahmed, *Functional Polymers*, 1st ed. Springer International Publishing, 2019.

[52] D. Tonelli, E. Scavetta, and I. Gualandi, "Electrochemical deposition of nanomaterials for electrochemical sensing," *Sensors*, vol. 19, no. 5, p. 1186, 2019, doi: 10.3390/s19051186.

[53]   G. Aragay and A. Merkoçi, "Nanomaterials application in electrochemical detection of heavy metals," *Electrochim. Acta*, vol. 84, pp. 49–61, 2012, doi: 10.1016/j.electacta.2012.04.044.

[54]   P. M. Lee, Z. Wang, X. Liu, Z. Chen, and E. Liu, "Glassy carbon electrode modified by graphene-gold nanocomposite coating for detection of trace lead ions in acetate buffer solution," *Thin Solid Films*, vol. 584, pp. 85–89, 2015, doi: 10.1016/j.tsf.2015.03.017.

[55]   S. Sang *et al.*, "Facile synthesis of AgNPs on reduced graphene oxide for highly sensitive simultaneous detection of heavy metal ions," *RSC Adv.*, vol. 7, no. 35, pp. 21618–21624, 2017, doi: 10.1039/c7ra02267k.

[56]   S. Lee, S. K. Park, E. Choi, and Y. Piao, "Voltammetric determination of trace heavy metals using an electrochemically deposited graphene/bismuth nanocomposite film-modified glassy carbon electrode," *J. Electroanal. Chem.*, vol. 766, pp. 120–127, 2016, doi: 10.1016/j.jelechem.2016.02.003.

[57]   Y. Zuo, J. Xu, X. Zhu, and X. Duan, "Graphene-derived nanomaterials as recognition elements for electrochemical determination of heavy metal ions : a review," *Microchim. Acta*, vol. 186, no. 171, 2019, doi: https://doi.org/10.1007/s00604-019-3248-5.

[58]   S. Xiong, B. Yang, D. Cai, G. Qiu, and Z. Wu, "Individual and Simultaneous Stripping Voltammetric and Mutual Interference Analysis of Cd 2 + , Pb 2 + and Hg 2 + with Reduced Graphene Oxide-Fe3O4 Nanocomposites," *Electrochim. Acta*, vol. 185, pp. 52–61, 2015, doi: 10.1016/j.electacta.2015.10.114.

[59]   Y. Wei *et al.*, "SnO 2 / Reduced Graphene Oxide Nanocomposite for the Simultaneous Electrochemical Detection of Cadmium (II), Lead (II), Copper (II), and Mercury (II): An Interesting Favorable Mutual Interference," *J. Phys. Chem. C*, vol. 116, no. 1, pp. 1034–1041, 2012, doi: https://doi.org/10.1021/jp209805c.

[60]   A. Fotia *et al.*, "Self standing mats of blended polyaniline produced by electrospinning," *Nanomaterials*, vol. 11, no. 5, pp. 1–15, 2021, doi:

References

10.3390/nano11051269.

[61]   Y. Huang, Y. E. Miao, and T. Liu, "Electrospun fibrous membranes for efficient heavy metal removal," *J. Appl. Polym. Sci.*, vol. 131, no. 19, pp. 1–12, 2014, doi: 10.1002/app.40864.

[62]   Y. Liu, Y. Deng, H. Dong, K. Liu, and N. He, "Progress on sensors based on nanomaterials for rapid detection of heavy metal ions," *Sci. China Chem.*, vol. 60, no. 3, pp. 329–337, 2017, doi: 10.1007/s11426-016-0253-2.

[63]   N. Promphet, P. Rattanarat, R. Rangkupan, O. Chailapakul, and N. Rodthongkum, "An electrochemical sensor based on graphene/polyaniline/polystyrene nanoporous fibers modified electrode for simultaneous determination of lead and cadmium," *Sensors Actuators, B Chem.*, vol. 207, no. PartA, pp. 526–534, 2015, doi: 10.1016/j.snb.2014.10.126.

[64]   H. Huang, W. Zhu, X. Gao, X. Liu, and H. Ma, "Synthesis of a novel electrode material containing phytic acid-polyaniline nanofibers for simultaneous determination of cadmium and lead ions," *Anal. Chim. Acta*, vol. 947, pp. 32–41, 2016, doi: 10.1016/j.aca.2016.10.012.

[65]   C. Zhang *et al.*, "Determination of Cd2+ and Pb2+ based on mesoporous carbon nitride/self-doped polyaniline nanofibers and squarewave anodic stripping voltammetry," *Nanomaterials*, vol. 6, no. 1, pp. 1–11, 2016, doi: 10.3390/nano6010007.

[66]   G. Zhu, Y. Ge, Y. Dai, X. Shang, J. Yang, and J. Liu, "Size-tunable polyaniline nanotube-modified electrode for simultaneous determination of Pb(II) and Cd(II)," *Electrochim. Acta*, vol. 268, pp. 202–210, 2018, doi: 10.1016/j.electacta.2018.02.101.

[67]   N. Ruecha, N. Rodthongkum, D. M. Cate, J. Volckens, O. Chailapakul, and C. S. Henry, "Sensitive electrochemical sensor using a graphene-polyaniline nanocomposite for simultaneous detection of Zn(II), Cd(II), and Pb(II)," *Anal. Chim. Acta*, vol. 874, pp. 40–48, 2015, doi: 10.1016/j.aca.2015.02.064.

[68]   F. H. Narouei, L. Livernois, D. Andreescu, and S. Andreescu, "Highly sensitive mercury detection using electroactive gold-decorated polymer nanofibers," *Sensors Actuators, B Chem.*, vol. 329, no. November 2020, p. 129267, 2021, doi: 10.1016/j.snb.2020.129267.

[69]   D. Li, J. Jia, and J. Wang, "Simultaneous determination of Cd(II) and Pb(II) by differential pulse anodic stripping voltammetry based on graphite nanofibers-Nafion composite modified bismuth film electrode," *Talanta*, vol. 83, no. 2, pp. 332–336, 2010, doi: 10.1016/j.talanta.2010.09.024.

[70]   D. Zhao, T. Wang, D. Han, C. Rusinek, A. J. Steckl, and W. R. Heineman, "Electrospun Carbon Nanofiber Modified Electrodes for Stripping Voltammetry," *Anal. Chem.*, vol. 87, no. 18, pp. 9315–9321, 2015, doi: 10.1021/acs.analchem.5b02017.

[71]   Y. Liao, Q. Li, N. Wang, and S. Shao, "Development of a new electrochemical sensor for determination of Hg(II) based on Bis(indolyl)methane/Mesoporous carbon nanofiber/Nafion/glassy carbon electrode," *Sensors Actuators, B Chem.*, vol. 215, pp. 592–597, 2015, doi: 10.1016/j.snb.2015.04.006.

[72]   C. Pérez-Ràfols, N. Serrano, J. M. Díaz-Cruz, C. Ariño, and M. Esteban, "Glutathione modified screen-printed carbon nanofiber electrode for the voltammetric determination of metal ions in natural samples," *Talanta*, vol. 155, pp. 8–13, 2016, doi: 10.1016/j.talanta.2016.04.011.

[73]   B. Zhang *et al.*, "Facile and green fabrication of size-controlled AuNPs/CNFs hybrids for the highly sensitive simultaneous detection of heavy metal ions," *Electrochim. Acta*, vol. 196, pp. 422–430, 2016, doi: 10.1016/j.electacta.2016.02.163.

[74]   J. E. Robinson, W. R. Heineman, L. B. Sagle, M. Meyyappan, and J. E. Koehne, "Carbon nanofiber electrode array for the detection of lead," *Electrochem. commun.*, vol. 73, pp. 89–93, 2016, doi: 10.1016/j.elecom.2016.11.002.

[75]   L. Oularbi, M. Turmine, and M. El Rhazi, "Electrochemical

References

determination of traces lead ions using a new nanocomposite of polypyrrole/carbon nanofibers," *J. Solid State Electrochem.*, vol. 21, no. 11, pp. 3289–3300, 2017, doi: 10.1007/s10008-017-3676-2.

[76]   S. Zhang, H. Zhu, P. Ma, F. Duan, W. Dong, and M. Du, "A self-supported electrochemical sensor for simultaneous sensitive detection of trace heavy metal ions based on PtAu alloy/carbon nanofibers," *Anal. Methods*, vol. 9, no. 48, pp. 6801–6807, 2017, doi: 10.1039/c7ay02223a.

[77]   S. Gao *et al.*, "Selective voltammetric determination of Cd(II) by using N,S-codoped porous carbon nanofibers," *Microchim. Acta*, vol. 185, no. 6, 2018, doi: 10.1007/s00604-018-2818-2.

[78]   L. Oularbi, M. Turmine, F. E. Salih, and M. El Rhazi, "Ionic liquid/carbon nanofibers/bismuth particles novel hybrid nanocomposite for voltammetric sensing of heavy metals," *J. Environ. Chem. Eng.*, vol. 8, no. 3, p. 103774, 2020, doi: https://doi.org/10.33961/jecst.2019.00528.

[79]   Q. Tang, G. Zhu, Y. Ge, J. Yang, M. Huang, and J. Liu, "AuNPs-polyaniline nanosheet array on carbon nanofiber for the determination of As(III)," *J. Electroanal. Chem.*, vol. 873, p. 114381, 2020, doi: 10.1016/j.jelechem.2020.114381.

[80]   R. Ding *et al.*, "High Sensitive Sensor Fabricated by Reduced Graphene Oxide/Polyvinyl Butyral Nanofibers for Detecting Cu (II) in Water," *Int. J. Anal. Chem.*, vol. 2015, no. Ii, 2015, doi: 10.1155/2015/723276.

[81]   J. Liu, G. Zhu, M. Chen, X. Ma, and J. Yang, "Fabrication of electrospun ZnO nanofiber-modified electrode for the determination of trace Cd(II)," *Sensors Actuators, B Chem.*, vol. 234, pp. 84–91, 2016, doi: 10.1016/j.snb.2016.04.073.

[82]   V. H. B. Oliveira *et al.*, "A sensitive electrochemical sensor for Pb2+ ions based on ZnO nanofibers functionalized by L-cysteine," *J. Mol. Liq.*, vol. 309, 2020, doi: 10.1016/j.molliq.2020.113041.

[83]   G. Zhu, J. Su, B. Zhang, and J. Liu, "Electrospun amino-containing

organosilica gel nanofibers for the ultrasensitive determination of Cu(II)," *J. Electroanal. Chem.*, vol. 882, p. 114976, 2021, doi: 10.1016/j.jelechem.2021.114976.

[84]   M. E. Orazem and B. Tribollet, *Electrochemical Impedance Spectroscopy*, 2nd ed. United Kingdom: Wiley, 2017.

[85]   R. Pollard and T. Comte, "Determination of Transport Properties for Solid Electrolytes from the Impedance of Thin Layer Cells," *J. Electrochem. Soc.*, vol. 136, no. 12, pp. 3734–3748, 1989, doi: https://doi.org/10.1149/1.2096540.

[86]   S. Wang, V. Vivier, M. Gao, and M. E. Orazem, "Electrochemical impedance spectroscopy," *Nat. Rev. Methods Prim. Vol.*, vol. 1, 2021, doi: 10.1038/s43586-021-00039-w.

[87]   B. Mei, J. Lau, T. Lin, S. Tolbert, B. Dunn, and L. Pilon, "Supporting information for : Physical Interpretations of Electrochemical Impedance Spectroscopy (EIS) of Redox Active Electrodes for Electrical Energy Storage," *J. Phys. Chem. C*, vol. 122, no. 43, pp. 24499–24511, 2018, doi: 10.1021/acs.jpcc.8b05241.

[88]   J. Diard, B. Le Gorrec, and C. Montella, "Deviation from the polarization resistance due to non-linearity I - theoretical formulation," *J. Electroanal. Chem.*, vol. 432, no. 1–2, pp. 27–39, 1997, doi: https://doi.org/10.1016/S0022-0728(97)00213-1.

[89]   R. Srinivasan and F. Fasmin, *An Introduction to Electrochemical Impedance Spectroscopy*, 1st ed. Boca Raton: Taylor & Francis Group, 2021, 2021.

[90]   I. Pivac and F. Barbir, "Inductive phenomena at low frequencies in impedance spectra of proton exchange membrane fuel cells – A review," *J. Power Sources*, vol. 326, pp. 112–119, 2016, doi: 10.1016/j.jpowsour.2016.06.119.

[91]   W. H. Mulder, J. H. Sluyters, T. Pajkossy, and L. Nyikos, "Tafel current at fractal electrodes Connection with admittance spectra," *J. Electroanal. Chem. Interfacial Electrochem.*, vol. 285, no. 1–2, pp. 103–115, 1990, doi:

References

https://doi.org/10.1016/0022-0728(90)87113-X.

[92] C. Kim, S. Pyun, and J. Kim, "An investigation of the capacitance dispersion on the fractal carbon electrode with edge and basal orientations," *Electrochim. Acta*, vol. 48, no. 23, pp. 3455–3463, 2003, doi: 10.1016/S0013-4686(03)00464-X.

[93] W. Strunz, C. A. Schiller, and J. Vogelsang, "The evaluation of experimental dielectric data of barrier coatings in frequency- and time domain," *Electrochim. Acta*, vol. 51, no. 8–9, pp. 1437–1442, 2006, doi: 10.1016/j.electacta.2005.02.122.

[94] D. R. Franceschetti and J. R. Macdonald, "Diffusion of neutral and charged species under small-signal a.c. conditions," *J. Electroanal. Chem. Interfacial Electrochem.*, vol. 101, no. 3, pp. 307–316, 1979, doi: https://doi.org/10.1016/S0022-0728(79)80042-X.

[95] J. Llopis, J. Fernández-biarge, and M. Pérez Fernández, "Study of the impedance of a platinum electrode in a redox system," *Electrochim. Acta*, vol. 1, no. 2–3, pp. 130–145, 1959, doi: https://doi.org/10.1016/0013-4686(59)85002-7.

[96] N. Sekar and R. P. Ramasamy, "Electrochemical impedance spectroscopy for microbial fuel cell characterization," *J. Microb. Biochem. Technol.*, vol. S6, 2013, doi: 10.4172/1948-5948.s6-004.

[97] X. Dominguez-Benetton, S. Surajbhan, K. Vanbroekhoven, and D. Pant, "The accurate use of impedance analysis for the study of microbial electrochemical systems," *Chem. Soc. Rev.*, vol. 41, no. 21, pp. 7228–7246, 2012, doi: 10.1039/c2cs35026b.

[98] B. Y. Chang and S. M. Park, "Electrochemical impedance spectroscopy," *Annu. Rev. Anal. Chem.*, vol. 3, no. 1, pp. 207–229, 2010, doi: 10.1146/annurev.anchem.012809.102211.

[99] A. Greiner and J. H. Wendorff, "Electrospinning: A fascinating method for the preparation of ultrathin fibers," *Angew. Chemie - Int. Ed.*, vol. 46, no. 30, pp. 5670–5703, 2007, doi: 10.1002/anie.200604646.

[100] V. Thavasi, G. Singh, and S. Ramakrishna, "Electrospun nanofibers in energy and environmental applications," *Energy Environ. Sci.*, vol. 1, no. 2, pp. 205–221, 2008, doi: 10.1039/b809074m.

[101] Z. Dong, S. J. Kennedy, and Y. Wu, "Electrospinning materials for energy-related applications and devices," *J. Power Sources*, vol. 196, no. 11, pp. 4886–4904, 2011, doi: 10.1016/j.jpowsour.2011.01.090.

[102] N. Bhardwaj and S. C. Kundu, "Electrospinning: A fascinating fiber fabrication technique," *Biotechnol. Adv.*, vol. 28, no. 3, pp. 325–347, 2010, doi: 10.1016/j.biotechadv.2010.01.004.

[103] G. Taylor, "Electrically driven jets," *Proc. R. Soc. London. A.*, vol. 313, pp. 453–475, 1969, doi: 10.1098/rspa.1969.0205.

[104] X. Zong, K. Kim, D. Fang, S. Ran, B. S. Hsiao, and B. Chu, "Structure and process relationship of electrospun bioabsorbable nanofiber membranes," *Polymer (Guildf).*, vol. 43, no. 16, pp. 4403–4412, 2002, doi: 10.1016/S0032-3861(02)00275-6.

[105] J. M. Deitzel, J. Kleinmeyer, D. Harris, and N. C. Beck Tan, "The effect of processing variables on the morphology of electrospun," *Polymer (Guildf).*, vol. 42, pp. 261–272, 2001.

[106] C. Zhang, X. Yuan, L. Wu, Y. Han, and J. Sheng, "Study on morphology of electrospun poly(vinyl alcohol) mats," *Eur. Polym. J.*, vol. 41, no. 3, pp. 423–432, 2005, doi: 10.1016/j.eurpolymj.2004.10.027.

[107] M. M. Demir, I. Yilgor, E. Yilgor, and B. Erman, "Electrospinning of polyurethane fibers," *Polymer (Guildf).*, vol. 43, no. 11, pp. 3303–3309, 2002, doi: 10.1016/S0032-3861(02)00136-2.

[108] S. Zhao, X. Wu, L. Wang, and Y. Huang, "Electrospinning of Ethyl-Cyanoethyl Cellulose/Tetrahydrofuran Solutions," *J. Appl. Polym. Sci.*, vol. 91, no. 1, pp. 242–246, 2004, doi: https://doi.org/10.1002/app.13196.

[109] C.-M. Wu, H.-G. Chiou, S.-L. Lin, and J.-M. Lin, "Effects of electrostatic polarity and the types of electrical charging on

electrospinning behavior," *J. Appl. Polym. Sci.*, vol. 126, no. S2, pp. E89–E97, 2012, doi: https://doi.org/10.1002/app.36680.

[110] T. Mazoochi, M. Hamadanian, M. Ahmadi, and V. Jabbari, "Investigation on the morphological characteristics of nanofiberous membrane as electrospun in the different processing parameters," *Int. J. Ind. Chem.*, vol. 3, no. 1, pp. 1–8, 2012, doi: 10.1186/2228-5547-3-2.

[111] S. Megelski, J. S. Stephens, D. Bruce Chase, and J. F. Rabolt, "Micro- and nanostructured surface morphology on electrospun polymer fibers," *Macromolecules*, vol. 35, no. 22, pp. 8456–8466, 2002, doi: 10.1021/ma020444a.

[112] X. M. Mo, C. Y. Xu, M. Kotaki, and S. Ramakrishna, "Electrospun P(LLA-CL) nanofiber: A biomimetic extracellular matrix for smooth muscle cell and endothelial cell proliferation," *Biomaterials*, vol. 25, no. 10, pp. 1883–1890, 2004, doi: 10.1016/j.biomaterials.2003.08.042.

[113] X. Y. Yuan, Y. Y. Zhang, C. Dong, and J. Sheng, "Morphology of ultrafine polysulfone fibers prepared by electrospinning," *Polym. Int.*, vol. 53, no. 11, pp. 1704–1710, 2004, doi: 10.1002/pi.1538.

[114] S. H. Chen, Y. Chang, K. R. Lee, and J. Y. Lai, "A three-dimensional dual-layer nano/microfibrous structure of electrospun chitosan/poly(d,l-lactide) membrane for the improvement of cytocompatibility," *J. Memb. Sci.*, vol. 450, pp. 224–234, 2014, doi: 10.1016/j.memsci.2013.08.007.

[115] S. Zargham, S. Bazgir, A. Tavakoli, A. S. Rashidi, and R. Damerchely, "The effect of flow rate on morphology and deposition area of electrospun nylon 6 nanofiber," *J. Eng. Fiber. Fabr.*, vol. 7, no. 4, pp. 42–49, 2012, doi: 10.1177/155892501200700414.

[116] J. Stanger, N. Tucker, A. Wallace, N. Larsen, M. Staiger, and R. Reeves, "The Effect of Electrode Configuration and Substrate Material on the Mass Deposition Rate of Electrospinning," *J. Appl. Polym. Sci.*, vol. 112, no. 3, pp. 1729–1737, 2008, doi: https://doi.org/10.1002/app.29663.

[117] N. Chanunpanich, B. Lee, and H. Byun, "A study of electrospun PVDF on PET sheet," *Macromol. Res.*, vol. 16, no. 3, pp. 212–217, 2008, doi: 10.1007/BF03218855.

[118] E. Adomavičiute and S. Stanys, "Formation of Electrospun PVA mats on different types of support materials using various kinds of grounded electrodes," *Fibres Text. East. Eur.*, vol. 19, no. 4 (87), pp. 34–40, 2011.

[119] C. Y. Xu, R. Inai, M. Kotaki, and S. Ramakrishna, "Aligned biodegradable nanofibrous structure: A potential scaffold for blood vessel engineering," *Biomaterials*, vol. 25, no. 5, pp. 877–886, 2004, doi: 10.1016/S0142-9612(03)00593-3.

[120] X. Wang, I. C. Um, D. Fang, A. Okamoto, B. S. Hsiao, and B. Chu, "Formation of water-resistant hyaluronic acid nanofibers by blowing-assisted electro-spinning and non-toxic post treatments," *Polymer (Guildf).*, vol. 46, no. 13, pp. 4853–4867, 2005, doi: 10.1016/j.polymer.2005.03.058.

[121] B. Sundaray, V. Subramanian, T. S. Natarajan, R. Z. Xiang, C. C. Chang, and W. S. Fann, "Electrospinning of continuous aligned polymer fibers," *Appl. Phys. Lett.*, vol. 84, no. 7, pp. 1222–1224, 2004, doi: 10.1063/1.1647685.

[122] D. Li and Y. Xia, "Electrospinning of nanofibers: Reinventing the wheel?," *Adv. Mater.*, vol. 16, no. 14, pp. 1151–1170, 2004, doi: 10.1002/adma.200400719.

[123] C. S. Ki *et al.*, "Electrospun Three-Dimensional Silk Fibroin Nanofibrous Scaffold," *J. Appl. Polym. Sci.*, vol. 106, no. 6, pp. 3922–3928, 2007, doi: https://doi.org/10.1002/app.26914.

[124] K. P. Matabola and R. M. Moutloali, "The influence of electrospinning parameters on the morphology and diameter of poly(vinyledene fluoride) nanofibers- Effect of sodium chloride," *J. Mater. Sci.*, vol. 48, no. 16, pp. 5475–5482, 2013, doi: 10.1007/s10853-013-7341-6.

[125] T. Wang and S. Kumar, "Electrospinning of polyacrylonitrile

References

nanofibers," *J. Appl. Polym. Sci.*, vol. 102, no. 2, pp. 1023–1029, 2006, doi: 10.1002/app.24123.

[126] J. Lannutti, D. Reneker, T. Ma, D. Tomasko, and D. Farson, "Electrospinning for tissue engineering scaffolds," *Mater. Sci. Eng. C*, vol. 27, no. 3, pp. 504–509, 2007, doi: 10.1016/j.msec.2006.05.019.

[127] T. J. Sill and H. A. von Recum, "Electrospinning: Applications in drug delivery and tissue engineering," *Biomaterials*, vol. 29, no. 13, pp. 1989–2006, 2008, doi: 10.1016/j.biomaterials.2008.01.011.

[128] T. Jarusuwannapoom *et al.*, "Effect of solvents on electro-spinnability of polystyrene solutions and morphological appearance of resulting electrospun polystyrene fibers," *Eur. Polym. J.*, vol. 41, no. 3, pp. 409–421, 2005, doi: 10.1016/j.eurpolymj.2004.10.010.

[129] L. Huang, K. Nagapudi, P. R. Apkarian, and E. L. Chaikof, "Engineered collagen - PEO nanofibers and fabrics," *J. Biomater. Sci. Polym. Ed.*, vol. 12, no. 9, pp. 979–993, 2001, doi: 10.1163/156856201753252516.

[130] A. Koski, K. Yim, and S. Shivkumar, "Effect of molecular weight on fibrous PVA produced by electrospinning," *Mater. Lett.*, vol. 58, no. 3–4, pp. 493–497, 2004, doi: 10.1016/S0167-577X(03)00532-9.

[131] P. Gupta, C. Elkins, T. E. Long, and G. L. Wilkes, "Electrospinning of linear homopolymers of poly(methyl methacrylate): Exploring relationships between fiber formation, viscosity, molecular weight and concentration in a good solvent," *Polymer (Guildf).*, vol. 46, no. 13, pp. 4799–4810, 2005, doi: 10.1016/j.polymer.2005.04.021.

[132] V. Pillay *et al.*, "A Review of the Effect of Processing Variables on the Fabrication of Electrospun Nanofibers for Drug Delivery Applications," *J. Nanomater.*, vol. 2013, p. 22, 2013, doi: https://doi.org/10.1155/2013/789289.

[133] P. Filip, P. Peer, and J. Zelenkova, "Dependence of poly(vinyl butyral) electrospun fibres diameter on molecular weight and concentration," *J. Ind. Text.*, 2020, doi: 10.1177/1528083720974038.

[134] J. S. Lee *et al.*, "Role of molecular weight of atactic poly(vinyl alcohol) (PVA) in the structure and properties of PVA nanofabric prepared by electrospinning," *J. Appl. Polym. Sci.*, vol. 93, no. 4, pp. 1638–1646, 2004, doi: 10.1002/app.20602.

[135] C. J. Angammana and S. H. Jayaram, "Analysis of the Effects of Solution and Process Parameters on the Electrospinning Process and Nanofibre Morphology," *Ieee Trans. Ind. Appl.*, vol. 47, no. 3, pp. 1109–1117, 2011, doi: 10.1109/TIA.2011.2127431.

[136] M. M. Hohman, M. Shin, G. Rutledge, and M. P. Brenner, "Electrospinning and electrically forced jets. II. Applications," *Phys. Fluids*, vol. 13, no. 8, p. 2221, 2001, doi: 10.1063/1.1384013.

[137] A. K. Haghi and M. Akbari, "Trends in electrospinning of natural nanofibers," in *Physica Status Solidi (A) Applications and Materials Science*, 2007, vol. 204, no. 6, pp. 1830–1834, doi: 10.1002/pssa.200675301.

[138] Q. P. Pham, U. Sharma, and A. G. Mikos, "Electrospun poly (ε-caprolactone) microfiber and multilayer nanofiber/microfiber scaffolds: Characterization of scaffolds and measurement of cellular infiltration," *Biomacromolecules*, vol. 7, no. 10, pp. 2796–2805, 2006, doi: 10.1021/bm060680j.

[139] G. T. Kim *et al.*, "Effect of humidity on the microstructures of electrospun polystyrene nanofibers," *Microsc. Microanal.*, vol. 10, no. S02, pp. 554–555, 2004, doi: 10.1017/S1431927604882187.

[140] P. K. Baumgarten, "Electrostatic spinning of acrylic microfibers," *J. Colloid Interface Sci.*, vol. 36, no. 1, pp. 71–79, 1971, doi: 10.1016/0021-9797(71)90241-4.

[141] C. L. Casper, J. S. Stephens, N. G. Tassi, D. B. Chase, and J. F. Rabolt, "Controlling surface morphology of electrospun polystyrene fibers: Effect of humidity and molecular weight in the electrospinning process," *Macromolecules*, vol. 37, no. 2, pp. 573–578, 2004, doi: 10.1021/ma0351975.

References

[142] H. I. Içoğlu and R. T. Oğulata, "Effect of ambient parameters on morphology of electrospun polyetherimide (PEI) fibers," *Tekst. ve Konfeksiyon*, vol. 23, no. 4, pp. 313–318, 2013.

[143] J. I. Goldstein, D. E. Newbury, J. R. Michael, N. W. M. Ritchie, J. H. J. Scott, and D. C. Joy, *Scanning electron microscopy and X-ray microanalysis*. Springer, 2017.

[144] A. Chauhan and P. Chauhan, "Powder XRD technique and its applications in science and technology," *J Anal Bioanal Tech*, vol. 5, no. 5, pp. 1–5, 2014.

[145] S. Loganathan, R. B. Valapa, R. K. Mishra, G. Pugazhenthi, and S. Thomas, "Thermogravimetric analysis for characterization of nanomaterials," in *Thermal and Rheological Measurement Techniques for Nanomaterials Characterization*, Elsevier, 2017, pp. 67–108.

[146] S. Koombhongse, W. Liu, and D. H. Reneker, "Flat Polymer Ribbons and Other Shapes by Electrospinning," *J. Polym. Sci. Part B Polym. Phys.*, vol. 39, no. 21, pp. 2598–2606, 2001, doi: 10.1002/polb.0000.

[147] K. J. Thomas, M. Sheeba, V. P. N. Nampoori, C. P. G. Vallabhan, and P. Radhakrishnan, "Raman spectra of polymethyl methacrylate optical fibres excited by a 532 nm diode pumped solid state laser," *J. Opt. A Pure Appl. Opt.*, vol. 10, no. 5, p. 055303, 2008, doi: 10.1088/1464-4258/10/5/055303.

[148] H. R. Rottmann, "Photolithography in integrated circuit mask metrology," *IBM J. Res. Dev.*, vol. 18, no. 3, pp. 225–231, 1974.

[149] R. Balma, K. Petsch, and T. Kaya, "Development of thin film photolithography process: patterning printed circuit boards (PCBs) and copper electroplating," in *Proc. 2011 ASEE Anual conference*, 2011, pp. 1–9.

[150] D. Ji *et al.*, "'Double exposure method': a novel photolithographic process to fabricate flexible organic field-effect transistors and circuits," *ACS Appl. Mater. Interfaces*, vol. 5, no. 7, pp. 2316–2319, 2013.

[151] D. Yang *et al.*, "Fabrication of ZnO nanorods based gas sensor pattern by photolithography and lift off techniques," *J. King Saud Univ.*, vol. 33, no. 3, p. 101397, 2021.

[152] H. Al Hashimi and O. Chaalal, "Flexible temperature sensor fabrication using photolithography technique," *Therm. Sci. Eng. Prog.*, vol. 22, p. 100857, 2021.

[153] S. Swann, "Magnetron sputtering," *Phys. Technol.*, vol. 19, no. 2, p. 67, 1988.

[154] X. Cai, P. Zhu, X. Lu, Y. Liu, and T. Lei, "Electrospinning of very long and highly aligned fibers," *J. Mater. Sci.*, vol. 52, no. 24, pp. 14004–14010, 2017, doi: 10.1007/s10853-017-1529-0.

[155] W. Teo and S. Ramakrishna, "Electrospun fibre bundle made of aligned nanofibres over two fixed points," *Nanotechnology*, vol. 16, no. 9, p. 1878, 2005, doi: 10.1088/0957-4484/16/9/077.

[156] H. Yan, L. Liu, and Z. Zhang, "Alignment of electrospun nanofibers using dielectric materials Alignment of electrospun nanofibers using dielectric materials," *Appl. Phys. Lett.*, vol. 95, no. 14, p. 143114, 2009, doi: 10.1063/1.3242378.

[157] W. Zhong, F. Li, L. Chen, and Y. Wei, "A novel approach to electrospinning of pristine and aligned MEH-PPV using," *J. Mater. Chem.*, vol. 22, no. 12, pp. 5523–5530, 2012, doi: 10.1039/c2jm15970h.

[158] L. Assaud, M. Hanbücken, and L. Santinacci, " Atomic Layer Deposition of TiN/Al 2 O 3 /TiN Nanolaminates for Capacitor Applications ," *ECS Meet. Abstr.*, vol. MA2012-02, no. 28, pp. 2475–2475, 2012, doi: 10.1149/ma2012-02/28/2475.

[159] P. Roy *et al.*, "Preventing Corrosion of Aluminum Metal with Nanometer-Thick Films of Al2O3Capped with TiO2for Ultraviolet Plasmonics," *ACS Appl. Nano Mater.*, vol. 4, no. 7, pp. 7199–7205, 2021, doi: 10.1021/acsanm.1c01160.

[160] L. Baldrianova, P. Agrafiotou, I. Svancara, A. D. Jannakoudakis, and S.

Sotiropoulos, "The effect of acetate concentration, solution pH and conductivity on the anodic stripping voltammetry of lead and cadmium ions at in situ bismuth-plated carbon microelectrodes," *J. Electroanal. Chem.*, vol. 660, no. 1, pp. 31–36, 2011, doi: 10.1016/j.jelechem.2011.05.028.

[161] K. Maeda, "Metal-Complex/Semiconductor Hybrid Photocatalysts and Photoelectrodes for CO2 Reduction Driven by Visible Light," *Adv. Mater.*, vol. 31, no. 25, p. 1808205, 2019.

[162] S. Wang, J. Zhang, O. Gharbi, V. Vivier, M. Gao, and M. E. Orazem, "Electrochemical impedance spectroscopy," *Nat. Rev. Methods Prim.*, vol. 1, no. 1, pp. 1–21, 2021.

[163] B. Petovar, K. Xhanari, and M. Finšgar, "A detailed electrochemical impedance spectroscopy study of a bismuth-film glassy carbon electrode for trace metal analysis," *Anal. Chim. Acta*, vol. 1004, pp. 10–21, 2018, doi: 10.1016/j.aca.2017.12.020.

[164] D. Zhang, J. Tong, B. Xia, and Q. Xue, "Ultrahigh performance humidity sensor based on layer-by-layer self-assembly of graphene oxide/polyelectrolyte nanocomposite film," *Sensors Actuators B Chem.*, vol. 203, pp. 263–270, 2014.

[165] M. A. Deshmukh *et al.*, "EDTA-modified PANI/SWNTs nanocomposite for differential pulse voltammetry based determination of Cu (II) ions," *Sensors Actuators B Chem.*, vol. 260, pp. 331–338, 2018.

[166] H. Li, X. Dong, E. B. da Silva, L. M. de Oliveira, Y. Chen, and L. Q. Ma, "Mechanisms of metal sorption by biochars: biochar characteristics and modifications," *Chemosphere*, vol. 178, pp. 466–478, 2017.

[167] R. Xu, X. Huang, H. Li, M. Su, and D. Chen, "Simultaneous removal of thallium and EDTA by Fenton process," in *IOP Conference Series: Earth and Environmental Science*, 2018, vol. 111, no. 1, p. 12034.

[168] V. Nasteski, "An overview of the supervised machine learning methods," *Horizons.B*, vol. 4, no. December 2017, pp. 51–62, 2017, doi:

10.20544/horizons.b.04.1.17.p05.

[169] P. Cunningham, M. Cord, and S. J. Delany, "Supervised learning," in *Machine learning techniques for multimedia*, Springer, 2008, pp. 21–49.

[170] Z. Ghahramani, "Unsupervised learning," in *Summer school on machine learning*, 2003, pp. 72–112.

[171] X. Zhu and A. B. Goldberg, "Introduction to semi-supervised learning," *Synth. Lect. Artif. Intell. Mach. Learn.*, vol. 3, no. 1, pp. 1–130, 2009.

[172] R. S. Sutton and A. G. Barto, *Reinforcement learning: An introduction*. MIT press, 2018.

[173] O. Chapelle, B. Schölkopf, and A. Zien, "A discussion of semi-supervised learning and transduction," in *Semi-supervised learning*, MIT Press, 2006, pp. 473–478.

[174] S. Zhang, C. Zhang, and Q. Yang, "Data preparation for data mining," *Appl. Artif. Intell.*, vol. 17, no. 5–6, pp. 375–381, 2003, doi: 10.1080/713827180.

[175] M. Kaden, M. Lange, D. Nebel, M. Riedel, T. Geweniger, and T. Villmann, "Aspects in classification learning-Review of recent developments in Learning Vector Quantization," *Found. Comput. Decis. Sci.*, vol. 39, no. 2, pp. 79–105, 2014.

[176] D. Maulud and A. M. Abdulazeez, "A review on linear regression comprehensive in machine learning," *J. Appl. Sci. Technol. Trends*, vol. 1, no. 4, pp. 140–147, 2020.

[177] P. C. Sen, M. Hajra, and M. Ghosh, *Supervised Classification Algorithms in Machine Learning: A Survey and Review*. Springer Singapore, 2020.

[178] B. Cestnik, I. Kononenko, and I. Bratko, "ASSISTANT 86: A knowledge-elicitation tool for sophisticated users," in *Proceedings of the 2nd European conference on European working session on learning*, 1987, pp. 31–45.

[179] R. O. Duda, P. E. Hart, and D. G. Stork, "Pattern classification 2nd ed,"

John Willey Sons Inc, 2001.

[180] V. Vapnik, *The nature of statistical learning theory*. Springer science & business media, 1999.

[181] T. Hastie, R. Tibshirani, J. H. Friedman, and J. H. Friedman, *The elements of statistical learning: data mining, inference, and prediction*, vol. 2. Springer, 2009.

[182] K. Fukunaga, *Introduction to statistical pattern recognition*. Elsevier, 2013.

[183] A. Tharwat, "Linear vs. quadratic discriminant analysis classifier: a tutorial," *Int. J. Appl. Pattern Recognit.*, vol. 3, no. 2, pp. 145–180, 2016.

[184] M. Lázaro-Gredilla, J. Quinonero-Candela, C. E. Rasmussen, and A. R. Figueiras-Vidal, "Sparse spectrum Gaussian process regression," *J. Mach. Learn. Res.*, vol. 11, pp. 1865–1881, 2010.

[185] E. Schulz, M. Speekenbrink, and A. Krause, "A tutorial on Gaussian process regression: Modelling, exploring, and exploiting functions," *J. Math. Psychol.*, vol. 85, pp. 1–16, 2018.

[186] X. Dong and Z. Yu, "A survey on ensemble learning," *Front. Comput. Sci.*, vol. 14, no. 2, pp. 241–258, 2020, doi: doi.org/10.1007/s11704-019-8208-z.

[187] M. Merenda, V. Mazzullo, R. Carotenuto, and F. G. Della Corte, "Tiny Machine Learning Techniques for Driving Behavior Scoring in a Connected Car Environment," in *2021 6th International Conference on Smart and Sustainable Technologies (SpliTech)*, 2021, pp. 1–6.

9

Publications

- L. Bonaccorsi, A. Fotia, A. Malara, and P. Frontera, "Advanced Adsorbent Materials for Waste Energy Recovery" Energies, vol. 13, no. 17, p. 4299, 2020, doi: 10.3390/en13174299;

- Fotia, A. Malara, E. Paone, L. Bonaccorsi, P. Frontera, G. Serrano, A. Caneschi "Self Standing Mats of Blended Polyaniline Produced by Electrospinning" Nanomaterials, vol. 11, no. 5, p. 1269, 2021, https://doi.org/10.3390/nano11051269 ;

- Malara, A. Fotia, E. Paone and G. Serrano "Electrospun Nanofibers and Electrochemical Techniques for the Detection of Heavy Metal Ions" Materials, vol.14, no. 11, p. 3000, 2021. https://doi.org/10.3390/ma14113000 ;

- Gnisci, A.; Fotia, A.; Bonaccorsi, L.; Donato, A. Effect of Working Atmospheres on the Detection of Diacetyl by Resistive SnO2 Sensor. Appl. Sci. 2022, 12, 367. https://doi.org/10.3390/app12010367 ;

- Bonaccorsi, L.; Donato, A.; Fotia, A.; Frontera, P.; Gnisci, A. Competitive Detection of Volatile Compounds from Food Degradation by a Zinc Oxide Sensor. Appl. Sci. 2022, 12, 2261. https://doi.org/10.3390/app12042261;